January 2010

Pattern formation and magnetism in pulsed laser-induced self-organized nanostructures from single and bilayer metallic films

Hare Krishna
Washington University in St. Louis

WASHINGTON UNIVERSITY IN ST. LOUIS

Department of Physics

Dissertation Examination Committee:

Ramki Kalyanaraman, Chair

Kenneth Kelton

James Schilling

Zohar Nussinov

Sophia Hayes

William Buhro

Hernando Garcia

PATTERN FORMATION AND MAGNETISM IN PULSED LASER-INDUCED SELF-ORGANIZED NANOSTRUCTURES FROM SINGLE AND BILAYER METALLIC FILMS

by

Hare Krishna

A dissertation presented to the

Graduate School of Arts and Sciences

of Washington University in

partial fulfillment of the

requirements for the degree

of Doctor of Philosophy

May 2010

Saint Louis, Missouri

ABSTRACT OF THE DISSERTATION

Pattern formation and magnetism in pulsed laser-induced self-organized nanostructures from single and bilayer metallic films

by

Hare Krishna

Doctor of Philosophy in Physics

Washington University in St. Louis, 2010

Professor Ramki Kalyanaraman, Chairperson

Self-organization via nanosecond pulsed laser melting of thin metal films is attractive as a reliable and low cost method to create surface metallic nanostructures. The potential applications of these resulting structures are related to their magnetic, optical, plasmonic, and magneto-optical properties, such as in high density magnetic storage, energy harvesting, and sensing. In this dissertation experimental and theoretical mechanisms of nanoscale patterning by dewetting self-organization was explored in nanoscopic thickness single and bilayer metal films. Magnetism in the resulting nanostructures was also explored. Experimental techniques included thin film deposition, laser irradiation, scanning and transmission electron microscopy, atomic force and magnetic force microscopy. A thermodynamic model of dewetting based on comparing the rate of change of free energy to frictional loss via viscous dissipation was developed. From this model the length scale characteristics of the self-organization in single and bilayer metal systems was determined. The model was successfully applied to experimental behavior of pulsed-laser induced dewetting of Ag, as well as for Co, where intrinsic thermocapillary effects influenced dewetting. Another finding was that the metal films show a thickness dependent dewetting morphology. This was investigated in detail for Ag on SiO_2 substrates and it was found that for films less then 9.5 nm, the early stages of dewetting consisted of bicontinuous structures, while

above, it consisted of regular sized holes. This observation was consistent with a previously published theoretical argument that morphology was based on the film-thickness dependent location of the minimum in the free energy curvature. In this model, bicontinuous patterns occur for thickness below the curvature minimum, while holes occur above it. For bilayer self-organization, the immiscible metals Ag and Co were investigated on SiO_2 substrates. The thermodynamic theory predicted substantially different length scales for the two bilayer configurations, Ag/Co/SiO_2 and Co/Ag/SiO_2. This behavior was corroborated by experimental measurements based on pulsed laser dewetting. The difference arises due to change in the sign and magnitude of intermolecular forces for the two configurations. The nanoparticles resulting from bilayer self-organization consisted of granular nanostructure with each nanoparticle containing phase separatedl grains of Ag and Co, thus representing nanoscale nanocomposites. Extensive magnetic investigations were performed on hemispherical shaped nanoparticles of elements (Co, Fe, Ni), alloys (FeCo) and composites (CuCo), created by the laser dewetting process. By utilizing magnetic force microscopy technique, the magnetic anisotropy of individual nanoparticles was determined. The most important discovery was a size-dependent single-domain magnetic anisotropy due to which, smaller particles had an in-plane magnetic orientation while larger particles were out-of-plane. The reason for the unusual out-of-plane orientation for the hemispherical particles was a residual strain in the nanoparticles following the large cooling rates under laser melting. The resulting magnetoelastic energy was sufficient to overcome shape and magnetocrystalline anisotropy energies. These investigations present a fundamental picture of nanostructure synthesis via pulsed laser-induced dewetting and self-organization in single and bilayer films and the magnetic behavior of the processed materials.

Acknowledgments

First and foremost, I would like to thank my advisor Prof. Ramki Kalyanaraman, for his patience, motivation, enthusiasm, immense knowledge and the continuous support of my Ph.D study and research. I appreciate all his contribution of time, ideas, sometimes his presence during the experiments and the motivation during the tough time in the Ph.D. pursuit. I could not have asked for a better advisor and mentor for my Ph. D. study.

Besides my advisor, I would like to thank the rest of my thesis committee members: Prof. K. F. Kelton, Prof. J. Schilling, Prof. Z. Nussinov, Prof. S. E. Hayes, Prof. W. Buhro and Prof. H. Garcia for their encouragement, insightful comments and questions.

My especial thanks goes to Dr. Anup Gangopadhyay for his tremendous contribution in my research during the entire period of my Ph.D study. I appreciate all his contribution in research ideas, advice for experiments and in analyzing the data. I would also like to thank Dr. Tyrone Daulton for teaching me few sophisticated instruments.

My sincere thanks also goes to all the WashU Physics department staff members for their help and support during my Ph.D. study. I also thank Washington university engineering department and Oak Ridge National Laboratory Knoxville for letting me use their facilities, which helped me to complete my research.

I thank my old labmates Chris Favazza and Justin Trice. I appreciate Chris for teaching me some instruments and experiments, many fruitful research discussions, suggestions for my experiments and being such a good friend. I thank Justin Trice for research discussions and some suggestions.

I also would like to thank my current labmates: Nozomi, Jeremy, Ritesh, Vanessa, Paul and Sagar. I appreciate Nozomi and Ritesh for their help in some of my experiments and being such a supporting labmates and good friends. I appreciate Jeremy's help in some of my research work. I also thank Sandy, Carla, Doug and many others in University of Tennessee - Knoxville, for their support during my stay at UTK.

I also thank some of my friends Abhas, Anamika, Biplab, Swati, Satya, Arup, Nayna,

Dasha, Pinaki and Manoranjan. Their emotional support made my Ph.D. study, a smooth journey.

Last but not the least, I would like to thank all my family members for their love and encouragement in all my good and tough times throughout my life.

Contents

List of Figures

List of Tables

Chapter 1

Introduction

Nanoscale materials have unique properties compared with both macroscopic bulk materials and individual atoms/molecules. Research in nanoscience focuses on the fundamental study and manipulation of materials in order to design, fabricate and characterize structures in the nanometer scale. The ultimate goal is to develop materials and devices that will overcome the existing technological limitations and even create new and novel functionalities. In this respect, the ability to manipulate and measure matter at the nanometer level is making it possible to synthesize a new generation of materials with enhanced mechanical [7], optical [8], plasmonic [9, 10], magnetic [11, 12, 13] and magneto-plasmonic [14] properties. Nanostructure devices can be based on tailoring these properties starting, at the molecular level [15, 16], in the structures comprised of three-dimensions nanometer scale components [17], or based on nanostructured surfaces with lateral features and/or ultrathin films of nanometer scale thickness [18, 19, 20]. Because of the partial realization of some of these objectives and vast potential for future applications, it has captured the attention and imagination of researchers in every area of science.

The focus of this work is to explore robust and cost-effective pathways to make nanostructured metallic and magnetic materials, comprised of different nanomorphologies of particles, polygons, wires, and bicontinuous structures (see Fig. 1.1), whose size, and

spatial arrangements can lead to various interesting applications. For example, spatially ordered arrays of single domain magnetic nanoparticles can be used for high density magnetic storage applications [21], nanowires for nanomagnetics [22], electronics [23] and sensors [24], surface plasmon waveguides made from linear chains of metal nanoclusters [25, 26], ordered metal nanocatalyst seeds to make high-efficiency flat-panel displays from carbon-nanotube arrays [27], and coupled magneto-plasmonic nanostructures for high density magneto-optical recording technology [28]. In most of these applications, controlling the spatial ordering, size, shape, composition and crystallographic orientation over large macroscopic length scales is necessary [29].

The development of magnetism in the nanoscale is primarily motivated by the demand for increasing areal density in magnetic data storage [21]. The technically challenging parameters to achieve are size, separation, and the long term stability of the magnetic state of the material. The highest density can be achieved by using particles with magnetization direction perpendicular to the plane, which simultaneously improves the signal-to-noise ratio [30] and lowers the read and write errors [31], compared to particles with in-plane magnetization. In addition, arrays of magnetic nanoparticles have potential applications in non-volatile and high speed magnetic random access memories (MRAM) [32]. These requirements call for robust and cost-effective nanomanufacturing processes that can make ordered surface nanostructures with the desired attributes. Nanostructured self-assembly and/or self-organization is one of the potential routes to achieve these ends [33, 34, 35]. By exploiting these techniques of assembling nanoscale building blocks with molecular precision, it becomes possible to design materials with a wider choice of functionalities and properties with well-defined architectures at different length scales.

In this chapter, the next section (sec. 1.1) will provide the background of self-organization theory for single and bilayer metal systems. Following this, the background on nanomagnetism and the properties of different nanostructures will be presented, in sec. 1.2. Finally,

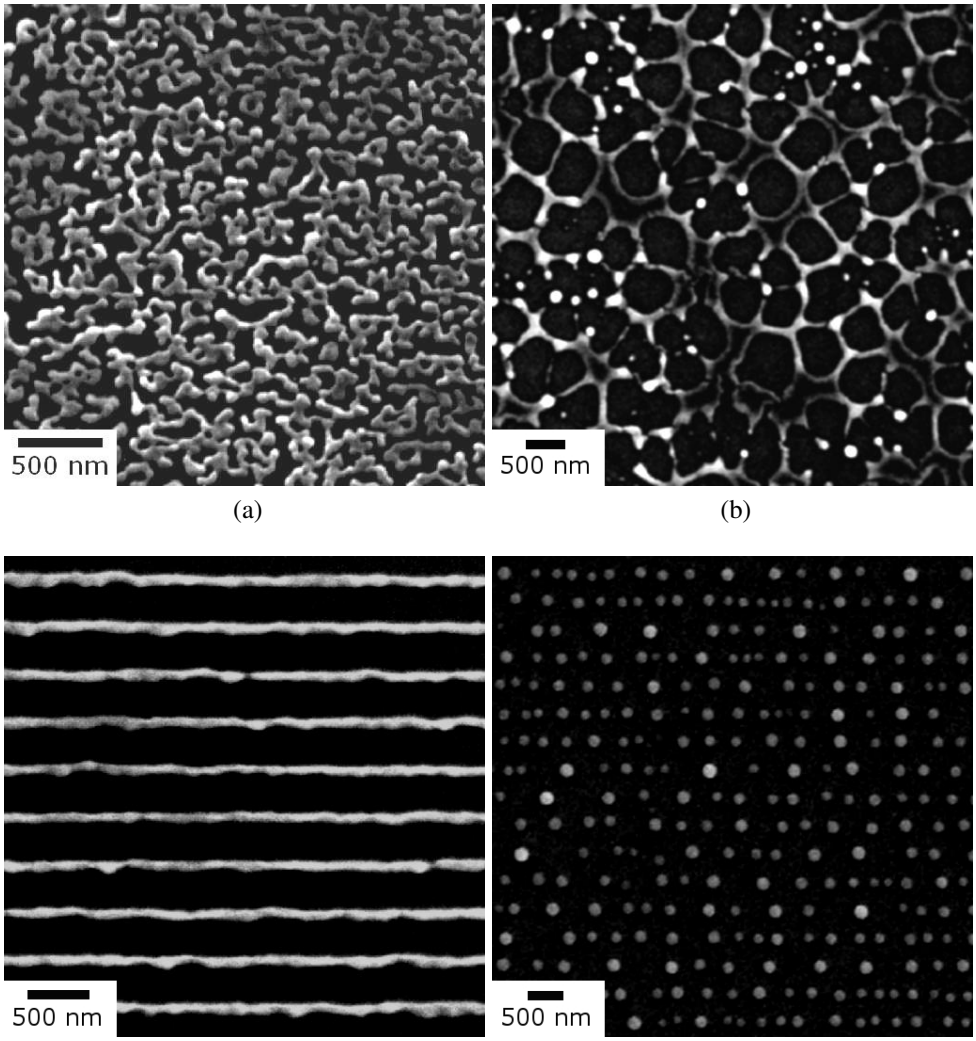

(a) (b)

(c) (d)

Figure 1.1: Different nanomorphologies as a result of self-organization of thin metal films; (a) bicontinuous structure, (d) polygon networks [1], (c) ordered nanowires, and (d) ordered nanoparticles.

the chapter will end with an outline of the important problems and results explored in this dissertation (sec. 1.3), which will be detailed in the subsequent chapters.

1.1 Self-organization

The spontaneous formation of patterns of well-defined structures by self-organization is a fundamental and technologically relevant topic of ongoing research. Various material systems show self-organizing characteristics: atoms rearrange in a predictable manner to form specific crystals, epitaxially strained thin films break into quantum dots [2], biological systems develop characteristic patterns and length scales [3, 36] (see Fig. 1.2). The processes involved in these systems possess some very attractive features from the perspective of manufacturing, namely, repeatability and cost-effectiveness. Another important characteristic is that such spontaneous processes can encompass a wide range of length (and time) scales, from nanometers in the case of thin film dewetting [37] to hundreds of kilometers in geological structures [38]. Therefore, the study of self-organizing systems is of tremendous practical importance and will likely play an important role in the realization of various nano- and micro-technologies. *In this work, the spontaneous pattern formation or self-organization resulting from nanosecond (ns) pulsed laser melting and subsequent dewetting of the ultrathin films was investigated. The results show that this approach is a promising route to realize robust nanoscale structures for magnetic, electronic and optical applications.*

Self-organization (SO) is the process by which intrinsic forces of a system lead to a spontaneous selection of length scales and patterns. It is an underlying principle that can explain structural organization over a wide range, from the molecular to the astronomical scales. Some examples of SO system include weather patterns, solar systems, and self-assembled monolayers. Some of the widely investigated self-organizing systems include

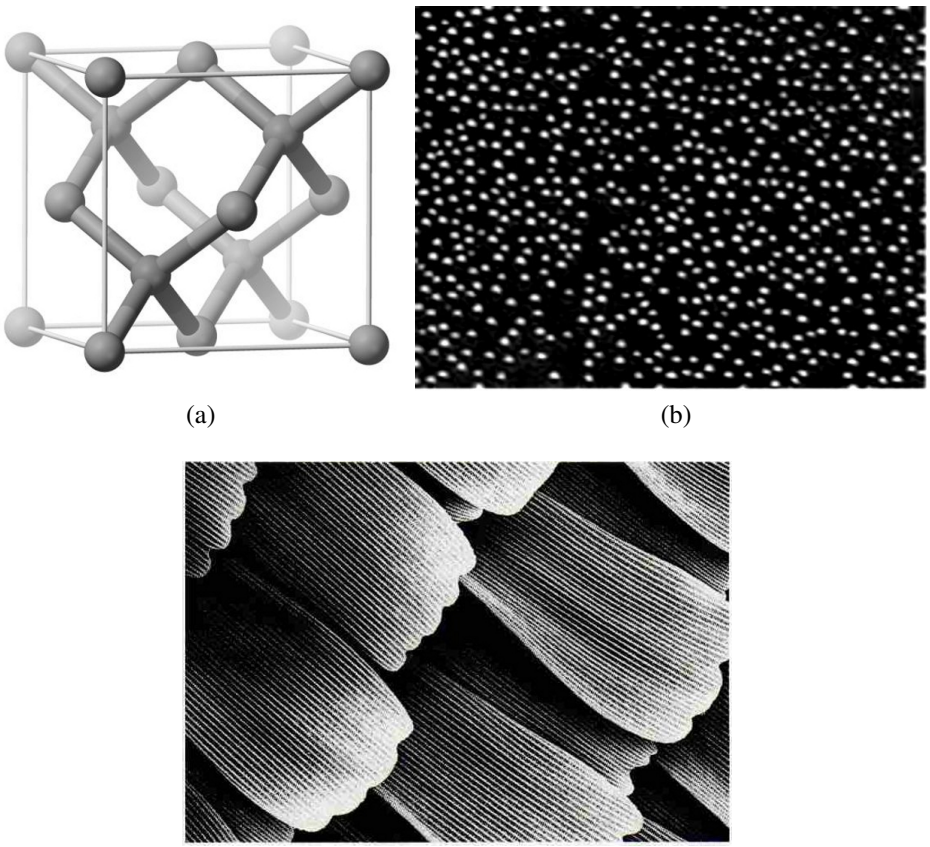

(a) (b)

(c)

Figure 1.2: Self-organized structures; (a) assembly of atoms to form periodic arrangements in a crystal, (b) Ge quantum dots on Si [2] (image size is $3\mu m \times 2\mu m$), and (c) patterns on the wing of the lady butterfly [3] (Magnification, $\times 400$).

thin films of liquid polymers [33, 39, 40, 41, 42], biomolecular self-assembly in protein folding or within cells [43], and the formation of micelles by surfactant molecules in a solution [44]. Mimicking these strategies and creating novel molecules with the ability to self-organize into molecular assemblies is an important paradigm in nanotechnology. In SO, the final structure is encoded in the shape and properties of the molecules that are used, as compared to traditional techniques, such as lithography, where the desired final structure must be obtained from a larger block of matter.

The phenomenon of dewetting, in which an initially flat liquid or solid film spontaneously breaks-up into various complex morphologies, is one potential route to create SO surface structures [45, 46, 47, 48, 33, 49, 40, 37, 4, 50, 35, 51]. Dewetting is a part of everyday life, and also plays an important role in many technological processes. Few common examples are biological systems such as self-cleaning plant leaves, rolling down of water drops down the car windshield, oil droplets on water surface and surface coatings. A thorough understanding of this dynamic dewetting phenomena in the nanoscale is a prerequisite to utilize this process for applications in nanotechnology. On a macroscopic scale, dewetting phenomena can be described in terms of the Young's equation, with the surface tensions between the different phases determining the equilibrium contact angle $\theta_{eq} = cos^{-1}[(\gamma_{SV} - \gamma_{SL})/\gamma_{LV}]$. Here γ_{SV}, γ_{SL} and γ_{LV} are the surface energies between the substrate-vacuum, substrate-liquid and liquid-vacuum, respectively. However, in thin films, the interfacial interactions are much stronger and provide more interesting insights of the dewetting process. The dynamics of the thin liquid film can be determined by using the parameters of the hydrodynamic equations such as viscosities, surface tensions, and the boundary conditions.

1.1.1 Background

The fundamental reason for the formation of drops is that the droplet-surface system has a lower energy than the continuous film-substrate system. What is most relevant to current

nanomanufacturing strategies is whether this spontaneous dewetting process can yield predictable nanomorphologies in a reliable and cost-effective manner. Based on the studies of dewetting of thin polymer films made over the past 50 years, it is evident that dewetting could be a very advantageous processing technique, even for metallic materials. These studies have uncovered several features that are very relevant to nanomanufacturing strategies. Most importantly, the thermodynamically unstable polymer film-substrate systems show evidence for spontaneous dewetting with well-defined intermediate and final morphologies at specific length scales. For film-substrate systems that show this effect, there is a strong resemblance between the shape of the free energy as a function of film thickness to the composition dependent behavior in binary systems showing spinodal phase segregation [52] (Fig. 1.3). Hence, such systems are often referred to dewet by spinodal dewetting [53, 54, 55, 56]. A typical thin film-substrate spinodal dewetting system will have a thickness dependent free energy per unit area $G(h)$ given by:

$$G(h) = G_{Surf} + G_{Int} + G_{Vol} + G_{Ext} \tag{1.1}$$

The surface free energy (G_{Surf}) describes the energy of a liquid-vapor or solid-vapor interface, and for a film in contact with vacuum is given by the appropriate surface tension γ_{fv} with units of energy/area. The interfacial free energy (G_{Int}) describes the energy of the liquid-solid, liquid-liquid or solid-solid interface and for a film on substrate is given by the interfacial tension γ_{fs}. A typical external free energy (G_{Ext}) is the gravitational energy $G_{Ext} = 1/2\rho g h^2$, where ρ is the density of the film, g is the local acceleration due to gravity and h is the height of the film. Unlike the surface, interface, and gravitational energy terms, the volume free energy term (G_{Vol}) can take several forms and is dictated by the system of interest. For instance, in epitaxial solid film-substrate systems the energy associated with lattice mismatch strain will contribute to the volume free energy [57, 58, 59]. In the case of

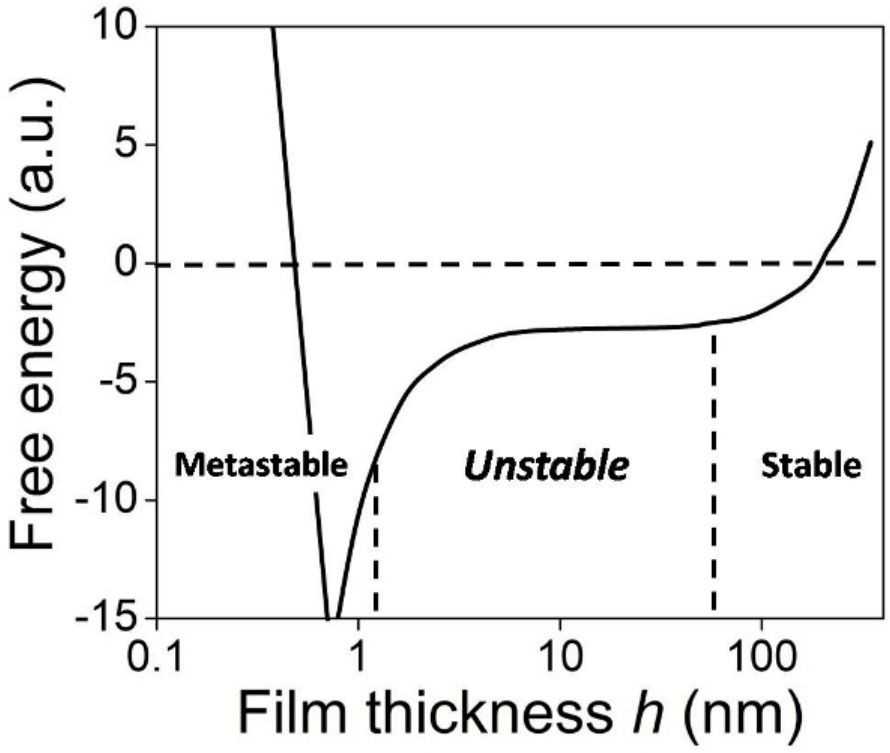

Figure 1.3: Plot of free energy per unit area as a function of film thickness h.

polymer films and metal films on inert amorphous substrates such as SiO_2, the commonly observed volume free energy term arises from intermolecular dispersion forces. The atomic origin of this intermolecular force is the van der Waals interaction between non-polar atoms in which the interaction energy varies as $1/h^6$, where h is the spacing between the particles. The extension of this point-like interaction energy to describe the free energy of interaction between planar interfaces is achieved by a pairwise addition of the van der Waals interaction. This results in an energy per unit area expressed as $G_{vol}^{Disp} = A/h^2$, where A is the Hamaker coefficient, which determines the sign and magnitude of interaction between the substrate-film and film-vacuum interface. The Hamaker coefficient, A, can be calculated through a relation of the frequency-dependent dielectric coefficients of the different media, which is summed over the entire frequency regime and is proportional to $(\varepsilon_1 - \varepsilon_2)(\varepsilon_2 - \varepsilon_3)$, where ε_1, ε_2 and ε_3 are the dielectric functions of substrate, film and vacuum, respectively [60, 61]. From the Hamaker relation, it is seen that the interaction energy is attractive

when the film has a larger (or smaller) dielectric constant than *both* the substrate and the vacuum (or vapor). In the case of polymer liquids and metal films on dielectric substrates like SiO_2 in a gaseous or vacuum medium, the free energy is attractive, *i.e*, Hamaker coefficient is negative. More importantly, for films in the thickness regime of 1 to 100 nm, for which gravitational energy is negligible, the curvature of the free energy is negative, *i.e.* $d^2G/dh^2 < 0$, as shown in Fig. 1.3. This unstable regime strongly resembles the free energy curvature found within the spinodal regime of binary phase segregating systems.

The second important finding of dewetting studies of unstable films is the progression of morphology from a initially smooth liquid film to the final droplet state. This occurs with intermediate states that have well-defined length scales and complex morphologies. Generally, two different intermediate morphologies are seen before the final particulate state: the film breaks by formation of holes followed by polygonal structures *or* through the formation of bicontinuous structures [53, 54, 55, 56]. In this dewetting instability regime, which is typically found for films with thickness $1 \leq h \leq 100$ nm, the formation of holes or bicontinuous structures occurs spontaneously and characteristic length scales emerge, because the subsequent dewetting dynamics is characterized by a narrow spread of preferential or fastest growing length scales [62, 63]. As shown theoretically, the dynamics leads to the selection of characteristic patterning length scales λ that vary with film thickness as $\lambda \propto h^2$ [62, 49, 40, 42], known as the classical dewetting behavior. This has been observed experimentally by several authors, verifying the existence of a spontaneous, self-organizing, spinodal-like process for polymeric [53, 42] as well as metallic films [46, 35, 37].

1.1.2 Dewetting mechanism through dissipation

As discussed in the previous section, the classical dewetting instability in thin films can be interpreted as a competition between two energy terms. For the case of a large number of polymer or metallic films studied, these two energies correspond to the surface tension and the attractive intermolecular dispersion force between the film-substrate and film-vacuum

interfaces mediated by the film material. As shown first by Vrij [62, 63], the instability can be described from an energetic viewpoint by evaluating the thermodynamic free energy change of the system under perturbations to the film height. The prediction from such an energy analysis is that for certain perturbation wave vectors, the film enters an unstable state and thus, can spontaneously dewet. As a result, studies of dewetting have focused largely on the fluid dynamics of the film, through which it is possible to obtain the relationship between the rate of growth or decay of surface perturbations to their wave vector, *i.e.* the dispersion relation. However, the fluid dynamics for even the simplest dewetting scenario, such as the example above, is a highly nonlinear process.Although this can be solved by many numerical techniques [33, 64, 65], a linear analysis is often employed to achieve physical insights into the dewetting process. An alternate approach to quantitatively evaluate dewetting is by thermodynamics. Fluid flow pathways can be analyzed through thermodynamic considerations, in which the conversion of useful internal energy to external energy loss via heat, such as by viscous dissipation, is used to quantify the behavior [66, 67].

Such an approach can provide meaningful insight into the nature of fluid flow as well as the energy pathway for dewetting instabilities. Specifically, the thermodynamic formulation can be applied to the case of dewetting, where film thickness dependent Marangoni or thermocapillary forces are also present. Such a situation has been observed in the melting of thin metallic films by nanosecond pulsed lasers [4, 1]. In this thermodynamic analysis the rate of thermodynamic free energy decrease due to film thickness fluctuations is balanced with the rate of energy loss due to viscous flow, i.e. viscous dissipation. This leads to an analytical description of the dewetting process without any need for linearization. The thermodynamic and linear approach show identical results for classical dewetting.

Dewetting mechanism can be understood by considering the energy transfer and/or energy conversion in systems during the liquid flow. Both the classical dewetting behavior

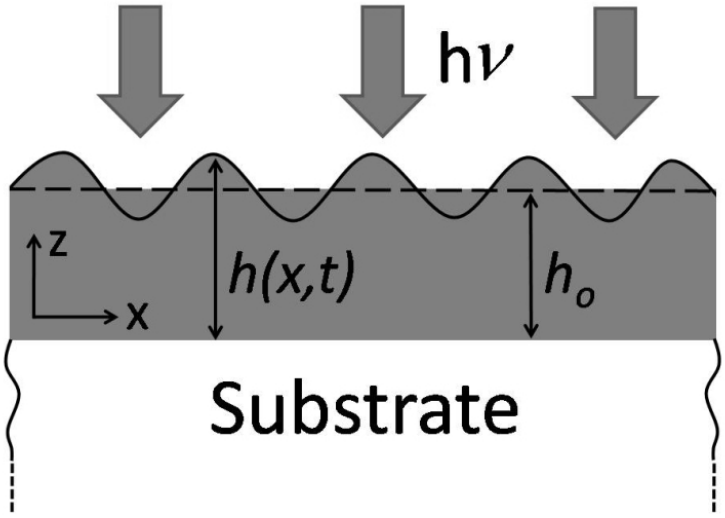

Figure 1.4: Schematic illustrating laser heating of ultrathin liquid films. A liquid metal film of initial height h_o undergoes surface height fluctuations due to capillary waves. This non-uniform height couples to the incident laser light and results in a local height-dependent temperature.

(as discussed in sec.1.1.1) as well as a substantially modified behavior (will be discussed in chapter 2) due to the nanosecond laser heating, can be understood on the principle of maximizing the rate of energy transfer between the thermodynamic state of the film and its viscous flow on the substrate. For an ultrathin metal film on an inert substrate such as glass (SiO_2), the total free energy of the system is made up of two terms: the surface/interface energies γ_{fv} and γ_{fs} of the film-vacuum and film-substrate interfaces respectively; and the disjoining pressure $\Pi(h_o)$, where h_o is the initial height of the film. The disjoining pressure $\Pi(h_o)$ is typically comprised of an attractive dispersive interaction between the metal film-substrate and film-vacuum interface of type $A/12\pi h_o^2$, where A is the Hamaker coefficient with a negative sign, and a short range repulsive term between the film and substrate atoms, typically given by B/h_o^n, where n is typically ≥ 4. For ultra thin films, the gravitational energy term is negligible, as is the short range repulsive term, and will therefore be ignored in the subsequent analysis. For such thin films, a height perturbation of the liquid film surface (see Fig. 1.4) , such as by capillary waves, results in a change in free energy. The contributions to this free energy change come from two terms. First, the area of the film

surface increases with respect to its original flat state for perturbations of any wavelength and hence the surface tension will contribute a positive term to the free energy change. Second, the attractive dispersion energy (which is proportional $\Pi(h_o)'' \propto 1/h_o^4$) contributes a large negative term. Therefore, the resulting total free energy change can be negative when the wavelength of the perturbation is of appropriate value, thus implying conditions for a spontaneous break-up of the liquid film [62]. In this situation, the characteristic patterning length scale λ is known to scale with the initial film thickness as $\lambda \propto h_o^2$ [63, 53]. As shown in this work (chapter 2 and 3), dewetting of metallic liquid films of nanometer thickness under nanosecond (ns) laser melting show this classical behavior as well as a substantially modified behavior, depending on the film thickness. Both these results can be understood by the principle of maximizing the rate of energy transfer between the thermodynamic state of the film and its viscous flow on the substrate.

The change in free energy per unit length can be evaluated from the difference in energies between the initial state h_o and a perturbed state $h(x,t)$, as depicted in Fig. 1.4. The perturbed height can be conveniently expressed as a Fourier component of type:

$$h(x,t) = h_o + \varepsilon e^{\sigma t} e^{-ikx} \tag{1.2}$$

where the perturbation has an amplitude of ε, a characteristic temporal decay rate σ and a corresponding wave vector k. In this 1-dimensional system, the temporal rate of change of free energy can be expressed as:

$$\dot{\Delta F} = \frac{\partial}{\partial t}[F(h) - F(h_o)] = \frac{\partial}{\partial t}[\frac{1}{2}\gamma \mid \frac{\partial h}{\partial x} \mid^2 + \frac{1}{2}\Pi'' \Delta h^2] \tag{1.3}$$

which, upon using, Eq. 2.1 and $\Pi'' = A/2\pi h_o^4$ gives:

$$\dot{\Delta F} = \sigma(\gamma k^2 + \frac{A}{2\pi h_o^4})\varepsilon^2 e^{2(\sigma t - ikx)} \tag{1.4}$$

Here, the first term on the right side is the rate of increase of surface tension energy due to increase in surface area of the film, while the second term, evaluated at the initial film height, is the rate of change in energy resulting from the dispersive interaction. From this, one can see that for attractive dispersive forces, *i.e.* A < 0, the second term in Eq. 3.1 competes with the surface tension term and could decrease the free energy depending on the value of k. This free energy behavior, which shows a negative curvature, is similar to the spinodal found in binary phase systems [52]. More importantly, it implies that the film will be unstable to perturbations of certain wave vectors k , creating the possibility of spontaneous dewetting and pattern formation. In order to evaluate the value of the patterning length scale $\lambda = 2\pi/k$ that actually dominates the dewetting process, the rate of free energy decrease $\dot{\Delta F}$ is compared with the rate of energy lost $\dot{E_V}$ due to viscous flow, in the presence of a film thickness-dependent temperature. These quantities allow one to evaluate the rate of viscous energy loss per unit length $\dot{E_V}$ occurring over the entire thickness of the liquid film due to the flow in the x-direction as [68]:

$$\dot{E_V} = \eta \int_0^{h_o} (\frac{dv_z}{dz})^2 dz \tag{1.5}$$

The above analysis was performed for dewetting of single layers of Co and Ag on SiO_2 substrates, as will be discussed in detail in chapter 2.

In contrast to the vast number of theoretical and experimental investigations for dewetting of single layer films, only a few theoretical studies have been performed for multiple film layers, such as bilayer polymer liquids on solid substrates [69, 70, 71, 72], using linear and non-linear analysis of the fluid flow equations. In this case, the instability characteristics were explained on the basis of different combinations of surface tensions of liquid layers and the solid surface. Depending on the ratio of the layer thicknesses and the van der Waals interactions between different interfaces, the system follow different pathways of dewetting [72, 69].

1.2 Nanomagnetism

Nanomagnetism is the area of research in physics which deals with the magnetic properties of objects that have at least one dimension in the nanoscopic range [73, 12]. The emergence of new phenomena in nanomagnetism results from important differences in nanoscopic and macroscopic samples [74, 75, 76, 77]. The nanoscopic objects: (i) have dimensions comparable to characteristic lengths, such as the limiting size of magnetic domains [78]; (ii) exhibit a higher proportion of surface or interface atoms compared to bulk. Another factor that modifies the magnetic properties of nanostructures is the close contact with other physical systems, for example, with a substrate in the case of most thin films, surface nanostructures and multilayers [73, 79, 80, 81]. In each case, the nanomagnet may feel a strong interaction with its immediate neighborhood. Also, in general, as nanoparticles are prepared with smaller dimensions, the presence of imperfections or anisotropies and defects becomes more relevant [82, 83].

Nanomagnetism includes the study of properties and applications of the magnetism of isolated or cluster of nanoparticles, nanodots, nanowires, thin films and multilayers [84, 73, 85]. In the last few decades tremendous progress has been made in the area of nanomanufacturing techniques including lithography and self-organization processes. In addition, the progress in magnetic characterization techniques *e.g.* magnetic and atomic force microscopy (AFM, MFM), magneto-optic Kerr effect (MOKE) and nano superconducting quantum interference device (nano SQUID), have made it much easier to study and understand nanomagnetism [86]. The magnetic nanostructures are characterized by a fascinating diversity of geometries, ranging from complex structures to a broad variety of small systems. The typical nanostructure geometries of interests are thin flat films, dots, nanowires, rings etc. First, the large surface-to-volume ratio of these elements lead to a comparatively strong size-dependence of the magnetic properties on surface and interface atoms. Also the ground-state domain configuration and the mechanism of magnetization reversal in small magnetic particles depend on the particle size and shape [76, 13, 12, 73, 78].

The total energy of a magnet includes the terms due to dipole interaction, shape anisotropy, crystal structure-related anisotropy or magnetocrystalline anisotropy, and the strain related magnetoelastic energy. These energy terms will be discussed in the next subsections, followed by the effect of size and shape of magnets on magnetic domains.

1.2.1 Dipole-dipole interactions

Magnetic dipole-dipole interaction refers to the direct interaction between two magnetic dipoles. Classically, the dipole-dipole interaction energy depends on the relative orientation of the magnetic moments. To obtain the dipolar interaction energy, consider the case for two magnetic dipoles, μ_1 and μ_2, held at a distance r at some angle between them. The dipole-dipole interaction energy per unit volume (E_{Dip}) can be expressed by the well known Eq. 5.9[87];

$$E_{Dip} = \frac{\mu_0}{4\pi V}\left[\frac{\boldsymbol{\mu_1}\cdot\boldsymbol{\mu_2}}{r^3} - 3\frac{(\boldsymbol{\mu_1}\cdot\mathbf{r})\,(\boldsymbol{\mu_2}\cdot\mathbf{r})}{r^5}\right] \tag{1.6}$$

where $\mu_1 = \mu_2 = M_0 V$, where V is the particle volume and M_0 the saturation magnetization [87]. As can be seen in the above equation, the interactions energy is proportional to the field strength, which falls off as $1/r^3$, and is highly dependent on the angle between the dipoles. In the present work, the interaction energies associated with the neighboring nanomagnets are considered and evaluated in chapter 5.

1.2.2 Magnetocrystalline anisotropy energy

For a single crystalline ferromagnet, the magnetic energy will be the lowest when the magnetization aligns along the easy axis, determined by the magnetocrystalline anisotropy. However, for the polycrystalline magnets, the magnetocrystalline anisotropy will be averaged out over all grains orientated in different directions, resulting in a weaker anisotropy [88]. For a polycrystalline cubic crystal with n number of grains, the magnetocrystalline

energy density (E_{MA} per unit volume) is given by [85]:

$$E_{MA} = \frac{1}{n}\sum_{i=1}^{n} K_1 \left[\frac{\sin^4(\alpha_i-\beta)\cdot\sin^2 2\phi}{4} + \cos^2(\alpha_i-\beta)\cdot\sin^2(\alpha_i-\beta)\right]$$

$$+\frac{1}{n}\sum_{i=1}^{n}\frac{K_2\sin^2 2\phi\cdot\sin^2 2(\alpha_i-\beta)}{16} \tag{1.7}$$

where K_1 and K_2 are the second and third order magnetocrystalline anisotropy constants. The grain orientation α_i, is the angle between the easy axis of the i^{th} grain with the substrate plane, β is the magnetization direction and ϕ is the azimuthal angle. The order of magnitude for E_{MA} depend on the number of grains (n) and the grain orientation [88], which depends on the actual microstructure of the magnetic particle. For example, particles made of a single grain will have the highest magnetocrystalline energy, compared to randomly oriented multiple grained particles of the same shape and size [88].

1.2.3 Demagnetization energy or shape anisotropy

The demagnetization energy or shape anisotropy is measured by the magnetic energy of a sample due to its own magnetic field (H_d). The demagnetization energy density E_{DM}, is given by:

$$E_{DM} = -\frac{1}{2V}\mu_o\int_V H_d\cdot M\,dV$$

where the integral is performed over the volume, V , of the sample. The magnetostatic energy of samples of ellipsoidal shape is simple to calculate since the magnetic field is the same at every point of the sample. However, the hemispherical shape, as in the present work, introduces complications due to the presence of truncated surface. The demagnetization energy per unit volume (E_{DM}) as a function of magnetization direction (β, w.r.t substrate plane) can be estimated for single domain hemispherical particles using the approach outlined in ref. [89], assuming uniform magnetization of the hemispheres. The calculation was performed by first evaluating the magnetic scalar potential (Φ_M) using general spherical harmonics (Y_{lm}). The final expression for the hemispherical demagnetization energy

per unit volume was obtained as [85]:

$$E_{DM} = \mu_0 M_0^2 \left(100 - 9\cos 2\beta\right)/768 \tag{1.8}$$

where, $\mu_0 = 4\pi \cdot 10^{-7} Wb/A \cdot m$ and M_o is the saturation magnetization.

1.2.4 Magnetostrictive energy

The magnetostrictive energy (or magnetoelastic energy) of a ferromagnetic solid arises from the interaction between the magnetization and the strain (ε) [90, 91]. Magnetostriction is a measure of change in dimensions of a solid as its magnetic state is changed. This energy basically introduces an additional extrinsic anisotropy due to strain, similar to the anisotropy introduced by shape. Using the magnetostriction and the stress or strain, the magnetostrictive energy density E_{MS} can be calculated using the relation [92];

$$E_{MS} = (3/2)\lambda\varepsilon(c_{11} - c_{12})[1 + (2c_{12}/c_{11})]cos^2\beta \tag{1.9}$$

where λ is the magnetostriction constant, ε is the thermal strain, c_{11} and c_{12} are the elastic stiffness constants and β is the direction of magnetization.

1.2.5 Magnetic domain size

To minimize the demagnetization energy, the macroscopic samples of magnetic materials break up into regions of uniform magnetizations with opposite spins, called magnetic domains, separated by domain walls or transition regions over which the magnetization changes direction [12, 93, 77]. When the nanoparticle size approaches the width of the domain walls, determined by the magnetic exchange and anisotropy energies, the particles become single domain (SD). This domain transition can be predicted by comparison of the magnetostatic energy of a uniformly magnetized particle (proportional to its volume) to the

domain wall energy of a multi-domain state (proportional to the particle surface) [13].

In addition to the size, effect of shapes is also important in magnetism of low dimensional objects, such as nanodisks, nanorings or nanowires. In some aspects, the magnetism of these objects is comparable to the magnetism of nanoparticles, and therefore, what is applicable to nanoparticles is also valid for nanodisks, nanorings, and nanowires. On the other hand, the fact that the nanoscopic disks and rings are approximately bi-dimensional, justifies why some results for extended thin films are also relevant for them

Thin magnetic disks, or circular dots of thickness of the order of the exchange length, exhibit a vortex spin structure. The magnetization is mostly confined to the plane of the disk and the vortex center is located near the center of the disk with magnetization normal to the disk plane [94, 95]. This perpendicular magnetization of the vortex core is verified experimentally through images of nanodisk arrays obtained using magnetic force microscopy (MFM), that shows dark or bright dots at the center of the disks [94], arising from the uncompensated magnetic poles, indicating up or down vortex core magnetization.

In the case of nanorings, the possible magnetic states are vortex, onion or twisted state [96]. In the vortex case, the directions of local magnetization turn around the annular part,where the magnetization is tangential to the perimeter of the nanoring, forming a vortex magnetic state. A second common magnetic configuration is an arrangement of spins in which the ring is divided into two magnetic domains, with magnetizations oriented tangentially in two different directions, clockwise and counterclockwise, a structure that is usually referred to as an onion state [97]. A third common structure is an asymmetric onion state or twisted state, containing two regions of opposite direction of rotation and different lengths, and is referred to as a twisted state [97].

Due to shape anisotropy, nanowires, especially single crystalline nanowires, usually favor the alignment of the magnetization along the axis of the wire [98]. However, for polycrystalline nanowires, depending on the crystallographic orientation of the grains, the magnetization may also point perpendicular to the axis [5]. In both cases, imperfections,

such as defects, kinks and bends in the nanowires, may lead to domain wall pinning and affect the size, shape, and orientation of each domain.

1.3 Outline of dissertation

The dissertation presents detailed study of self-organization in thin liquid metal films using *ns* pulsed laser to create ordered metallic nanostructures on semiconductor surfaces and its characterizations. The experimental observations are supported by the theoretical analysis of SO mechanisms. In addition, exhaustive studies have been done on the magnetic properties of ferromagnetic structures.

- CHAPTER 2: The thermodynamic theory of spinodal dewetting in single layers is presented. It was shown theoretically that the self-organization principle based on the rate of transfer of free energy equal to the minimum value of the viscous dissipation during liquid flow, accurately describes the characteristic scales of spontaneous spinodal dewetting [1]. This principle was also applied to the case of dewetting in the presence of intrinsic thermocapillary forces generated by nanosecond pulsed laser melting. The results agree well with the experimental observations of pulsed laser dewetting of Ag and Co on SiO substrates.

- CHAPTER 3: Similar to the single metal layer, theoretical and experimental dewetting studies have been performed in bilayer metal systems. To experimentally study the dewetting in bilayers, the immiscible metals Ag and Co were chosen on SiO_2 substrates. The theoretical analysis of dewetting in bilayer was performed using the thermodynamic approach. The characteristic length scales predicted by this theory show different behavior for different configurations of bilayers of Ag and Co on SiO_2 substrates (*e.g.* Ag/Co/SiO_2 and Co/Ag/SiO_2). This difference in length scale was explained by the differences in the sign and magnitude of the intermolecular forces for the two arrangements. The experimental length scale behavior for both the con-

figurations was consistent with theory. Nanostructural studies were also performed on the nanoparticles created by laser processing of bilayer Ag-Co thin films on SiO_2.

- CHAPTER 4: The particular morphology selected by a polymer film during spinodal dewetting has been predicted to be related to the functional form of the free energy and its curvature [33, 42]. In this chapter, we have investigated this characteristic for metallic films. The morphological pathway of dewetting in ultrathin Ag films on SiO_2 in the thickness range of $2 \leq h \leq 20$ nm was investigated. The morphology consisted of an intermediate stage of bicontinuous structures for the thinner films $h \leq 9.5$ nm, and regularly-sized holes or polygons for films $11.5 \leq h \leq 20$ nm. This behavior can be explained by the curvature of the free energy.

- CHAPTER 5: The magnetic properties of hemispherical shape nanomagnets of elemental Co and Fe prepared by pulsed laser dewetting is presented[85, 99]. . Magnetic force microscopy (MFM) and hysteresis loop measurements were done to characterize these nanomagnets. In the single domain size range, the magnetic behavior of these particles show size-dependent magnetic orientations, where smaller particles are in-plane with respect to the substrate plane and bigger particles show out-of-plane magnetization directions. The size-dependent magnetic direction of the nanomagnet was explained by the size-dependent residual strain and the microstructures formed by rapid laser processing *[85]*.

- CHAPTER 6: The magnetic properties of spatially ordered patterns of hemispherical nanoparticles of elemental ferromagnets Co, Ni, was compared to nanoparticles of an alloy ($Fe_{50}Co_{50}$) and a mixture ($Cu_{50}Co_{50}$), synthesized on SiO_2 substrates. Magnetic force measurements reveals the predominantly out-of-plane magnetization direction of Co and Ni nanoparticles, as compared to in the plane behavior for the $Fe_{50}Co_{50}$ and $Cu_{50}Co_{50}$ nanoparticles. The difference in the magnetic behavior was attributed to the dominating influence of magnetostrictive energy due to the differ-

ence in the signs of magnetostriction coefficients. The magnitudes of each of the magnetic energy terms was calculated for hemispherical shape Co, Ni elemental ferromagnets as well as for alloys (FeCo) and mixtures (CuCo) nanomagnets.

- CHAPTER 7: Here, a summary of this dissertation research as well as some directions for future work on magnetism and self-organization are given.

Chapter 2

Thermodynamic theory of self-organization in single layer thin metallic liquid films

Summary

Nanometer thick metallic liquid films on inert substrates can spontaneously dewet and self-organize into complex nanomorphologies and nanostructures with well-defined length scales. Nanosecond pulses of an ultraviolet laser can capture the dewetting evolution and ensuing nanomorphologies as well as introduce dramatic changes to dewetting length scales due to the nanoscopic nature of film heating. The physical manifestation of the instability in terms of characteristic length and time scales can be described by a linearized form of the initial conditions of the non-linear film's dynamics. Alternately, a thermodynamic approach based on equating the rate of free energy decrease to the viscous dissipation can give similar information. Here the theoretical model show that the self-organization principle based on equating the rate of thermodynamic free energy change with viscous loss during liquid flow accurately describes the spontaneous dewetting. The results of this approach agree with those from linear analysis and experimental observations provided the

rate of decrease in free energy is equated to the minimum value of viscous dissipation. The flow boundary condition that produces this minimum viscous dissipation is when the film-substrate tangential stress is zero. Experimental measurements of laser dewetting of Ag and Co liquid films on SiO_2 substrates were used to confirm this principle. This energy transfer approach could be useful towards analyzing materials and chemical processes as well as behavior of nanomaterials in which spontaneous changes are important.

2.1 Introduction

Understanding the mechanism(s) of energy transfer and/or energy conversion in systems involving nanoscale materials is important for several reasons. This could lead to discovery of new and improved materials for many applications. Such applications include, solar energy harvesting [100, 101], sensing [102, 103], optical or magnetic information processing [25, 26, 85, 104], biomedicine [105, 106], spintronics [107] and surface enhanced Raman scattering (SERS) [100, 101, 102, 103]. One class of materials that can be used in several of these applications is surface nanostructures made from complex shapes and/or specific sizes of various metals. Such nanostructures could be achievable in an economical and reliable manner if chemical and materials processing principles involving spontaneous pattern formation, such as self-assembly or self-organization, are fully realized [108]. One such technique that could be harnessed to create complex nanostructures from thin films is the spontaneous self-organization of thin liquid films that lead to nanostructure formation on surfaces (Fig. 2.1). The extensive studies of this technique in polymer thin films and growing number of investigations of dewetting in metallic thin films is indicative of technological interest and also to the need for a deeper understanding of the phenomenon [53, 42, 109, 110]. It is for these reasons that investigating and understanding the dewetting mechanisms in thin metal films has gained attention [111, 112, 113, 37].

As mentioned in chapter 1, the theoretical understanding of the dewetting and dynamics in thin liquid films has been primarily investigated by analyzing the non-linear mass transport equations [71, 37], which is often evaluated through a linear analysis in order to achieve physical insights into dewetting. An alternate approach to quantitatively evaluate dewetting is thermodynamics. Fluid flow pathways can be analyzed through thermodynamic considerations in which the conversion of useful internal energy to external energy loss via heat, such as by viscous dissipation, can be used to quantify the behavior [114]. The dewetting of metallic liquid films of nanometer thickness under nanosecond (ns) laser melting show both the classical spinodal dewetting behavior as well as a substantially mod-

ified behavior due to the nanosecond laser heating. *Both these results can be understood on the principle of balancing the rate of free energy change of the thermodynamic state of the film to the dissipation due to viscous flow on the substrate.* It has been shown previously that melting of thin metal films by ultraviolet light (UV) from a nanosecond pulsed laser permits one to quench-in various stages of the dewetting morphology and therefore enables a highly accurate and quantitative understanding of the dewetting process [48, 37]. Furthermore since this laser dewetting is a result of nanometer-thin films interacting with ns light of wavelength 266 nm, which is strongly absorbed within nanometer length scales by metals, interesting thermal effects have been observed in the film [4]. Consequently, a novel dewetting behavior, in which a dramatic change in the spontaneous patterning length scale can be observed [4], has been reported. However, the previous understanding of dewetting in thin metal films has focused primarily on the mechanism of mass transport in the dewetting process [35].

It is shown here via experiment and theory, that dewetting can be accurately described by equating the rate of thermodynamic free energy change to energy lost during liquid flow. Ag and Co were chosen for their strong plasmonic and ferromagnetic responses [85], respectively, as well as due to the large differences in thermal diffusivity ($D_{Ag}^{Th} >> D_{Co}^{Th}$). The dewetting of Ag and Co was investigated in a thickness regime spanning 2 to 15 nm. In the case of Ag, only the classical spinodal behavior was observed, while for Co, the classical behavior, as well as a modified dewetting regime was observed. These experimental results could be explained by the thermodynamic theory suggesting that a principle based on balancing the rate of free energy change with could be used to describe nanoscale processing in which dynamical effects lead to robust pattern formation, such as in dewetting of thin metallic films.

2.2 Experimental details

Thin films of Ag of thickness h_o from $\sim$4 to 12 nm and Co from $\sim$2 to 15 nm were deposited on SiO_2 substrates by pulsed laser deposition and electron beam evaporation techniques, respectively, under high vacuum ($\sim 1 \times 10^{-8}\, Torr$) at room temperature [4, 37, 35]. The substrate was commercial available optical quality SiO_2/Si wafers consisting of 400 nm thick thermally grown oxide layer on polished Si(100) wafers. Prior to evaporation, the substrates were cleaned by ultrasonic rinsing in acetone, ethanol and DI water. The final thickness was verified by an in-situ Inficon XTM/2 deposition monitor and by thickness calibrated measurement of the Co and Ag signal counts from energy dispersive x-ray spectrometry (EDS) in a scanning electron microscope (SEM) [37]. Following deposition, each film thickness was irradiated under vacuum at normal incidence by multiple pulses with a uniform Nd:YAG laser beam having a Gaussian shaped pulse of 9 ns width, 266 nm wavelength and 50 Hz repetition rate. The laser energy density was chosen to be just above the film melt threshold, which is required to achieve the self-organization [35], and typically varied between 100 to 300 mJ/cm^2. The resulting dewetting nanomorphology for each film thickness was measured as a function of the number of laser pulses (n) by scanning electron microscopy (SEM) and atomic force microscopy (AFM).

2.3 Results and discussion

Fig. 2.1 shows composite images of the typical dewetting nanomorphologies for a 10 nm Ag film as a function of n. The images were generated by combining SEM micrographs with input on height information from AFM. At early stages (n$\sim$10 pulses) a narrow size-distribution of holes was evident (Fig. 2.1(a)), with polygonal structures (Fig. 2.1(b)) appearing at later stages (n$\sim$1000) which eventually changed into nanoparticles (Fig. 2.1(c)), which was the final stable state after long irradiation times (n$\sim$10,000 pulses). Besides the complex morphologies which could be repeatable obtained, another important observation

was that at each stage of the dewetting pattern a characteristic length scale was present, as evident and quantifiable by the ring-like radial distribution function (inset of each figure) that measured the correlation between contrast in the images. From such measurements, a characteristic dewetting length scale was defined as the nearest neighbor particle spacing λ and its behavior as a function of film thickness for Ag and Co films is plotted in Fig. 2.3(a) and (b) respectively. While Ag films follow a smooth trend that can be fitted to a $\lambda \propto h_o^2$ behavior, consistent with the classical spinodal dewetting process, Co films showed a dramatic change in behavior for thickness > 8 nm. As shown here, this modified dewetting behavior can be explained by equating the rate of thermodynamic free energy with frictional loss in energy due to viscous liquid flow under conditions of surface temperature gradients that develop in the liquid film due to nanoscale laser heating.

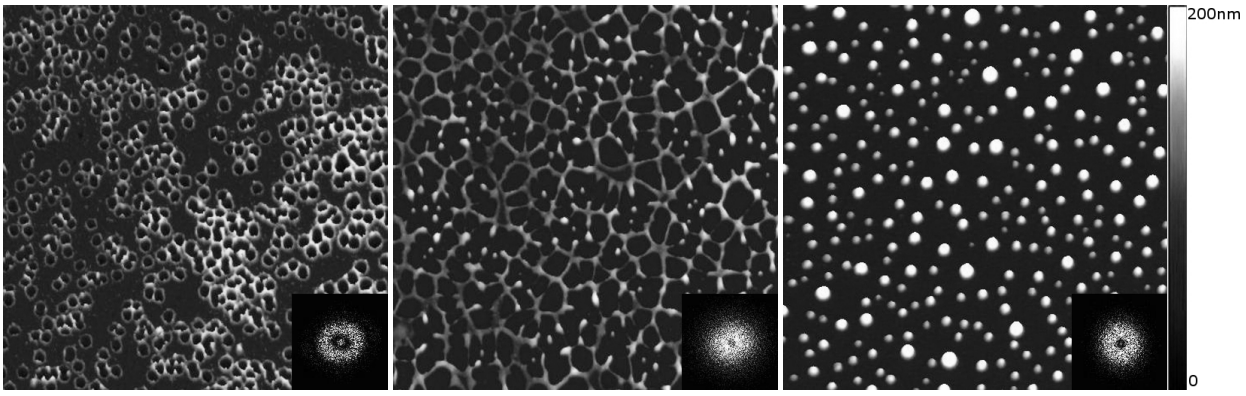

(a) (b) (c)

Figure 2.1: The characteristic nanomorphologies following nanosecond pulsed laser-induced spontaneous dewetting and self-organization of ultrathin Ag metal film on SiO_2 substrates. (a) At early stages of dewetting (irradiation by n$\sim$10 laser pulses), holes with a narrow size distribution are visible (as evident from the ring-like power spectrum in the inset). (b) Later stage dewetting (n$\sim$1000 pulses) leads to the formation of polygonal features which also have with a narrow size distribution (power spectrum in inset). (c) The final stable dewetting state (n$\sim$10,000 pulses) consists of nanoparticles with a well defined nearest-neighbor spacing. Each image is of dimension $8 \times 8\,\mu m^2$ and contains information about length (from scanning electron microscopy) and height (from Atomic force microscopy and shown by the color bar on the right).

A transient intrinsic thermal gradient develops along the liquid surface due the strong thickness-dependent ns laser heating of such nanoscopic metals films [4, 37]. This thickness-

dependence arises from three effects, each of which is described here qualitatively. Firstly, the skin depth of 266 nm wavelength UV light in metals typically ranges 3 to 12 nm, which is the range of film thickness investigated here. Consequently, the intensity of light absorbed will be a function of the film of thickness h_o and can be expressed as $I(h_o) = I_o(1 - e^{-\alpha(\lambda)h_o})$, where I_o is the incident light intensity and $\alpha(\lambda)$ is the wavelength-dependent absorption coefficient in the metal film. Secondly, the effective reflectivity of light from the surface of the metal film on the SiO_2 substrate is also strongly thickness dependent. This can be understood physically by noting that at zero film thickness the reflectivity will be that of the SiO_2 substrate (which is practically zero for UV light) while it will be the value of the bulk metal (which is >> zero) for a very thick film. From quantitative calculations based on evaluating the Fresnel coefficients for such metal/SiO_2 bilayer systems, the general nature of the thickness dependent reflectivity for metals can be found to be $R(h_o) = r_o(1 - \exp(-a_r h_o))$, where a_r and r_0 are materials-dependent parameters [115]. Third, the effective mass of the material heated $M(h_o)$ is also a strong function of film thickness for the following reason. Due to the large thermal conductivity of metals, any heat generated within the nanoscopic metal film due to optical absorption will diffuse into the underlying SiO_2 substrate. Consequently, the effective mass of material heated will include the thermal mass of the film and an effective thermal mass of the substrate estimated from the length scale of thermal diffusion occurring within the substrate in the nanosecond time scales of the experiment. Therefore, the heated mass will be $M(h_o) = (\rho C_p)_m h_o + (\rho C_p)_S \sqrt{D_S^{th}\tau}$, where the subscript m and s denote metal and substrate while ρ and C_p are values of density and specific heat, D_S^{th} is the substrate thermal diffusivity and τ is the ns time scale of laser heating. Consequently, energy balance shows that the temperature rise will be qualitatively given by $\Delta T(h_o) = I(h_o)(1 - R(h_o))\tau / M(h_o)$. As can be noted, in this function, I increases with increasing thickness while (1-R) and 1/M decrease with increasing thickness. As a result, a non-monotonic variation in temperature with film height h_o can be expected for any given laser intensity and in fact at a critical film

thickness $h*$ the temperature rise will be a maximum. Furthermore the position of this $h*$ will depend strongly on the laser energy density, which controls the rate at which the film gets heated and hence effects the time scale τ. The T vs h_o behavior was estimated using a previously developed heating model based on 1D heat transport into the substrate, i.e. a *localized* heat absorption and heat transfer [37]. In this model the film temperature is uniform in a direction perpendicular to the film thickness and the model has accurately predicted the thickness-dependent laser energy density required to melt the films [37]. In Fig. 2.2(b) representative T vs h_o plots are provided for Ag and Co films evaluated from this model for laser energy densities of 140 mJ/cm^2 and 250 mJ/cm^2 respectively. As is evident, a non-monotonic behavior with a critical $h*$ is seen for both films. Based on this behavior, it was suggested previously that transient temperature differences can exist *along the plane* of the liquid film, thus leading to intrinsic thermocapillary forces that could contribute to the patterning process [4]. This gradient can be understood as follows: within a single laser pulse the film melts at some fraction of the pulse time and therefore the liquid continues to interact with the pulse. Subsequently, height fluctuations of the liquid surface due to capillary waves interact with the laser light to produce local thickness-dependent temperatures, and hence the temperature gradients along the liquid film surface. It is this gradient that subsequently influences dewetting, as shown here via theoretical analysis based on the thermodynamic principle stated earlier.

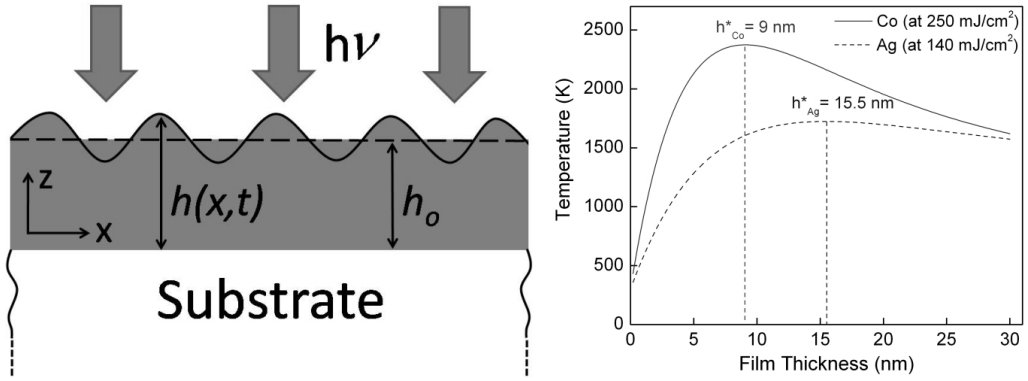

(a) (b)

Figure 2.2: (a) Schematic figure illustrating laser heating of ultrathin liquid films. A liquid metal film of initial height h_o undergoes surface height fluctuations due to capillary waves. This non-uniform height couples to the incident laser light and results in a local height-dependent temperature. (b) Film temperature, calculated using a local heating model, for Ag and Co metal films on SiO_2 as a function of thickness h_o following heating by a 9 ns ultraviolet laser of 266 nm wavelength of energy density 140 and 250 mJ/cm^2 respectively. A non-monotonic change in T with h_o is evident as is the critical thickness $h*$ at which the sign of the gradient T_h changes . Consequently, this T vs h_o behavior results in a positive surface temperature gradient T_h for the perturbed film (shown in a) whose initial thickness $h_o < h*$ and negative gradients for perturbed films whose $h_o > h*$. This intrinsic thermal gradient can substantially modify the length scale of dewetting from its classical values [4].

2.4 Thermodynamic theory

The change in free energy per unit length can be evaluated from the difference in energies between the initial state h_o and a perturbed state h(x,t), as depicted for 1D in Fig. 2.2(a). The perturbed height can be conveniently expressed as having a Fourier component of type:

$$h(x,t) = h_o + \varepsilon e^{\sigma t} e^{-ikx} \tag{2.1}$$

where the perturbation has an amplitude of ε, a characteristic temporal decay rate σ and a corresponding wavevector k. In this 1D system, the temporal rate of change of free energy can be expressed as [62, 63]:

$$\dot{\Delta F} = \frac{\partial}{\partial t}[F(h) - F(h_o)] = \frac{\partial}{\partial t}[\frac{1}{2}\gamma \mid \frac{\partial h}{\partial x} \mid^2 + \frac{1}{2}\Pi'' \Delta h^2] \tag{2.2}$$

which, upon using, Eq. 2.1 and $\Pi = A/12\pi h^2$ gives:

$$\dot{\Delta F} = \sigma(\gamma k^2 + \frac{A}{2\pi h_o^4})\varepsilon^2 e^{2(\sigma t - ikx)} \tag{2.3}$$

Here, the first term on the right side is the rate of increase of surface tension energy due to increase in surface area of the film, while the second term, with $\Pi'' = A/2\pi h_o^4$ evaluated at the initial film height, is the rate of change in energy resulting from the dispersive interaction. From this one can see that for attractive dispersive forces, i.e. A < 0, the second term in Eq. 3.1 competes with the surface tension term and could decrease the free energy depending on the value of k. This free energy behavior, which shows a negative curvature, is similar to the spinodal found in binary phase systems. More importantly it implies that the film will be unstable to perturbations of certain wavevectors k thus implying the possibility of spontaneous dewetting and pattern formation. In order to evaluate the value of the patterning length scale $\lambda = 2\pi/k$ that actually dominates the dewetting process, the rate of free energy decrease in comparison to the rate of energy lost $\dot{E_V}$ due to frictional effects associated with the viscous flow of the liquid metal film with a film thickness-dependent temperature was explored. As has been shown in the past, flow in thin liquid films can be described by the thin film form of the Navier-Stokes (NS) equation [116]. For such thin films, viscous forces dominate inertial forces and so the 1D form of the NS describing liquid flow with velocity v in the x-direction due to a pressure gradient $\nabla P = \frac{dP}{dx}$ along the x-direction can be expressed as [116]:

$$v = \nabla P \frac{z^2}{2\eta} + Az + B \tag{2.4}$$

where v is the z-variation (in the direction of film height) of the liquid velocity, η is the dynamic viscosity, $\nabla P = \frac{dP}{dx}|_{h_o}$ is the gradient in pressure along the x-direction evaluated

at the film surface, and A and B are constants related to the boundary conditions. For the general flow situation being considered here, the liquid does not slip in contact with the stationary substrate was assumed, and so $v(h=0)=0$ resulting in $B=0$. For the top surface of the liquid a local thickness dependent temperature T(h,x) was considered that results from the thickness-dependent heating of the metal films by the UV laser, as described above [37]. In order to satisfy the stress-free boundary condition at the top film surface, $\eta\frac{dv}{dz}|_{h_0} = -\frac{d\gamma(T,x)}{dx} = -\mid\gamma_T\mid T_h\frac{dh}{dx} = -(\mid\gamma_T\mid T_h h')|_{h_o}$, where: $\gamma(T,x)$ is the temperature and position dependent surface tension of the film-vapor interface; $\mid\gamma_T\mid=\mid\frac{d\gamma}{dT}\mid$, is the magnitude of the temperature coefficient of surface tension; $T_h = \frac{dT}{dh}$ is the laser-induced temperature gradient along the film surface due to thickness variations; and $\frac{dh}{dx} = h'$ is the thickness gradient along the flow direction, with all quantities evaluated at the film surface. From this, the velocity and velocity gradient in the film height direction can be expressed as:

$$v = \frac{\nabla P}{\eta}(\frac{z^2}{2} - h_o z) - \frac{\mid\gamma_T\mid T_h h'}{\eta}z \tag{2.5}$$

and

$$\frac{dv}{dz} = \frac{\nabla P}{\eta}(z - h_o) - \frac{\mid\gamma_T\mid T_h h'}{\eta} \tag{2.6}$$

These quantities allow us to evaluate the rate of viscous energy loss per unit volume $\dot{e}_v$ occurring over the entire thickness of the liquid film due to flow in the x-direction as follows. The total dissipation per unit volume of film is given by [68]:

$$\dot{e_V} = \eta(\frac{dv}{dz})^2 = \frac{\nabla P^2}{\eta}(z-h_o)^2 - 2\nabla P\frac{\gamma_T T_h h'}{\eta}(z-h_o) + \frac{(\mid\gamma_T\mid T_h h')^2}{\eta} \tag{2.7}$$

As will be shown shortly, the minimum rate of viscous dissipation is needed for the thermodynamic principle to successfully yield results similar to those previously obtained by linear analysis. For the fluid being subjected to pressure gradients, this can be estimated

from the differential condition $d\dot{e}_v/d\nabla P = 0$, which gives:

$$\frac{d\dot{e}_V}{d\nabla P} = \frac{d}{d\nabla P}(\eta(\frac{dv}{dz})^2) = \frac{2\nabla P}{\eta}(z-h_o)^2 - 2\frac{\gamma_T T_h h'}{\eta}(z-h_o) = 0 \tag{2.8}$$

leading to the condition:

$$\nabla P(z-h_o) = \mid \gamma_T \mid T_h h' \tag{2.9}$$

From this is is seen that the minimum dissipation occurs when the pressure gradient ∇P is related to the thermal stress due to temperature gradients. In order to identify the appropriate form of this relation, the behavior for various values of $z-h_o$ needs to be evaluated. It can be immediately noted that the choice of $z = h_o$ does not yield a unique relation between ∇P and $\mid \gamma_T \mid T_h h'$. Likewise, the general value of $z-h_o$ results in the total dissipation $\dot{e}_v = 0$, as can be noted by using Eq. 2.9 in Eq. 2.7. On the other hand, the choice of $z = 0$, yields the useful case of $\nabla P = -\frac{|\gamma_T| T_h h'}{h_o}$. By utilizing Eq. 2.6, one can see that the physical interpretation of this condition is that the tangential stress at the film-substrate interface at z=0 is zero. The resulting viscous dissipation for thermocapillary dewetting will now be:

$$\dot{e_v} = \frac{(\nabla P z)^2}{\eta} \tag{2.10}$$

One can also verify that this is a minima by noting that the second derivative $d^2\dot{e}_v/d^2\nabla P$ is positive. Therefore, the minimum dissipation rate per unit area of the film $\dot{E}_v^m$ can be obtained by integrating over the film height and is given by:

$$\dot{E}_v^m = \int_o^{\dot{h}_o} \frac{(\nabla P z)^2}{\eta} dz = \frac{(\nabla P)^2 h_o^3}{3\eta} \tag{2.11}$$

The next step in evaluating this integral is to relate the pressure gradient to the film height through volume conservation arguments. Volume conservation requires that the rate of

change of film height $\partial h/\partial t$ be related to the flux of liquid flow $J(x)$ as $\partial h/\partial t = -\nabla . J(x)$. For this, he thin film lubrication approximation is used, in which flux can be written in terms of the height-averaged liquid velocity $< v >$ as [116]:

$$J(x) = h_o < v >= h_o.(\frac{1}{h_o}\int_0^{h_o} vdz) = -\frac{\nabla P}{3\eta}h_o^3 - \frac{\mid \gamma_T \mid T_h h' h_o^2}{2\eta} \tag{2.12}$$

from which, the volume conservation equation is:

$$\frac{\partial h}{\partial t} = -\nabla .J = \frac{\nabla^2 P}{3\eta}h_o^3 + \frac{\mid \gamma_T \mid T_h h'' h_o^2}{2\eta} \tag{2.13}$$

By rearranging terms, the desired relation for the pressure gradient is obtained as:

$$\nabla p = \int \nabla^2 P dx = \frac{i}{k}(\frac{3\eta\sigma}{h_o^3} + \frac{3 \mid \gamma_T \mid T_h k^2}{2h_o})\varepsilon e^{\sigma t - ikx} \tag{2.14}$$

where the Fourier form of the height perturbation of $h = h_o + \varepsilon e^{\sigma t - ikx}$ has been used. By substituting Eq. 2.14 into Eq. 2.11, the final expression for the minimum viscous energy loss in the film is:

$$\dot{E_v^m} = -\left(\frac{3\eta}{h_o^3 k^2}\sigma^2 + \frac{3 \mid \gamma_T \mid T_h}{h_o}\sigma + \frac{3(\mid \gamma_T \mid T_h)^2 k^2 h_o}{4\eta}\right)\varepsilon^2 e^{2(\sigma t - ikx)} \tag{2.15}$$

Using the principle that the rate of free energy change $\dot{\Delta F}$ is balanced by the minimum dissipation $\dot{E_V^m}$, the dispersion relation, which expresses the rate of deformation of film height σ to the wavevector of the surface perturbation k is obtained from Eq.'s 2.3 and 2.15 as:

$$\sigma^2 + \frac{h_o^3 k^2}{3\eta}(\gamma k^2 + \frac{A}{2\pi h_o^4} + \frac{3 \mid \gamma_T \mid T_h}{h_o})\sigma + \frac{h_o^3 k^2}{3\eta}\frac{3}{4\eta}(\mid \gamma_T \mid T_h)^2 h_o k^2 = \sigma^2 + B\sigma + C = 0 \tag{2.16}$$

This quadratic relation between σ and k obtained by maximizing the rate of free energy change for dewetting in the presence of a temperature gradient is the central theoretical result of this chapter. In order to understand the physical implications of this result, the dispersion relation has been evaluated for the spontaneous dewetting process for distinct thermal gradient scenarios.

This quadratic equation with coefficient B and C has roots given by:

$$\sigma_{\pm} = -\frac{B}{2} \pm \frac{1}{2}\sqrt{B^2 - 4C} \tag{2.17}$$

By defining $dF = \gamma k^2 + A/2\pi h_o^4$ and $dG = (3 \mid \gamma_T \mid T_h)/h_o$, the general form of Eq. 2.17 is:

$$\sigma_{\pm} = -\frac{h_o^3 k^2}{6\eta}(dF + dG) \pm \frac{h_o^3 k^2}{6\eta}\sqrt{(dF + dG)^2 - dG^2} \tag{2.18}$$

Next, σ has been used to obtain the characteristic wavevectors k^* from the condition $d\sigma/dk = 0$ for several useful cases.

Case 1: No thermal gradients In this situation, $T_h = 0$ and so $dG = 0$ and Eq. 2.18 gives:

$$\sigma_{-} = -\frac{h_o^3 k^2}{3\eta}(\gamma k^2 + \frac{A}{2\pi h_o^4}); \; and \; \sigma_{+} = 0 \tag{2.19}$$

and using $d\sigma_{-}/dk = 0$

$$k*^2 = \frac{4\pi^2}{\lambda_C^2} = -\frac{A}{4\pi\gamma h_o^4} \tag{2.20}$$

it gives the classical values for the characteristic dewetting wavelength λ_C and dewetting timescale (τ_C) as [63]:

$$\lambda_C = \sqrt{-\frac{16\pi^3\gamma}{A}}h_o^2 \tag{2.21}$$

$$\tau_C = \frac{96\pi^3\gamma h_o^5}{A^2} \tag{2.22}$$

Case 2: Weak thermal gradients For the situation when the thermal gradients are small in comparison to the free energy change, i.e. $\mid dG \mid < \mid dF \mid$, Eq. 2.18 can be

approximated as follows:

$$\sigma_{\pm} \approxeq -\frac{h_o^3 k^2}{6\eta}(dF+dG) \pm \frac{h_o^3 k^2}{6\eta}\sqrt{dF^2-dG^2} \approxeq -\frac{h_o^3 k^2}{6\eta}(dF+dG) \pm \frac{h_o^3 k^2}{6\eta} dF(1-\frac{dG^2}{2dF^2}) \tag{2.23}$$

where the binomial approximation $(1-(dG/dF)^2)^{1/2} \sim (1-dG^2/2dF^2)$ has been used.

Case 3: Strong thermal gradients In the case when the magnitudes of the thermal gradients are large, i.e. for instance when $3 \mid \gamma_T T_h \mid \geq \mid A/2\pi h_o^3 \mid$, then $\mid dG \mid > \mid dF \mid$. This condition is the experimental case presented in this work and an approximate solution can be obtained from Eq. 2.18 as follows:

$$\sigma_{\pm} \approxeq -\frac{h_o^3 k^2}{6\eta}(dF+dG) \pm \frac{h_o^3 k^2}{6\eta}\sqrt{dG^2-dG^2} = -\frac{h_o^3 k^2}{6\eta}(dF+dG) \tag{2.24}$$

or

$$\sigma_{Th} = -\frac{h_o^3 k^2}{3\eta}(\gamma k^2 + \frac{A}{2\pi h_o^4} + \frac{3 \mid \gamma_T \mid T_h}{h_o}) \tag{2.25}$$

Where the subscript 'Th' signifies the solution for strong thermal effects. From Eq. 2.25, the characteristic wavelength λ_{Th} obtained from the maxima in the dispersion given by $d\sigma/dk = 0$ is given by:

$$\lambda_{Th} = \sqrt{-\frac{16\pi^3\gamma}{A+6\pi \mid \gamma_T \mid T_h h_o^3}} h_o^2 \tag{2.26}$$

By utilizing Eq. 2.28 with values of T_h obtained from the thermal model, the dashed and dotted curves in Fig. 2.3 have been evaluated.

Based on these dispersion relations, a qualitatively and quantitative analysis of the role of thermal gradients on dewetting for Ag and Co can be made. The most likely length scale(s) that will be observed experimentally following spontaneous dewetting is(are) the one(s) that grow at the fastest rate, and can be obtained from the equality $d\sigma/dk = 0$. Using, this, one can compare the classical spinodal length scale, i.e. dewetting without thermal

gradients (*Case 1*) to the characteristic wavelength resulting from strong thermal gradients (*Case 3*), which respectively give:

$$\lambda_C = \frac{2\pi}{k} = \sqrt{\frac{-16\pi^3\gamma}{A}} h_o^2 \tag{2.27}$$

$$\lambda_{Th} = \sqrt{-\frac{16\pi^3\gamma}{A + 6\pi \mid \gamma_T \mid T_h h_o^3}} h_o^2 \tag{2.28}$$

As expected, Eq. 2.27 is the classical form of dewetting without thermal gradients and a comparison of this length with that of Eq. 2.28 shows that intrinsic thermal gradients will modify the characteristic length scale. *Moreover, the length scale could decrease or increase, depending on the magnitude and sign of the gradient* T_h. From Fig. 2.2, it is clear that for liquid films whose starting thickness $h_o < h*$ the surface temperature gradient between two points on the perturbed surface will have $T_h > 0$. On the other hand for films where $h_o > h*$ the sign of the surface temperature gradient will be negative, i.e. $T_h < 0$. In this context, for the case when $T_h < 0$ (noting that $A < 0$ and $\gamma_T < 0$ is generally true for all materials and the metals evaluated here) the characteristic length scale should *decrease* in comparison to the classical value. On the other hand, for i.e. $T_h > 0$, the length scale should *increase* compared to its classical value.

2.5 Experiment vs. theory

1. Classical dewetting in Ag thin films: In Fig. 2.3(a), the experiment results for dewetting observed in Ag thin films (solid squares) is plotted along with the the best fit (solid line). For the best fit, the known value of surface tension $\gamma_{Ag} = 0.93$ Jm^{-2} has been used and this results in a value of 1.97 for the exponent of h_o and a Hamaker coefficient of $A = -4.78 \times 10^{-18}$ J, which is consistent with the magnitude expected for metals on SiO_2 [60]. The very good agreement between experiment measurement and the classical theoretical form

of Eq. 2.27 suggests that nanosecond laser dewetting of Ag on SiO_2 in the thickness regime investigated here follows the classical behavior. The observation of classical dewetting in Ag implies that the large intrinsic thermal gradients expected from Fig. 2.2(a) do not play a role in patterning. This result can be interpreted by refining the intrinsic heating effect to include thermal diffusion along the film surface. As noted earlier, the calculations of Fig. 2.2(b) assumed a local heating, i.e. one in which thermal energy was only transported perpendicular to the film and into the substrate, while thermal diffusion along the film was neglected. In reality, based on the time and length scales of relevance, heat diffusion along the film will not be negligible. In the laser heating experiment here, the relevant time scale is the time-to-melt, since it is at this point when the thermal gradient on the liquid surface will contribute to the patterning process. From experimental observations and thermal modeling [37], this time-to-melt is determined by the laser energy density and typically varies between 1 ns to ~t_p/2, where t_p is the Gaussian laser pulse width of 9 ns. Based on this the relevant thermal diffusion length $l_{Ag}^{th} \sim 2\sqrt{D_{Ag}^{th}\tau}$ lies between 734 to 1557 nm for a known thermal Ag diffusivity of $D_{Ag}^{th} \sim 13.48 \times 10^{-5}$ m^2/s [117]. Therefore, for surface perturbations whose wavelength $\lambda < l_{Ag}^{Th}$, negligible thermal gradient effects can be expected. From Fig. 2.3(a) it can be seen that the experimental dewetting length scales for Ag are $\leq$ 600 nm and so $\lambda < l_{Ag}^{Th}$ over the entire film thickness regime investigated here, i.e. $4 \leq h_o \leq 12$ nm. Thus, the large thermal conductivity of Ag suppresses the role of the intrinsic thermal gradients on the dewetting process in these experiments.

2. Dewetting in Co thin films: As compared to Ag, the behavior in Co is fundamentally different, as seen from Fig. 2.3(b). The thermal diffusivity of Co ($D_{Co}^{th} \sim 2.7 \times 10^{-5}$ m^2/s) is much smaller then Ag and so the thermal smoothing length scale l_{Co}^{Th} for times between 1 to 4.5 ns will be 328 to 697 nm respectively. Therefore, from Fig. 2.3(b),strong thermal gradient effects on dewetting for films having thickness from 2 to ~7 nm will be unlikely. Indeed, as seen by the best fit (solid line) of the experimental data ranging from 2 to 7 nm, the observed behavior follows the classical trend. For the best fit, a value of $\gamma_{Co} = 1.88$

Jm^{-2} was used and it results in a value of 1.98 for the exponent of h_o and a Hamaker coefficient value of $A = -1.4 \times 10^{-18}$ J, which is again consistent with the expected sign and magnitude of A. On the other hand, for films with $h_o > 7$ nm, the intrinsic thermal gradients should play some role on the dewetting length scale as $\lambda > l_{Co}^{Th}$. Indeed, as seen in Fig. 2.3(b), the experimental data deviate substantially from the classical trend for films with $h_o > 7$ nm. In fact the length scale decreases with increasing h_o in striking contrast to the classical behavior. In order to quantitatively evaluate the experimental results, the sign and magnitude of T_h for films in this thickness regime from curves, such as shown in Fig. 2.2(b), were estimated. The sign and magnitude of T_h for various values of the laser energy density ranging from 250 mJ/cm^2 to 400 mJ/cm^2 was calculated. For these energies, the various thicknesses reach their melting point in time scales ranging from 4.5 ns to $\sim$ 1 ns. From this calculation it was determined that the magnitude of the thermal gradient T_h ranged between $10^9 \leq T_h K \leq 5 \times 10^{10}$ K/m and the sign was negative, i.e. $T_h < 0$. Based on this and noting that $\mid 3\gamma_T T_h \mid > \mid A/2\pi h_o^3 \mid$ for this thickness regime (where |A| used for Co as $\sim 1.4 \times 10^{-18}$ J and $\gamma_T^{Co} = -0.3 \times 10^{-3}$ J/m^2-K [118]), Eq. 2.28 was used to estimate the characteristic length scales. From the functional form of the characteristic λ_{Th}, Eq. 2.28, it is clear that for $T_h < 0$ the length scale will decrease in comparison to the classical scale. The results of this calculation using T_h values for laser energies ranging from 250-400 mJ/cm^2 are plotted in Fig. 2.3(b) as dashed or dotted lines. It is evident that the experimentally observed behavior for the dewetting length scales for $h_o > 7$ nm can be reasonably well described by invoking the intrinsic thermal gradients resulting from the ns laser heating. *More importantly, this result suggests that the rich dewetting behavior that is observed experimentally following ns laser melting of thin metal films can also be explained by the principle of equating the rate of free energy change to the minimum rate of viscous energy loss in the system.*

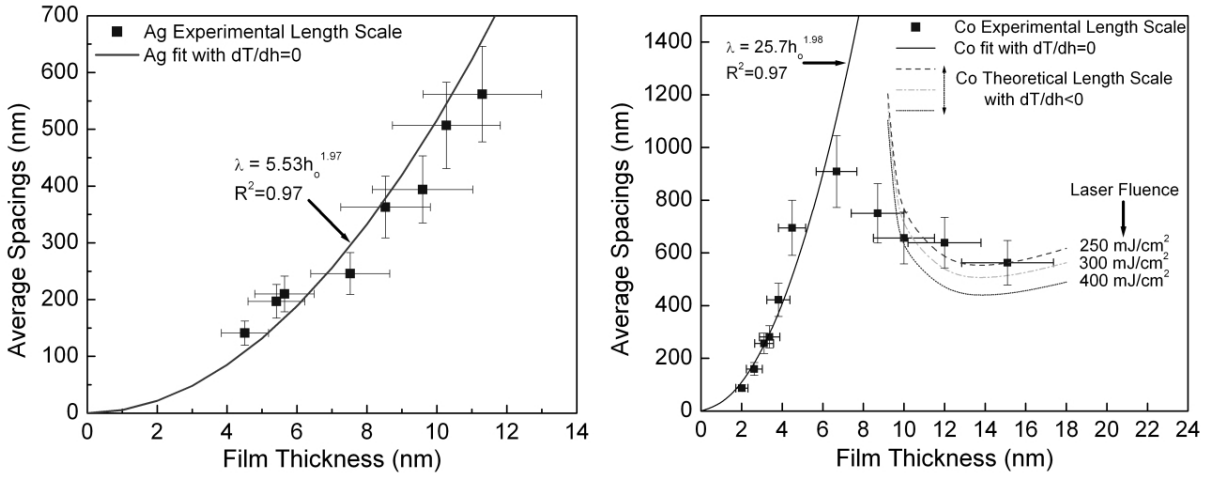

(a) (b)

Figure 2.3: (a) Experimental length scales (solid squares) and best fit without thermal gradients (solid line) for dewetting of Ag on SiO_2. The best fit results suggest that Ag dewetting follows the classical behavior. (b) Experimental length scales (solid squares), best fit without thermal gradients (solid line), and trends for dewetting with $T_h < 0$ (dashed/dotted lines) for dewetting of Co on SiO_2. Co dewetting for $2 \leq h_o \leq 7$ follows the classical behavior but it is strongly modified by intrinsic thermal gradients, leading to a substantial *decrease* in length scale over the classical values for $9 \leq h_o \leq 15$ nm. The theoretical trends from the energy transfer model estimated for various laser energy densities (dashed and dotted lines) captures the experimental observations reasonably well.

2.6 Conclusion

In summary, spontaneous dewetting patterns that arise when thin metal films are melted by a nanosecond pulsed laser with UV wavelength have been investigated. The dewetting patterns are characterized by complex nanomorphologies with well-defined length scales. Such thin films are expected to be in a thermodynamically unstable free energy state due the strong attractive dispersion forces. Pulsed laser heating is known to result in a strong thickness dependent film temperature. As a consequence, coupling of the incident laser light to height perturbations in the liquid phase of the film are likely to result in transient temperature gradients along the plane of the film. Based on this heating profile, a theoret-

ical evaluation of dewetting has been made using the principle that of a balance between the rate of free energy change to rate of viscous loss in the liquid thin film. The theory gives excellent agreement with the experimental observations for Ag films, in which pattern formation follows the classical behavior. Very good agreement for dewetting was also observed for Co films, in which strong thermal effects are visible and result in patterning length scales substantially different from the classical case. These results suggest that understanding and optimizing the rate of energy transfer in such nanoscale systems could be a useful approach for manipulating pattern formation during nanomaterials manufacturing via self-assembly or self-organization. Such complex metal nanomorphologies with predictable patterns and length scales can have applications in a variety of technologies, including in light-to-electricity converting materials, surfaces for Raman sensing via optical scattering and magnetism.

2.7 Acknowledgments

I would like to acknowledge Dr. C. Favazza for his contribution in the experimental length scale data of Co [shown in Fig. 2.3(a)], and Nozomi Shirato for his contribution in the heating model of Ag and Co [shown in Fig. 2.2(b)].

Chapter 3

Bilayer liquid self-organization: thermodynamic theory and experiments

Summary

In the previous chapter, a nanosecond pulsed laser-induced self-organization (SO) technique was applied to single layer metallic thin films on inert substrates to create spatially ordered nanopatterns. This SO technique is applied here to immiscible bilayer metallic thin films of Ag and Co on SiO_2 substrates. A theoretical analysis is performed for the SO in bilayer films, for both bilayer arrangements Ag/Co/SiO_2 and Co/Ag/SiO_2. The principle of balancing the rate of Gibbs free energy change to viscous dissipation was utilized to describe the length scales from spontaneous self-organization in ultrathin bilayer metallic films. For both configurations, theory predicts characteristic length scales, but with different functional behavior, as evidenced by the form of the film thickness dependence. This difference in behavior was attributed to the difference in the sign and magnitude of the intermolecular forces for the two configurations. The experimental length scale behavior for both the configurations are consistent with theory. Measurements of physical properties show that the nanoparticles are composites of Ag-Co, where the ratio of Ag and Co can be independently controlled. This result provides a practical way to independently vary the

length scale, composition, and size of the nanostructures. This bilayer self-organization is a cost-effective and robust nanomanufacturing process to make hybrid nanoscale materials with new properties. These studies can also assist in an understanding of dewetting in bilayer configurations of immiscible mixtures, which in turn could be used in the design and fabrication of nanoscale mixtures for a variety of applications.

3.1 Introduction

Self-organization is a powerful route to synthesize materials in a cost-effective and robust manner because the ensuing length scales and morphologies are primarily governed by forces intrinsic to the system. One of the simplest examples of self-organization leading to unique morphologies and nanostructures is the spontaneous spinodal dewetting of liquid films from an inert surface. In this process, the thermodynamic stability of the film is governed by a competition between stabilizing surface tension forces and destabilizing intermolecular forces, such as the attractive intermolecular dispersion force, with magnitude governed by the Hamaker coefficient A. The spontaneous patterning leading to well-defined length scales and morphologies results when natural fluctuations of the film surface produces an overall reduction in the free energy of the system. Since only specific fluctuation wavelength cause a reduction in free energy, the ensuing structures have characteristic scales. For instance, in single layer dewetting, the interparticle spacing λ is related to the film-ambient surface tension γ, the Hamaker coefficient A, and the average initial film thickness h_o as $\lambda = \sqrt{\frac{16\pi^3\gamma}{A}}h_o^2$. Recently, theoretical work on dewetting in bilayer liquid films has shown that it is possible to achieve superior control over patterning length scales [72, 69]. This is because the intrinsic forces governing the self-organization is dependent on the order of arrangement of the individual films, and as a result, improved control of the composition, size, and spacing of nanoparticles could be expected. However, this effect has not demonstrated experimentally.

A magneto-plasmonic (MP) nanoparticle is one which will have controllable ferromagnetic orientation and strong localized surface plasmon (LSP) response. The magnetic state and frequency-dependent resonant plasmonic response can exert control over photon and electron interactions, leading to changes in spin (polarization) as well as current (intensity). However, currently there is a dearth of such useful materials, especially those with low optical absorption and ability to manipulate electron and photon properties in multiple spatial dimensions. In practice, one way this can be achieved is by incorporating suit-

able magneto-plasmonic nanoparticles, within dielectrics, metals, or semiconductors. The resulting materials will show a multi-dimensional *and* coincidental control of the polarization state (or spin) and current (or intensity) of both photons, and electrons. As a result, new materials and properties related to the control of photon and electron behavior, including for magneto-optic sensing and data storage, for energy harvesting in photovoltaics with photon and spin-dependent electronic behavior, and in semiconductor computing and switching applications utilizing spintronic effects, will result. One suitable candidate for the MP nanoparticle is a mixture of a ferromagnetic metal like Co, with a strong optical plasmonic scatterer, like Ag. From the binary phase diagram [119] there is no atomic mixing between Co and Ag and therefore, combining Co with Ag can potentially show controllable ferromagnetic anisotropy as well as strong LSP interactions. However, the primary challenge lies in developing cost-effective nanomanufacturing routes to combine Co and Ag to achieve precise composition, size, and shape, all of which strongly influence ferromagnetic and optical behavior.

The motivation for the work presented here is to show that bilayer liquid self-organization can lead to control of concentration, size, and spacing of composite magneto-plasmonic nanoparticles, such as of Co and Ag, which are candidates for new materials and application. Recently, we have developed a thermodynamic model to explore the behavior of single film dewetting. In this model, the dispersion relation that characterizes the rate of deformation σ of the film to the perturbation wavevector k can be obtained by equating the rate of free energy change to the viscous dissipation, or the rate of frictional energy lost, during fluid flow. Consequently, the necessary quantitative description of dewetting can be readily obtained. Another benefit of using the thermodynamic approach is that it provides useful insight into the physical conditions of fluid flow. For instance, in the case of single layer dewetting under thermocapillary forces, the thermodynamic model shows that the ensuing self-organization is determined by conditions that minimize the rate at which viscous energy is lost during flow [1]. The thermodynamic model was applied to describe

self-organization in bilayer liquid systems. From this the σ vs k dispersion relation predicts substantially different behavior for the different bilayer configurations. In Fig. 3.1, the two possible deformation pathways, corresponding to squeezing and bending modes, are schematically depicted. Theory shows the Ag/Co/SiO_2 bilayer deforms by the bending mode while the Co/Ag/SiO_2 deforms by the squeezing mode. This is a result of the difference in interfacial and intermolecular forces for the two configuration. As a result, the length scales and their behavior with bilayer thickness also show dramatic differences. For the two bilayer configurations having identical thickness, vastly different length scales can result, leading to superior control of particle size and spacing.

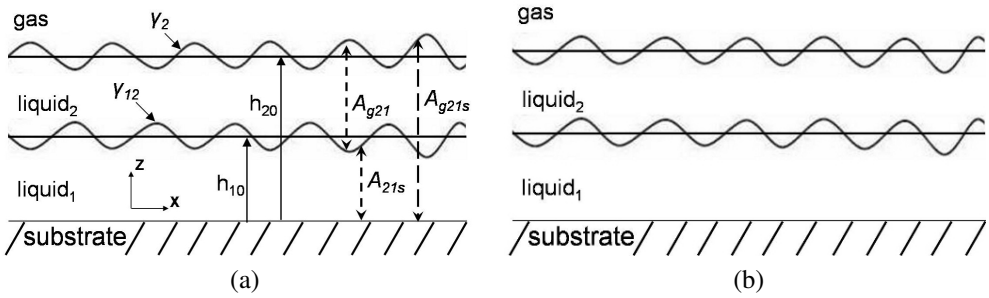

Figure 3.1: Schematic of the bilayer configuration showing the various quantities used in the theoretical model. (a) In Fig. a, the perturbation is a squeezing mode ($\alpha = \varepsilon_2/\varepsilon_1$ is < 0). (a) In Fig. b, the perturbation is a bending mode ($\alpha = \varepsilon_2/\varepsilon_1$ is > 0). The parameters indicated in fig a is same for fig b.

To provide an experimental demonstration of bilayer self-organization, the liquid films of immiscible Co and Ag were investigated. Since these metals have high melting points, the liquid phase has been accessed by melting by nanosecond pulses of a ultraviolet laser. It has been shown previously that spinodal dewetting of high melting point materials, such as metals, can be initiated and progressed under multiple cycles of melting by a pulsed laser [35, 4]. The pulsed laser dewetting of Ag and Co on silica (SiO_2) substrates was performed and the bilayer-thickness dependent behavior for the two possible configurations,

i.e. Ag/Co/SiO_2 and Co/Ag/SiO_2 was determined. A detailed experimental measurement of the ensuing nanoparticle spacing showed a substantial difference in the length scale behavior with bilayer configuration. This was consistent with predictions of the thermodynamic model. In addition, electron microscopy confirmed that the nanoparticles that result are composites made from individual grains of Ag and Co in the same ratio as the film thickness. As a result, the composition of the particles can be also be readily controlled.

3.2 Thermodynamic model for bilayer self-organization

In the thermodynamic model, the dispersion relation is obtained by equating the rate of Gibbs free energy change $\dot{\Delta F}$ to the total viscous dissipation $\dot{E}_V$ for the bilayer under small height perturbations to the liquid/vacuum surface and liquid/liquid interface. The rate of free energy change $\dot{\Delta F}$ is evaluated by comparing the free energy of this perturbed state to that of the initial unperturbed state [1]. In Fig. 3.1, the schematic of the bilayer structure, where the initially flat film thickness for bottom layer and the total bilayer is indicated as h_{10} and h_{20}, respectively. For the bilayer configuration the contributions to free energy changes come from the surface tension forces at the top liquid/vacuum and middle liquid/liquid interfaces, as well as due to the intermolecular interactions between the three pairs of interfaces, i.e. top-middle, middle-bottom, and top-bottom. The analysis was done by balancing the change in free energy between the flat unperturbed state to a perturbed state by considering surface height disturbances that are small compared to the heights of the individual films. The middle liquid/liquid interface and top free liquid surfaces are perturbed by Fourier components of type $h_1 = h_{10} + \varepsilon_1 e^{\sigma t - ikx}$, and $h_2 = h_{20} + \varepsilon_2 e^{\sigma t - ikx}$, where the perturbation amplitudes are ε_1 and ε_2, respectively. There are two possible collective modes for deformation [120, 72], where the decay rate and wavevector are identical for the two surfaces. In the squeezing mode, the perturbation amplitude ratio $\alpha = \varepsilon_2/\varepsilon_1$ is < 0 [shown in Fig. 3.1(a)], while in the bending mode, α is > 0 [Fig. 3.1(b)]. The Hamaker co-

efficients for the intermolecular dispersion interactions between different interfaces in the bilayer films are given by A_{21s}, A_{g21} and A_{g21s}, as indicated in Fig. 3.1, where the subscripts 1, 2, s and g denote liquid 1 (top layer), liquid 2, solid substrate, and gas, respectively.

With this information, the rate of free energy change from flat to the perturbed state of the films can be expressed as [1]:

$$\Delta\dot{F} = \frac{\partial}{\partial t}\{\sum[F(h_j) - F(h_{jo})]\} \tag{3.1}$$

$$\Delta\dot{F} = \frac{\partial}{\partial t}[\frac{1}{2}\gamma_{12}\left|\frac{\partial h_1}{\partial x}\right|^2 + \frac{1}{2}\gamma_2\left|\frac{\partial h_2}{\partial x}\right|^2 + \sum\frac{A_{efgh}}{2\pi h_{j0}^4}\triangle h_j^2] \tag{3.2}$$

where $\triangle h_j = \varepsilon_j e^{\sigma t - ikx}$ and A_{efgh} stands for the different Hamaker coefficients. The interfacial energies of the liquid 1 - liquid 2 and liquid 2- gas interfaces are γ_{12} and γ_2 respectively. For the bilayer system, upon substituting the different height functions, the above equation simplifies to:

$$\Delta F(\dot{k},\alpha) = \sigma\varepsilon_1^2\left[\gamma_2\alpha^2k^2 + \gamma_{12}k^2 + \frac{A_{g21s}\alpha^2}{2\pi h_{2_o}^4} + \frac{A_{21s}}{2\pi h_{1_o}^4} + \frac{A_{12g}(\alpha-1)^2}{2\pi(h_{2_o}-h_{1_o})^4}\right]e^{2\sigma t - 2ikx} \tag{3.3}$$

$$\Delta F(\dot{k},\alpha) = \sigma\varepsilon_1^2 dF e^{2\sigma t - 2ikx} \tag{3.4}$$

The total viscous dissipation $\dot{E}_V$ per unit area of the bilayer system can be evaluated from the knowledge of the fluid velocities and viscous stresses within each of the two fluid layers [68]. The calculation (See Supplementary material) was performed by using fluid flow analysis within the lubrication approximation [121] for a 1-D isothermal situation. In this approximation, with boundary conditions, and the resulting expression for velocities taken from Bandyopadhyay et al [72]. The boundary conditions for the bilayer situation are as follows. The top surface of liquid 1 and gas (at $z = h_2$ in Fig. 3.1) is considered stress free, the bottom interface between liquid 2 and substrate (at $z = 0$) is a no-slip interface,

while for the middle interface between liquid 1 and liquid 2 (at $z = h_1$), the stress and velocity are continuous across the interface. The velocity along the x-direction of the layer is u_j, $\bigtriangledown p_j$ is the pressure gradient in the x-direction, and η_j is the viscosity, where $j = 1,2$ indicates liquid 1 and liquid 2. The total viscous dissipation for the bilayer can be written as [68]:

$$\dot{E_V} = \eta_1 \int_0^{h_{10}} (\frac{du_1}{dz})^2 dz + \eta_2 \int_{h_{10}}^{h_{20}} (\frac{du_2}{dz})^2 dz \tag{3.5}$$

Using the lubrication approximation and above mentioned boundary conditions, the velocities (Eq. 3.6 and 3.7) and viscous stresses (Eq. 3.8 and 3.9) can be expressed as follows:

$$\eta_1 u_1 = \nabla P_1 (z^2/2) + (\nabla P_2 - \nabla P_1) h_{10} z - \nabla P_2 h_{20} z \tag{3.6}$$

$$\eta_2 u_2 = \nabla P_2 (\frac{z^2 - h_{10}^2}{2}) - \nabla P_2 h_{20} (z - h_{10}) + \eta_2 (u_1)_{h_{10}} \tag{3.7}$$

$$\eta_1 \frac{du_1}{dz} = \nabla P_1 (z - h_{10}) + \nabla P_2 (h_{10} - h_{20}) \tag{3.8}$$

$$\eta_2 \frac{du_2}{dz} = \nabla P_2 (z - h_{20}) \tag{3.9}$$

In order to estimate the dissipation, an expression for the pressure gradient is needed. This is obtained from the simultaneous equations describing volume conservation of the fluid within each layer:

$$\frac{\partial h_1}{\partial t} = \frac{h_{10}^3}{3\eta_1} \nabla^2 P_1 - \frac{h_{10}^2 (h_{10} - h_{20})}{2\eta_1} \nabla^2 P_2 \tag{3.10}$$

$$\frac{\partial h_2}{\partial t} = -\frac{(h_{10}^3/3 - h_{10}^2 h_{20})}{2\eta_1} \nabla^2 P_1 - \nabla^2 P_2 (\frac{(h_{10} - h_{20})^3}{3\eta_2} + \nabla^2 P_2 \frac{(h_{10} - h_{20}) h_{10}}{\eta_1} (h_{20} - \frac{h_{10}}{2}) \tag{3.11}$$

By using Cramer's rule, the $\nabla^2 P$'s can be expressed as:$\nabla^2 P_1 = \frac{D^1}{D}$; $\nabla^2 P_2 = \frac{D^2}{D}$, where

D, D^1 and D^2 correspond to the 2x2 matrix of the simultaneous equation (Eq. 3.10 and 3.11) given by,

$$\begin{bmatrix} \nabla^2 P_1 \\ \nabla^2 P_2 \end{bmatrix} \begin{bmatrix} \frac{h_{10}^3}{3\eta_1} & -\frac{h_{10}^2(h_{10}-h_{20})}{2\eta_1} \\ -\frac{h_{10}^2(\frac{h_{10}}{3}-h_{20})}{2\eta_1} & (-\frac{(h_{10}-h_{20})^3}{3\eta_2} + \frac{(h_{10}-h_{20})h_{10}(h_{20}-\frac{h_{10}}{2})}{\eta_1}) \end{bmatrix} = \begin{bmatrix} \frac{\partial h_1}{\partial t} \\ \frac{\partial h_2}{\partial t} \end{bmatrix} \tag{3.12}$$

By using the height perturbations of each of the two films in terms of single Fourier mode, ∇P_j can be evaluated by integrating over the x-direction to get an indefinite integral as $\nabla P_i = \int \nabla^2 P_i dx$, which gives:

$$\nabla P_1 = \frac{i\sigma}{k}\varepsilon_1 \frac{(D_{22} - \alpha D_{12})}{(D_{11}D_{22} - D_{12}D_{21})} e^{\sigma t - ikx} = \frac{i\sigma}{k}\varepsilon_1 p_1 e^{\sigma t - ikx} \tag{3.13}$$

$$\nabla P_2 = \frac{i\sigma}{k}\varepsilon_1 \frac{(-D_{21} + \alpha D_{11})}{(D_{11}D_{22} - D_{12}D_{21})} e^{\sigma t - ikx} = \frac{i\sigma}{k}\varepsilon_1 p_2 e^{\sigma t - ikx} \tag{3.14}$$

Finally, the viscous dissipation can be evaluated from the form :

$$\dot{E_V} = f(p_1, p_2)$$

Using Eq. 3.8 and 3.9 in Eq. 3.5, the total dissipation can be evaluated as:

$$\dot{E_V} = \frac{h_1^3}{3\eta_1}(\nabla P_1)^2 + \frac{(h_2 - h_1)^2 (h_2 + 2h_1)}{3\eta_2}(\nabla P_2)^2 + \frac{h_1^2 (h_2 - h_1)}{\eta_1}(\nabla P_1)(\nabla P_2) \tag{3.15}$$

Now using Eqs. 3.13 and 3.14, the above equation can be rewritten as:

$$E_V(\dot{k}, \alpha) = -H\left(\frac{\sigma^2 p_1^2}{k^2}\right) e^{2\sigma t - 2ikx} \tag{3.16}$$

where,

$$\dot{H} = \left[\frac{h_1^3}{3\eta_1} + \frac{(h_2 - h_1)^2 (h_2 + 2h_1)}{3\eta_2} \left(\frac{p_2}{p_1} \right)^2 + \frac{h_1^2 (h_2 - h_1)}{\eta_1} \left(\frac{p_2}{p_1} \right) \right] \tag{3.17}$$

From the above derived equations, one can directly obtain the dispersion relation that relates the rate of deformation σ with the wavevector k by equating the rate of free energy change (eq. 3.3) to the viscous dissipation (Eq. 3.16). The resulting expression is of form:

$$\sigma(k, \alpha) = -\frac{k^2 dF}{H p_1^2} \tag{3.18}$$

From the form of Eq. 3.18, it can be noted that the deformation rate σ is a function of two variables, k and α for any given value of h_{10} and h_{20}. Therefore, in order to obtain the most probable length scale λ, the maximum deformation rate must be obtained from a surface plot of σ vs k and α, or mathematically the maximum of equation $\partial\sigma/\partial k + \partial\sigma/\partial\alpha = 0$. In Fig. 3.2(a), a typical 3-D dispersion plot is shown for the bilayer case of Ag(5 nm)/Co(5 nm)/SiO_2, while in Fig. 3.2(b) it is shown for the Co(5 nm)/Ag(5 nm)/SiO_2 case. It is evident that for a specific combination of k and α, the deformation rate attains a maximum. A conventional representation of this 3-D dispersion plot is a slice taken at a particular value of α. In Fig. 3.2(c), a slice or 2-dimensional dispersion plot at particular α is shown for Ag(5 nm)/Co(5 nm)/SiO_2. Again, it is clear that the deformation rate achieves a maxima at specific values of k, and these in turn vary with α. From such 3-D dispersion plots, the characteristic rate $\sigma*$, wavevector k^* and the corresponding α value could be evaluated for any combination of bilayer thickness and bilayer configuration. In Table 3.1, the materials parameters used to evaluate the theoretical behavior is presented. Important to note here that the Hamaker coefficient (A_{efgh}) values can be obtained by two approaches. In one case, the A values can be calculated using the dielectric function of the different materials involved, as shown in ref. [122], while in ref. [72], they are evaluated using the various interfacial energies. Both the values are provided in Table 3.1, with the calculations

presented in Fig. 3.2 estimated from the dielectric function.

Table 3.1: Table of materials parameters, including the Hamaker coefficients calculated using two different approaches and surface tensions and viscosities for the two bilayer configurations investigated.

Hamaker coefficients (J)	$Ag/Co/SiO_2$		$Co/Ag/SiO_2$	
Using different approaches	Using ref. [122]	Using ref. [72]	Using ref. [122]	Using ref. [72]
A_{g21s}	-2.25×10^{-19}	-2.15×10^{-18}	-2.10×10^{-19}	-2.03×10^{-18}
A_{21s}	-3.09×10^{-19}	-9.19×10^{-19}	1.97×10^{-19}	6.07×10^{-19}
A_{g21}	1.61×10^{-19}	7.31×10^{-19}	-2.26×10^{-19}	-1.04×10^{-18}
Viscosity (η)	$\eta_{Co}^{T_m} = 4.46x10^{-3}Pa-s$		$\eta_{Ag}^{T_m} = 3.88x10^{-3}Pa-s$	
$\gamma_{Co} = 1.88J/m^2$	$\gamma_{Ag} = 0.925J/m^2$		$\gamma_{Co/Ag} = \gamma_{Ag/Co} = 0.168J/m^2$	

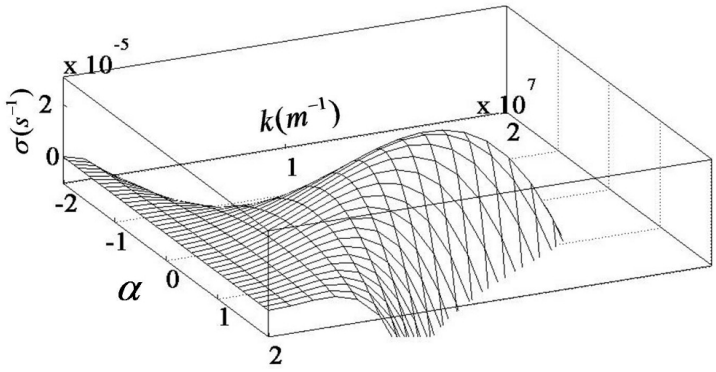

(a)

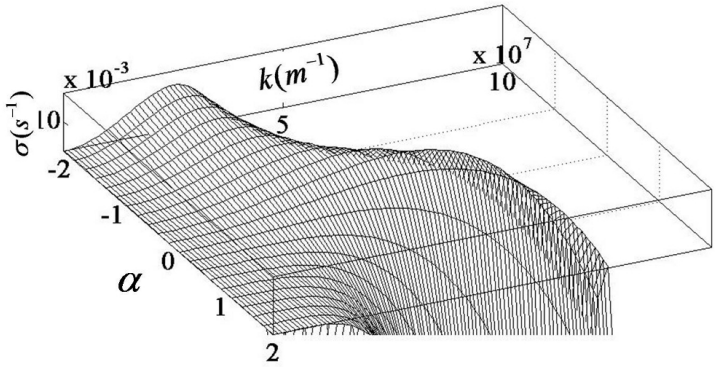

(b)

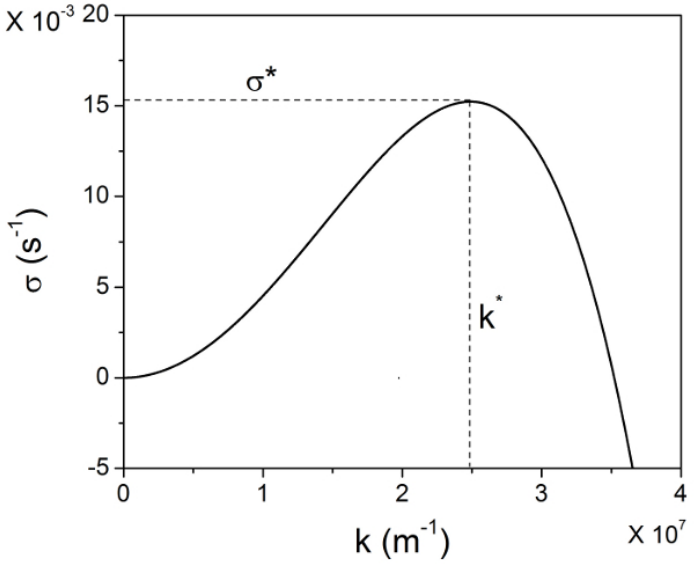

(c)

Figure 3.2: Surface plots of the dispersion behavior showing variation in the decay rate σ as a function of wave vector k and perturbation amplitude ratio α for Ag/Co/SiO_2 [Fig. (a)] and Co/Ag/SiO_2 [Fig. (b)]. (c) Typical 2-dimensional (2-D) dispersion plot at a particular α, used to obtain σ^* and $k^*$for Ag/Co/SiO_2. All these three plots are for 5 nm thick films of both Ag and Co in both bilayer arrangements.

In Table 3.2, the α values corresponding to maximum σ for different combinations of film thicknesses for both configurations is shown. In both cases, the bottom liquid layer thickness was fixed at 5 nm while the top layer was varied between 1 to 17 nm. Importantly, the α values leading to the maximum deformation rate for the Ag/Co/SiO_2 configuration corresponded to the bending mode ($\alpha > 0$) for all thicknesses, while for Co/Ag/SiO_2 it corresponded to the squeezing mode ($\alpha < 0$). In Fig. 3.3, the overall length scale, $\lambda = 2\pi/k^*$ is shown, behavior for the two bilayer combinations as a function of top layer thickness ranging from $1 \leq (h_{20} - h_{10}) \leq 17$ nm, and for values of the bottom layer ranging from $5 \leq h_{10} \leq 10$ nm. Fig. 3.3 is the behavior for Ag/Co/SiO_2 system, and shows that the length scale transitions from an initial increase to a rapid decreases, and eventual saturation with increasing top layer thickness. On the other hand, Fig. 3.3(b) shows that in the Co/Ag/SiO_2 system, the length scale increases monotonically with increasing top layer thickness. The most important theoretical result can be summarized as follows. *For identical thickness of each film in the bilayer, the two configurations give different patterning length scales. This suggests that the nanoparticles created from same thickness of Ag and Co can have different interparticle spacing and diameter simply by changing the configuration of the bilayer*. In order to verify this behavior, detailed experiments were performed, as discussed next.

Table 3.2: The ratio of perturbation amplitude α ($= \varepsilon_2/\varepsilon_1$) values for Ag/Co and Co/Ag on SiO_2 substrates for different bottom layers (5 nm, 7 nm and 10 nm). Positive and negative α indicate the bending and squeezing modes, respectively.

Ag/Co/SiO_2				Co/Ag/SiO_2	
h_{Ag} (nm)	α for h_{Co}=5nm	α for h_{Co}=7nm	α for h_{Co}=10nm	h_{Co} (nm)	α for (h_{Ag}=5, 7 and 10nm)
1	1	1	1	1	-2
2	0.99	1	1	2	-2
3	0.95	0.99	0.99	3	-2
4	0.85	0.99	0.95	4	-2
5	0.56	0.95	0.88	5	-2
6	0.25	0.80	0.85	6	-2
8	0.06	0.50	0.80	8	-2
10	0.04	0.1	0.2	10	-2
12	0.01	0.1	0.2	12	-2
15	0.01	0.08	0.1	15	-2
17	0.005	0.05	0.1	17	-2

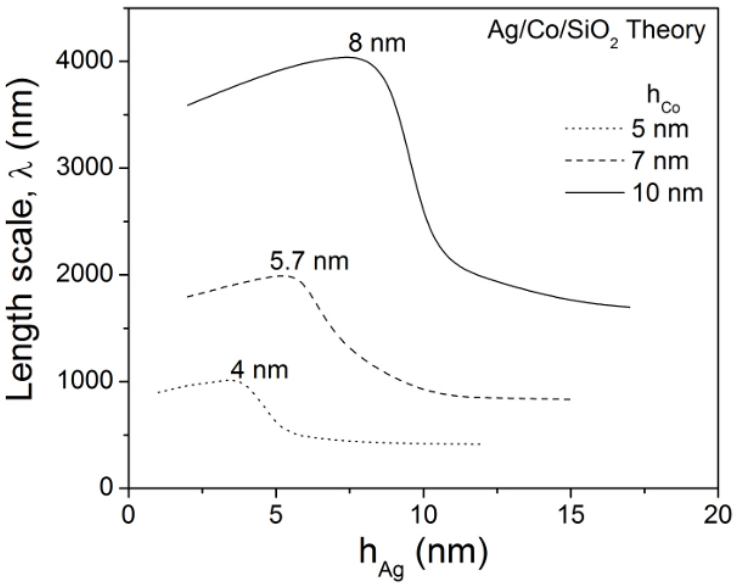

(a)

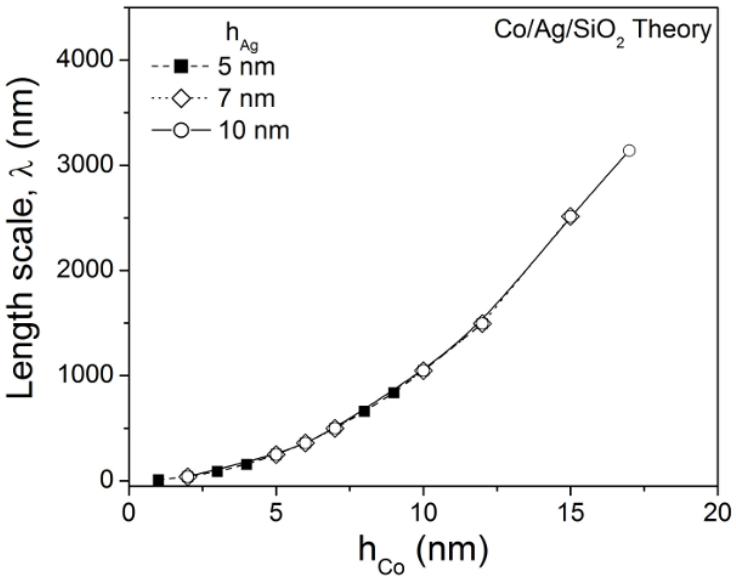

(b)

Figure 3.3: Theoretical length scale plots for different bottom layer thickness (5 nm, 7 nm and 10 nm) for (a) $Ag/Co/SiO_2$, and (b) $Co/Ag/SiO_2$ configuration. The top layer thickness was varied from 1 nm to 17 nm.

3.3 Experimental measurements of bilayer self-organization

Ultrathin films of Co and Ag were first deposited under high vacuum conditions ($\sim 1 \times 10^{-8}$ Torr) using electron beam evaporation (e-beam) and pulsed laser deposition (PLD) techniques on commercially available optically smooth SiO_2/Si(100) substrates. The thickness of thermally grown SiO_2 layer was 400 nm. Prior to film evaporation, the substrates were cleaned by ultrasonic rinsing in acetone, ethanol and DI water. Two types of bilayer structures were deposited. For the Ag/Co/SiO_2 structure, the bottom Co film of a fixed thickness of 5 nm was first deposited by e-beam and was followed by the deposition of a top Ag layer by PLD. Several such samples were prepared with the top Ag layer film varying from 1 to 12 nm. For the Co/Ag/SiO_2 configuration, a bottom Ag layer of 5 nm thickness was deposited by e-beam evaporation followed by deposition of Co by PLD. Several such samples were prepared with the top Co layer film varying from $\sim$1 to 12 nm. The thicknesses of the e-beam films were estimated by measurement of the deposition rate monitored by quartz crystal thickness monitor. For the case of the films deposited by PLD, the thickness was measured by performing quantitative energy dispersive x-ray spectroscopy (EDS) measurements and comparing the metal x-ray counts with calibrated measurements on metal films of known thicknesses [123]. Following deposition, the samples were irradiated (without breaking vacuum) at normal incidence with a pulsed laser beam, with a Gaussian spatial profile whose intensity variation was less that 10% over the regions of investigation (typically 1 mm). The Nd:YAG laser output consisted of 266 nm wavelength light, 9 ns pulse width, with a repetition rate of 50 Hz. The laser energy density of 80 mJ/cm^2 was chosen such that all the bilayer combinations could be completely melted. This melting was confirmed by the experimental observation that a substantial surface deformation occurs at a threshold energy, and this corresponds to the melt threshold, as shown previously for single layer films [123]. This energy threshold was also confirmed by the modeling of melting process by heating the bilayer under laser pulse [123]. The final spontaneous self-organized state of nanoparticles was achieved by irradiating the samples

with $\sim$10,000 laser pulses. The ensuing nanoparticles were then characterized using a scanning electron microscopy (SEM, Hitachi S-4300). The root means square roughness of the as-deposited films were measured to be in the range of 0.5 nm (RMS) using atomic force microscopy (AFM, Digital Instruments Dimension 3000 Multimode III A scanning probe microscope). The crystalline structure and composition characteristics of the nanoparticles was measured by transmission electron microscopy (TEM, JEOL JEM - 2100F field emission) and X-ray mapping in SEM (JEOL JSM - 7001 FLV field emission) investigations of select samples.

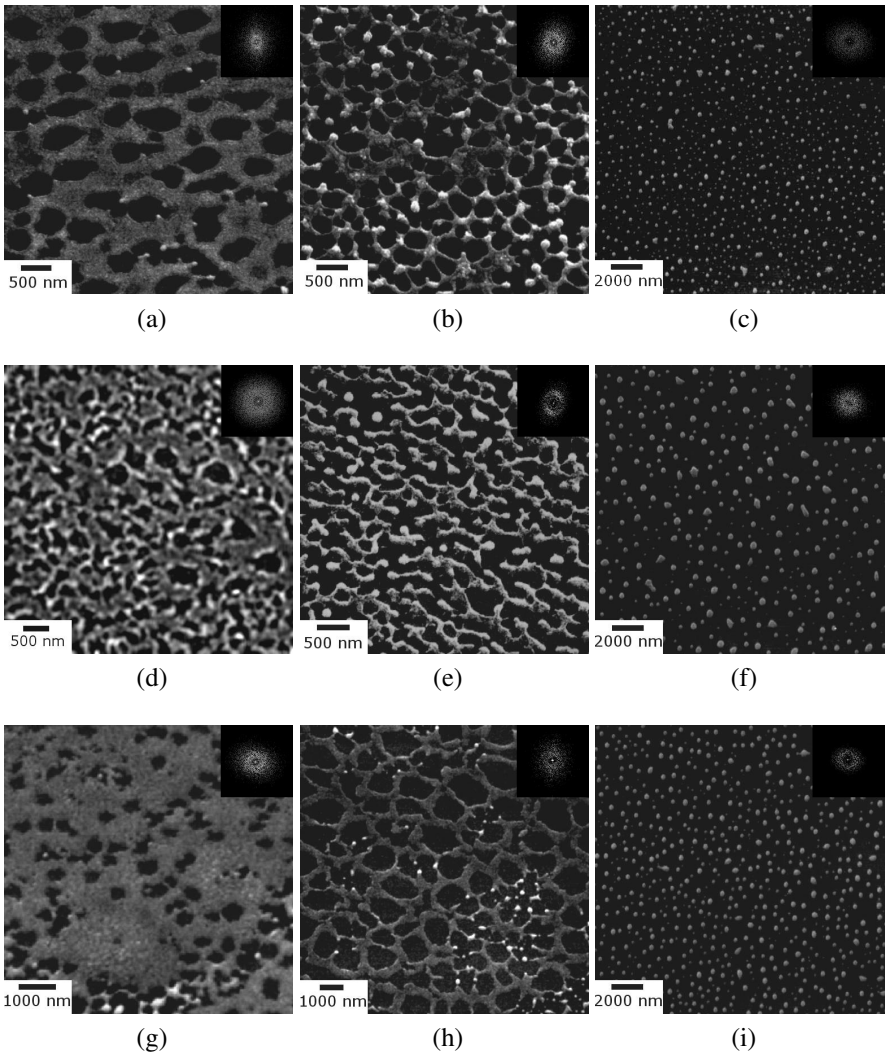

Figure 3.4: SEM images for the morphological evolution in bilayer Ag/Co/SiO_2; (a-c) images after irradiation on the bilayer film thicknesses of 1 nm of Ag and 5 nm Co, (d-f) initial film thicknesses were 3.5 nm of Ag and 5 nm Co, (g-i) for 12 nm of Ag and 5 nm Co. The images (a), (d) and (g) are after irradiation with 10 laser pulses; (b), (e) and (h) are after $\sim$100 laser pulses; and figures (c), (f) and (i) are after $\sim$10000 laser pulses. The inset of each image shows the FFT of the corresponding SEM image. The annular shape in each FFT is the indication of presence of SRO.

To measure the self-organization length scale, the nearest neighbor interparticle spacing was evaluated, which has been shown to be related to the spinodal dewetting length scale in single layer systems [35, 123]. SEM micrographs as indicated in images (c), (f) and (i) in Figs. 3.4 and 3.6 of the nanoparticles resulting from the self-organization for a series of Ag/Co/SiO_2 and Co/Ag/SiO_2 samples were used. In which, the bottom layer thickness was

fixed at 5 nm, and the top layer was varied from 1 - 12 nm. Also shown in the inset of each of these figures is the Fast Fourier Transform (FFT) of the image contrast. The ring-like spectrum is characteristic of short range order in the interparticle spacing, confirming that there is indeed a characteristic length scale for the pattern formation. From these images, the experimentally observed length scale was evaluated for the two bilayer configurations. In Fig. 3.5(a) theory (solid and dashed lines) and experiment (symbols) for the Ag/Co/SiO_2 system is compared, while Fig. 3.5(b) shows the results for the Co/Ag/SiO_2 system. In both cases, the bottom layer thickness was fixed at 5 nm, while the top layer thickness was varied. The two sets of theoretical lines in each figure were obtained by using the two sets of Hamaker coefficients, shown in Table 3.1. These Hamaker coefficient values were calculated using two different approaches. The first approach [69] includes the interaction between two surfaces through vacuum with a difference in their dielectric constants. In the second approach [72], the Hamaker coefficients were estimated using the difference in interfacial energies of the interacting surfaces. As seen from the two figures, very good agreement between theory and experiment is evident. The dramatic change in length scale behavior for the Ag/Co/SiO_2 system predicted by theory is clearly seen in the experiments.

The difference in self-organizing behavior for the two bilayer combinations can be explained on the basis of the difference in intermolecular forces. As shown in Fig. 3.1, the signs (negative sign is attractive interaction, see Table 3.1) and magnitudes of the intermolecular dispersion forces are different for the two configurations. In the case of Co/Ag/SiO_2 the top Co layer is always destabilizing because of the negative Hamaker coefficient (A_{g21}) while the bottom Ag layer is always stabilizing. As a result, the spontaneous patterning is dictated primarily by the top layer and so the length scale increases monotonically with top Co layer thickness. This explains the repeatable length scale behavior obtained in theory for different bottom layer (Ag) thickness (h_{Ag} = 5, 7 and 10 nm) [see Fig. 3.3(b)]. For the case of Ag/Co/SiO_2, the bottom Co layer is always unstable while the top Ag layer is always stabilizing. In this case, when the top layer (Ag) is thin compared to the

bottom layer (Co), the additive effect of attractive intermolecular dispersion force between the top interface and the substrate (A_{g21s}) *and* the middle interface (liquid$_1$ - liquid$_2$) and substrate (A_{21s}) contributes to the instability. The length scale increases with increase in top layer (Ag) thickness until such time that this interaction is sufficiently weak so that the instability is then determined primarily by the bottom Co layer. In the case of Ag/Co, this transition occurs when the top layer thickness reaches close to the bottom layer thickness. In the theoretical analysis the transition occurs at $\sim$4 nm, 5.7 nm and 8 nm, respectively for the bottom layer (Co) thicknesses of 5 nm, 7 nm and 10 nm [Fig. 3.3(a)] and experimentally $\sim$3.9 nm for 5 nm bottom thickness. Following the transition point, the patterning length scale relaxes to a value determined primarily by the fixed thickness of the bottom layer.

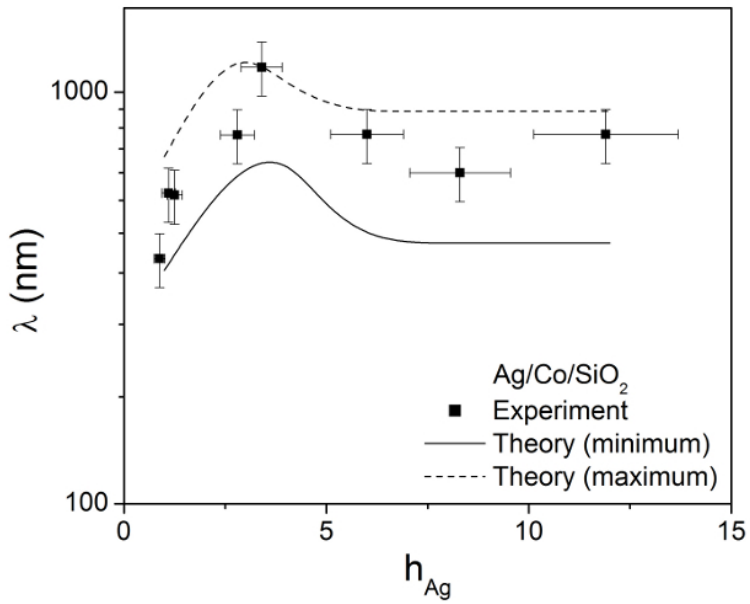

(a)

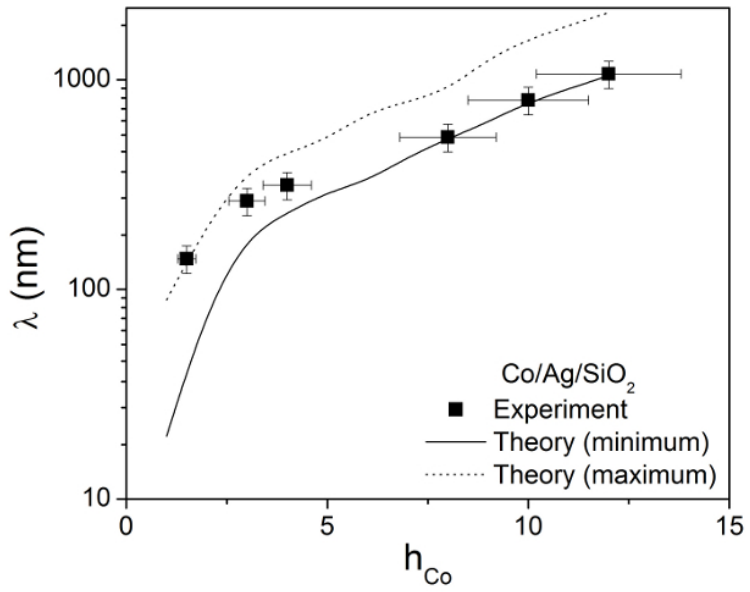

(b)

Figure 3.5: Comparison of theoretical behavior (solid and dashed lines) to the experimentally determined length scales (closed and open symbols) for the two bilayer configurations; (a) Ag/Co/SiO_2, and (b) Co/Ag/SiO_2. In both the cases the bottom layer thickness was kept constant at 5 nm and the top layer thickness was varied. The theoretical length scales indicated by solid and dashed lines in both figures are plotted using the maximum and minimum range of Hamaker coefficients values for different interfaces in the bilayers.

3.4 Morphological analysis

Figures 3.4(a-i) shows a series of SEM micrographs of the evolution of dewetting morphologies in bilayer Ag/Co/SiO_2 for different film thickness combinations of Ag and Co in the bilayer. Figures 3.4(a-c) are the SEM images for the progression of morphology in bilayer Ag/Co/SiO_2 with 5 nm thick Co and 1 nm Ag. The early stage dewetting morphology, following irradiation by 10 laser pulses is shown in Fig. 3.4(a). The morphologies following $\sim$100 and 10000 laser pulses are presented in Fig. 3.4(b) and (c), respectively. The spatial characteristics of each morphology was obtained by evaluating the fast Fourier transform (FFT) of the SEM image. The FFT information of the contrast correlation is shown in the inset of each figure. The annular form for each of the FFT is the indication of presence of short range order (SRO) in each stage of dewetting. Similarly, the morphologies following $\sim$10, 100 and 10000 laser pulse irradiation are presented in Figures 3.4 (d-f) and (g-i), for the thickness combinations of 5 nm Co, 3.5 nm Ag and 5 nm Co, 12 nm Ag, respectively.

Similar to bilayer Ag/Co/SiO_2, the progression of dewetting morphology was also studied for bilayer configuration Co/Ag/SiO_2, as shown in Figures 3.6(a-i). Here the SEM images in Figures 3.6(a-c) was obtained after irradiation on bilayer film of 5 nm thick Ag and 1.5 nm Co, following irradiation of $\sim$10 (fig. a), 100 (fig. b) and 10000 (fig. c) laser pulses, respectively. Morphologies shown in Figures 3.6(d-f) and (g-i) were obtained using thicknesses 5 nm Ag, 4.5 nm Co and 5 nm Ag, 12 nm Co, respectively.

In either bilayer arrangements, Ag/Co/SiO_2or Co/Ag/SiO_2, the morphological pathway depends on the ratio of Co and Ag thicknesses in the bilayer, as can be seen in the series of SEM images in Figures 3.4 and 3.6. The initial and intermediate stage morphologies (*i.e.* after $\sim$10 and 100 laser pulses) in each thickness combinations are dictated by the thicker layer of the two films in the bilayer. For instance, when Co film is thicker than Ag, then the initial and intermediate stages follow by forming the holes and polygon networks, which are the morphological stages in the case of a single layer of Co on SiO_2 [35, 123]. However,

when Ag film is thicker than Co in the bilayer, then the morphology pathway is through the formation of bicontinuous structures (see Fig. 3.6(a) and (b)), until Ag film is $\sim$10 nm thick. For the thicker Ag films ($\geq$ 10 nm) in the bilayer, the morphology is dictated by holes and polygons, as can be seen in Fig. 3.4(g) and (h). The formation of bicontinuous and polygons was evident in the case of single layer of Ag on SiO_2. Interestingly, when both Ag and Co films are similar in thickness in either arrangements, the morphology was evidenced by a combination of bicontinuous and polygons, as can be seen in images (d) and (e) of Figures 3.4 and 3.6. In either case of the bilayer configuration, the final morphology after $\sim$10000 laser pulses is an array of nanoparticles.

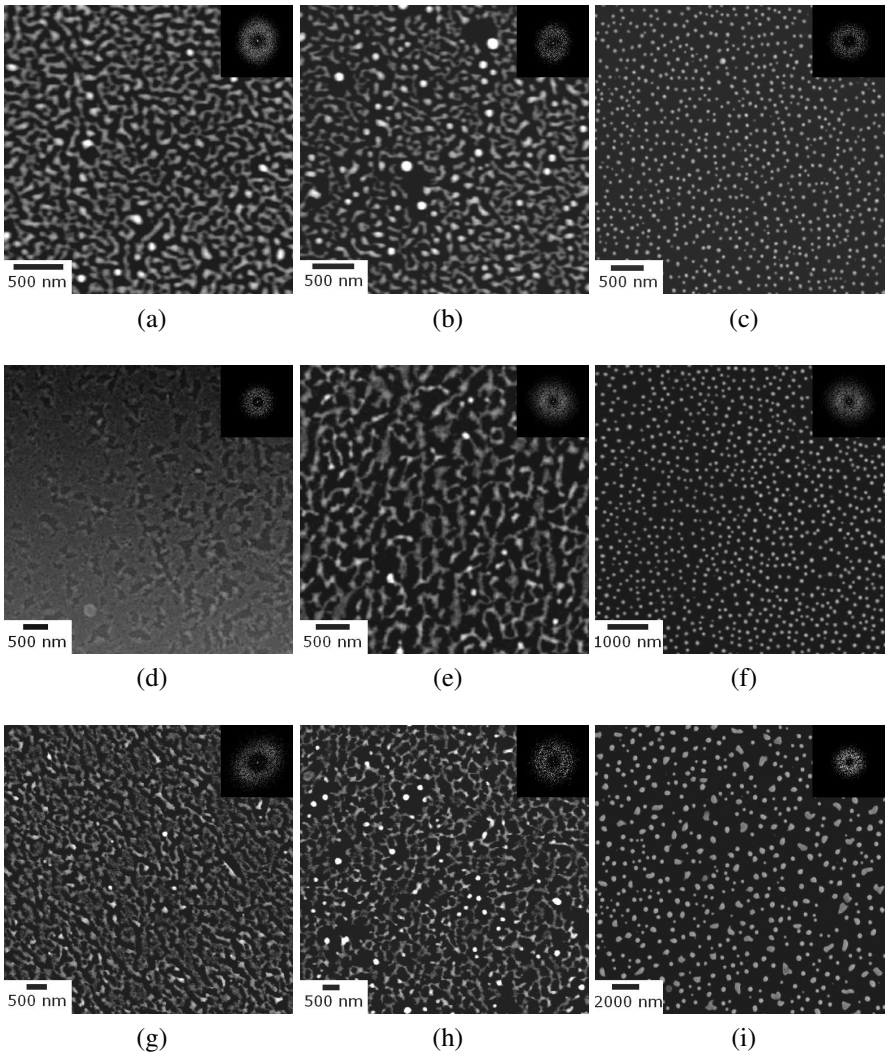

Figure 3.6: SEM images for the morphological evolution in bilayer Co/Ag/SiO_2; (a-c) images after irradiation on the bilayer film thicknesses of 1.5 nm of Co and 5 nm Ag, (d-f) initial film thicknesses were 4.5 nm of Co and 5 nm Ag, (g-i) for 12 nm of Co and 5 nm Ag. The images (a), (d) and (g) are after irradiation with 10 laser pulses; (b), (e) and (h) are after $\sim$100 laser pulses; and figures (c), (f) and (i) are after $\sim$10000 laser pulses. The inset of each image shows the FFT of the corresponding SEM image. The annular shape in each FFT is the indication of presence of SRO.

As discussed above that the morphology obtained after laser-induced self-organization in bilayer metallic films is always dictated by the thicker film in the bilayer, which is in contrast to the results obtained for the case on bilayer polymer films [69]. More detailed study

is required to address this difference in morphological behavior in metals and polymers.

3.5 Microstructural analysis

Figure 3.7(a) shows the plan view bright field TEM micrograph for nanoparticles created after laser irradiation on Ag/Co/SiO_2. The inset of Fig. 3.7(a) is TEM image of a particle with diameter $\sim$100 nm. Each particle consist of small grains, and different grains inside each particle show different contrast, a possible indication that the grains consist of different chemical composition (or rather different atomic number or Z values). Similar results were also obtained in the case of bilayer configuration Ag/Co/SiO_2. Figure 3.7(b) shows the selected area diffraction (SAD) pattern taken on a single nanoparticle of $\sim$50 nm in diameter. The *d* spacings and the corresponding crystallographic planes [124, 125] for the diffraction rings indicated with numbers in SAD pattern (see Fig. 3.7(b)) is shown in Table 3.3. The diffraction spots for each *d* spacings is distributed in several directions, indicating the random orientation of the grains. The experimentally observed *d* spacings matched well with the elemental theoretical *d* spacings of cubic phase of pure Co and face centered cubic phase of pure Ag.

In order to verify the fraction of Ag and Co in each nanoparticle, x-ray mapping analysis in the SEM was performed. These measurements were performed on the array of nanoparticles, as shown in Fig. 3.8. Figures 3.8(a), (d) and (g) are the SEM micrographs of the array of nanoparticles obtained for the thickness combinations Co (1.5 nm)/Ag (5 nm), Co (4.5 nm)/Ag (5 nm), and Ag (1 nm)/Co (5 nm), respectively. Figures 3.8(b), (e) and (h) show the spatial map of Ag in the arrays, while Figures 3.8(c), (f) and (i) show the same for Co. The presence of both Ag and Co in each particle confirms that each particle consists of both Ag and Co, supporting the result obtained by TEM analysis. From the number of counts within each particle, the ratio of Co and Ag was established as a function of their initial film thickness. Figure 3.9 shows a plot of ratio of x-ray counts of Ag and Co

in the array to the ratio of initial film thickness of Ag and Co in the bilayer. This indicates that the ratio of the x-ray count for each particle is similar to the ratio of the film thickness (i.e. $\sim$1). This confirmed that the composition of each particle is determined by the ratio of the film thickness. These TEM and SEM results were confirmed for a number of other bilayer compositions as well as arrangements. While this behavior is expected, given the immiscibility of Ag and Co, this is the first evidence that composite nanoparticles can be synthesized with good control of size, spacing and composition.

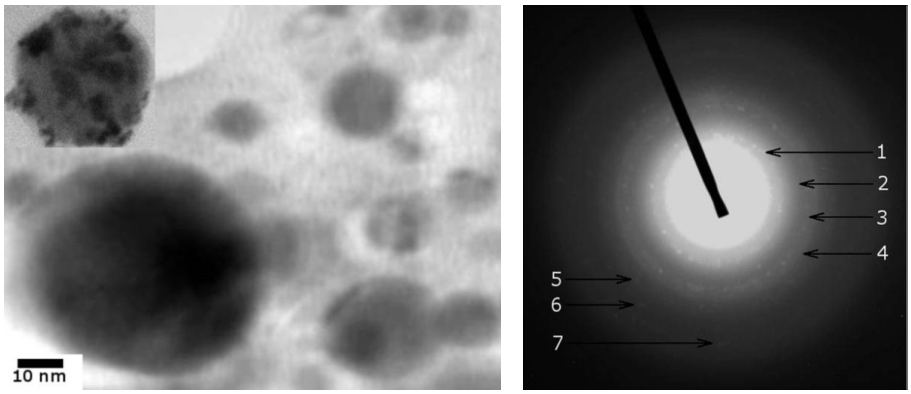

(a) (b)

Figure 3.7: TEM analysis of nanoparticles obtained from dewetting of Co/Ag/SiO_2; (a) Plan-view TEM micrograph of Co/Ag/SiO_2 nanoparticles showing contrast inside each particle indicating presence of grains. The inset shows the TEM micrograph of a larger particle (100 nm in diameter), (b) selected area diffraction (SAD) of a single nanoparticle of Ag/Co/SiO_2

Table 3.3: Indexing of diffraction rings from SAD pattern shows presence of both Ag and Co in their elemental state within each nanoparticle. Co is in cubic phase (high temperature phase) and Ag is in its face-centered cubic phase.

Spot #	$d^{Expt.}$(Å)	d^{Theory}(Å)	Elements *(hkl)*
1	2.05±0.2	2.04/2.05	Co*(111)*/Ag*(200)*
2	1.79±0.2	1.77	Co*(200)*
3	1.56±0.1	1.54	Ag
4	1.43±0.1	1.44	Ag*(220)*
5	1.28±0.1	1.25/1.23	Co*(220)*/Ag*(311)*
6	1.19±0.1	1.18	Ag*(222)*
7	1.06±0.1	1.06	Co*(311)*

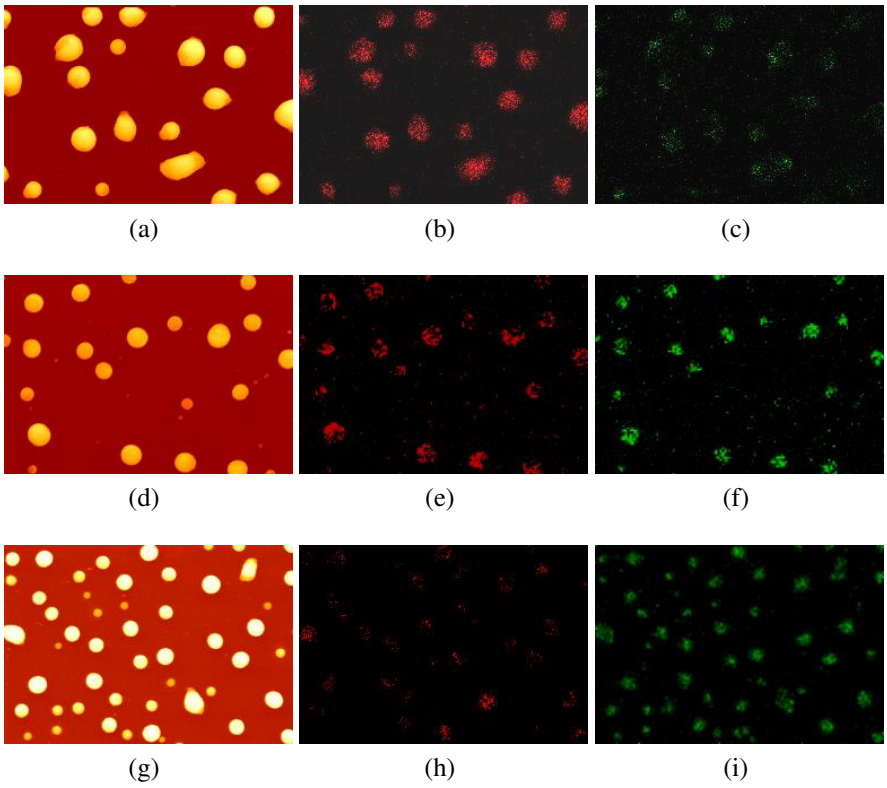

Figure 3.8: Energy dispersive x-ray mapping taken in SEM on the arrays of nanoparticles obtained from dewetting of Ag/Co/SiO_2 and Co/Ag/SiO_2, for three different thickness ratios of Co and Ag; (a-c) Co (1.5 nm)/Ag (5 nm), (d-f) Co (4.5 nm)/Ag (5 nm), and (g-i) Ag (1 nm)/Co (5 nm). The images (a), (d) and (g) are the SEM micrographs; (b), (e) and (h) are the elemental maps of Ag; and (c), (f) and (i) are the elemental maps of Co. The size of images in figures (a-c) is $2\,\mu m \times 1.4\,\mu m$, (d-f) is $3.5\,\mu m \times 2.4\,\mu m$, and (g-i) is $4\,\mu m \times 2.75\,\mu m$

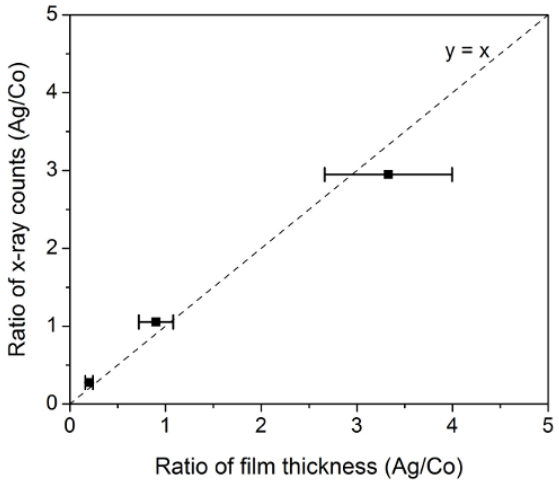

Figure 3.9: A plot of ratio of x-ray counts of Ag and Co obtained during x-ray mapping in SEM to the ratio of the initial film thicknesses of Ag and Co in the bilayer configurations. The dotted straight line indicates the points of equal ratios of x-ray counts and film thicknesses.

3.6 Conclusion

The thermodynamic principle of balancing the rate of Gibbs energy change with viscous dissipation was used to theoretically describe the spontaneous self-organization in ultra-thin bilayer metallic films. In this theory, the self-organized length scales can be obtained without need for linear or non-linear analysis of the fluid flow equations. For either arrangement, self-organization theory predicts characteristic length scales, but with different self-organizing behavior, as evidenced by the form of the thickness dependence. This difference was attributed to the nature of the intermolecular forces for the two configuration. The experiments of the self-organization in Co/Ag/SiO_2 and Co/Ag/SiO_2 bilayer systems by pulsed laser melting were performed. The resulting patterns show evidence for a spontaneous process with characteristic length scales. The experimentally measured behavior of

patterning length scale as a function of film thickness agrees very well with the prediction from thermodynamic theory. The morphological analysis in both bilayer configurations confirmed that thicker layer dominate the initial and intermediate morphologies. The microstructures of the nanoparticles revealed that each particle is made of both Ag and Co and the ratio of the metals in each composite is controlled by the initial film thickness of the films. These type of bilayer configurations could be useful towards manipulating the structural properties and controlling the length scales of nanoscale mixtures and alloys.

3.7 Acknowledgments

I would like to thank Nozomi Shirato for his help in Matlab programming for the bilayer calculations. Also, I would like to acknowledge Dr. Jeremy Strader for the bilayer laser heating model.

Chapter 4

Relation of dewetting morphology with free energy curvature in thin metal films

Summary

In this chapter, the morphological pathway of spontaneous dewetting of ultrathin Ag films on SiO_2 under nanosecond laser melting is investigated, which is found to be film thickness dependent. For films with thickness h between $2 \leq h \leq 9.5$ nm, the morphology during the intermediate stages of dewetting consisted of bicontinuous structures. For films $11.5 \leq h \leq 20$ nm, the intermediate stages consisted of regularly-sized holes. Measurement of the characteristic length scales for different stages of dewetting as a function of film thickness showed a systematic increase, which is consistent with the spinodal dewetting instability over the entire thickness range investigated. This change in morphology with thickness is consistent with observations made previously for polymer films [*A. Sharma et al, Phys. Rev. Lett., v81, pp3463 (1998); R. Seemann et al, J. Phys. Cond. Matt., v13, pp4925, (2001)*]. Based on the behavior of free energy curvature that incorporates intermolecular forces, the morphological transition thickness for the intermolecular forces for Ag on SiO_2 was investigated. The theory predictions agree well with observations for Ag. These results show that it is possible to form a variety of complex Ag nanomorphologies

in a consistent manner, which could be useful in optical applications of Ag surfaces, such as in surface enhanced Raman sensing.

4.1 Introduction

Silver (Ag) films and nanostructures have strong plasmonic activity and consequently, are very useful in the chemical detection of species via surface enhanced Raman scattering (SERS) [25, 126]. It is known that the magnitude of the localized field enhancement leading to increase in Raman scattering is very sensitive to the roughness or asymmetry (aspect ratio) of the nanostructures [127]. Therefore, controlling the morphology and nanostructure characteristics, of metals like Ag, in a reliable and cost-effective manner is very important towards further improving the sensitivity and selectivity of SERS detection.

One potential approach towards creating complex nanomorphologies in metals is to utilize the spontaneous dewetting of thin films [46, 128, 35, 4, 129, 130]. In the classical spinodal dewetting instability, an initially smooth film is unstable to height fluctuations because attractive intermolecular forces can exceed the stabilizing effect of interfacial tension [62, 53, 46]. As a result, a narrow band of wavelengths can spontaneously grow, eventually leading to film rupture and, more importantly, to morphologies with well-defined length scales [131, 33]. One of the important observations in polymer dewetting is the behavior of the dewetting morphology as the film progresses from its initially smooth state to a final stable state of particles. It has been observed that below a transition thickness h_T, the intermediate stage dewetting morphology consists of bicontinuous structures, while above, it consists of regularly sized holes [132, 133]. This change in morphology has been attributed to the form of the intermolecular forces influencing dewetting [33]. Specifically, for ultrathin films, with thickness between 1 and 20 nm, the film thickness-dependent intermolecular forces are made up of a long range attractive component, and a shorter-range repulsive component. The transition thickness can be identified from the thermodynamic

free energy of the system and, as shown by Sharma and Khanna [33], is located at the minimum in the curvature of the free energy. Consequently, the appearance of bicontinuous structures is correlated with films whose initial thicknesses lie to the left of the curvature minimum, while the formation of holes occur in films with thicknesses to the right of the minimum. In polymers, the the magnitude of h_T is found to be of the order of a few nm's. More importantly, knowledge of this transition can help guide the controlled fabrication of materials with different morphologies and length scales.

Recently, detailed investigations by various authors have shown that nanosecond laser irradiation of ultrathin metal films on non-wetting substrates can initiate a similar dewetting instability, producing robust and repeatable patterns with well-defined length scales [111, 48, 35, 4, 1]. Previously reported articles also showed that metal films can have different morphologies, including bicontinuous structures or holes, and in the case of Co on SiO_2 the transition was found to occur between 3 to 4 nm in film thickness [113, 37]. In this chapter, the dewetting pathway for Ag metal on SiO_2 substrates in the thickness range of $2 \leq h \leq 20$ nm under pulsed laser melting was explored. Besides the numerous applications associated with Ag nanostructures, another important reason to choose Ag for this dewetting morphological study is that nanosecond laser heating effects do not introduce any novel dewetting effects, due primarily to the large thermal conductivity of Ag [1]. To capture the various morphologies between the flat film and the final nanoparticle state, the dewetting was investigated as a function of number of pulses. Here Ag shows the bicontinuous morphology up to a thickness of ~9.5 nm, while above that it shows holes. Moreover, measurements of the characteristic length scale showed the expected h^2 behavior associated with spinodal dewetting over the entire thickness range investigated. Importantly, the experimentally observed transition thickness h_T agrees well with the value predicted by using the sum of possible intermolecular forces for Ag on SiO_2, and is analogous to results for polymer films. The results from dewetting of Ag films show that various complex morphologies, potentially useful towards plasmonic and non-linear optical properties, can be

robustly fabricated in a repeatable and controllable manner.

4.2 Experimental details

Ag films with thickness from $\sim$2 to 20 nm were deposited in high vacuum ($\sim 1 \times 10^{-8}$ Torr) by pulsed laser deposition at room temperature onto commercially obtained, optical quality, SiO_2/Si wafers consisting of 400 nm thick thermally grown oxide layer on polished $Si(100)$ wafers [48]. The deposition rate was typically $\backsim$ 0.3 nm/min. The energy dispersive X-ray spectrometry (EDS) was used to measure the Ag counts of the deposited films in a scanning electron microscope (SEM). The EDS counts were converted into an equivalent thickness value by using calibration based on step-height measurements of the film thickness. For every film thickness the surface roughness was measured via atomic force microscopy (AFM) and established an upper limit of 0.5 ± 0.2 nm for the average root mean square (RMS) roughness over the entire thickness range. Following the deposition, the films were irradiated in vacuum by a varying number of pulses n from a 266 nm ultraviolet laser having a pulse length τ_p of 9 ns. Irradiation was at normal incidence by an unfocused laser beam of area 1×1 mm^2 at a repetition rate of 50 Hz. Under these vacuum deposition and irradiation conditions, the film surface was never exposed to air and hence no role of oxygen or an oxide layer was expected. The dewetting morphology was investigated as a function of film thickness h, and the number of pulses n, which typically ranged between 10 to 10,500 pulses, for irradiation at laser energies at or just above the melt threshold of the films. It was shown earlier that the melt threshold energy is a function of the film thickness [37]. For each thickness the melt threshold was determined by a visible roughening of the metal film surface, as detected under high-resolution SEM within the longest time scale of the experiment (i.e. after $10,500$ laser pulses) [134]. The range of E used for the thickness regime investigated here was $60 \leq E \leq 120$ mJ/cm^2. For this irradiation condition, the heating and cooling rate of the metal film was of the order of 10^{10}

K/s with a total heating plus cooling time per pulse of $\sim$ 100 ns, which was much smaller than the spacing between pulses of 20 ms. Consequently, as it was quantitatively shown earlier [135], that negligible contribution to the morphology evolution was expected from processes in the solid state. Hence, any morphology changes occurred primarily during the liquid phase following each pulse. The EDS measurements confirmed that the laser irradiation did not result in substantial evaporation of the Ag, even after the longest irradiation experiments of 10,500 pulses.

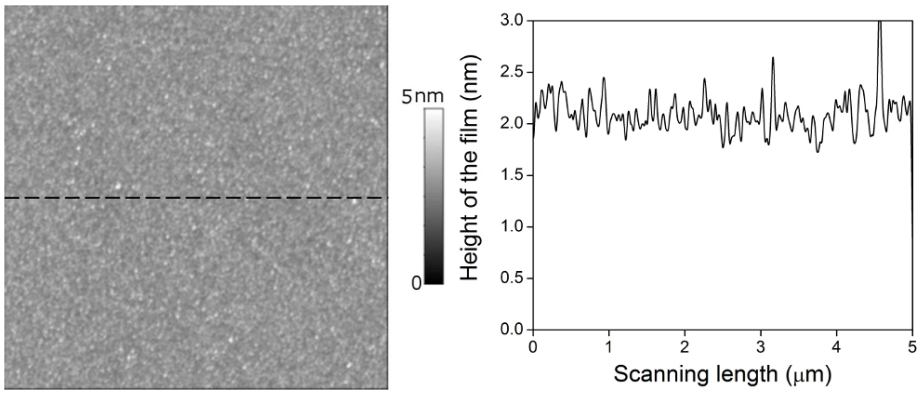

(a) (b)

Figure 4.1: (a) AFM image of an as deposited 2 nm Ag film on SiO_2 (image size is 5x5 μm^2). (b) A line profile taken along a horizontal dashed line of the AFM image (a) indicating the root mean square roughness (RMS) of the Ag film is $\sim$0.5$\pm$0.05 nm.

4.3 Results and discussion

Figure 4.1(a) shows the AFM micrograph of as-deposited 2 nm Ag film on SiO_2 substrate. The average RMS roughness of the film was measured by plotting the profile of the film along a horizontal dashed line (see Fig. 4.1(a)), which is shown in Fig. 4.1 (b), indicating RMS roughness to be $\sim$0.5$\pm$0.05 nm. Similar measurements were made for all the films investigated. In Fig. 4.2 (a-f), a series of SEM images denoting the early stage dewetting morphology, following irradiation by 10 laser pulses, is shown for a different Ag film

thickness. The important evidence from this series of images is the distinct transition in the general nature of the morphology between the 9.5 and 11.5 nm films. Up to 9.5 nm [Fig. 4.2(a-d)], the morphology generally consists of asymmetric undulations or a bicontinuous type structure. On the other hand, for the 11.5 and 20 nm films [Fig. 4.2(e-f)], regular holes are clearly visible. Quantitative information about the spatial characteristics of these morphologies was obtained by evaluating the fast Fourier transform (FFT) of the SEM image contrast, which is related to the dewetting film's height variations. The resulting FFT information of the contrast correlation is shown in the inset of each figure, and the important information here is the annular form for each of the films. This annular FFT is indicative of a narrow band of characteristic length scales for the height variations on the surface. This is an important observation given that the dewetting morphology can progress via either of the three pathways: homogeneous nucleation, heterogeneous nucleation, or spinodal dewetting [67]. In the case of homogeneous nucleation, the features are randomly distributed, both spatially, and in time, and no characteristic length scale should appear in this type of dewetting [55]. Heterogeneous nucleation can occur due to defects, impurities or other experimentally imposed heterogeneities. In this type of dewetting, a characteristic length scale could appear at the early stages of dewetting only in the presence of available ordered nucleation sites. However, the spatially ordered heterogeneities on the substrate surface, as well as on the as-deposited films, prior to irradiation, was never observed. Therefore, the results presented here point strongly to the third option, which is spinodal dewetting [54].

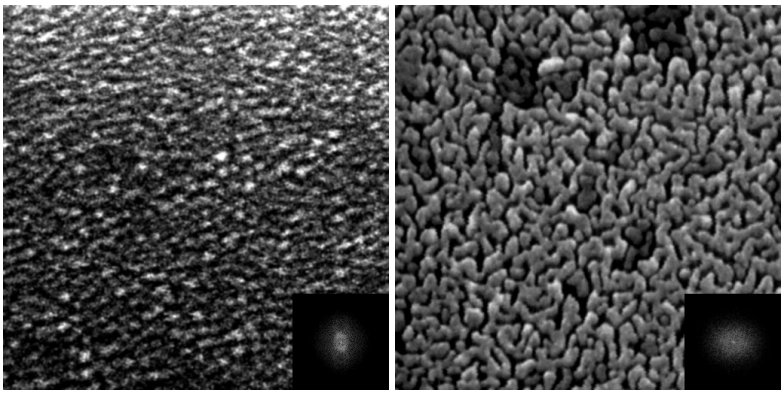

(a) (b)

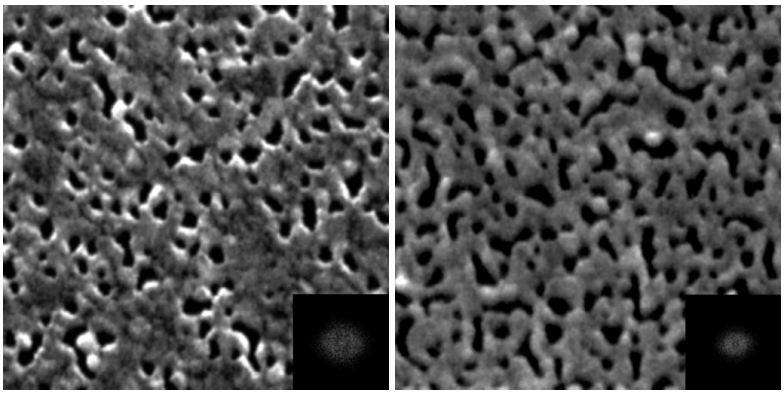

(c) (d)

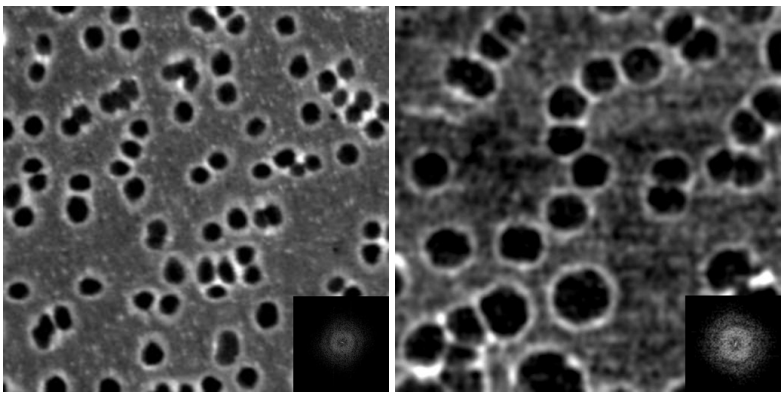

(e) (f)

Figure 4.2: (a-f) SEM images of the early stage dewetting morphologies following irradiation by 10 laser pulses. The film thickness from (a) to (f), corresponds to 2, 4.5, 7.4, 9.5, 11.5, and 20 nm, respectively. Also shown in the inset of each figure is the FFT of the contrast correlations of the SEM images. The annular spectrum indicates that a well-defined length scale characterizes each pattern. The size of image (a) is 0.5x0.5 μm^2, images (b-d) are 1.5x1.5 μm^2, and images (e) and (f) are 3x3 μm^2 and 10x10 μm^2, respectively.

The characteristic length scale associated with spinodal dewetting is established at the very early stages of film deformation [46]. The early stage undulations, which occur prior to the appearance of large height variations in the film, are extremely difficult to capture experimentally. However, the subsequent morphology, which is a result of ripening of the initial undulations, forms as dewetting progresses and has length scales directly related to the initial length scale. Therefore, as shown by many authors, the final nanoparticle length scale, can be used as a measure of the thickness-dependent behavior [53, 35]. Here, the length scales were measured at different stages of the dewetting process as a function of film thickness. In Fig. 4.3(a-c), the progression of the morphology is shown for the 4.5 nm film, while Fig. 4.3(e-g) shows the same for the 11.5 nm films as a function of laser pulses between 10 and 10,500 shots. Figures 4.3(d) and (h) are the radial distribution functions (RDF) for each stage for the 4.5 and 11.5 nm film, respectively. From the position of the peaks in such RDF measurements, obtained directly from the FFT's, it was possible to generate the characteristic length scale present in the pattern at each stage. The result of measuring length scales from these progressions is shown in Fig. 4.4(a). The early stage behavior is shown by the closed squares, the intermediate stage is shown by open triangles, while the final nanoparticle state is shown by open circles. One important observation from this measurement is that no dramatic change in length scale is seen when the morphology changes from the bicontinuous to the hole structures, i.e. between 9 to 11 nm. This strengthens the argument that both morphologies can arise for spinodal dewetting of Ag. Since the characteristic length scale for spinodal dewetting is known to vary as $\lambda_{sp} \propto h^2$, the trend line of h^2 was plotted for the early stage (solid line) and nanoparticle stage (dotted line) data sets with an h^2 trend. The early stage dewetting agrees reasonably well with the spinodal trend over the regime investigated, confirming a previously reported result for Ag, based on the behavior of the nanoparticle state [1]. An important observation can be made on the apparent deviation of the intermediate and final stage length scales for the thickest film investigated, i.e. the 20 nm film. The nanoparticle length appears much smaller than

the trend (dotted line), while the intermediate state appears much larger. This can be understood as follows. The drop in the nanoparticle length scale is due to the nearest-neighbor interparticle spacing being dominated by a Rayleigh-like break-up of the arms of the polygon, as shown in Fig. 4.4(b). In contrast, particles in the 11.5 nm film form at the vertex of the polygons formed during the dewetting stage [Fig. 4.3(g)]. A similar argument, based on a change in the feature shape being measured, is likely to explain the intermediate state behavior. As shown in Fig. 4.3(e-g), the progression of the hole morphology is through merging of the holes into polygons, whose size (diameter) will be dependent upon the number of holes it was formed from. It is quite likely that the large increase in length scale for the intermediate state of the 20 nm film is because the measured length scale is for polygons formed from numerous holes.

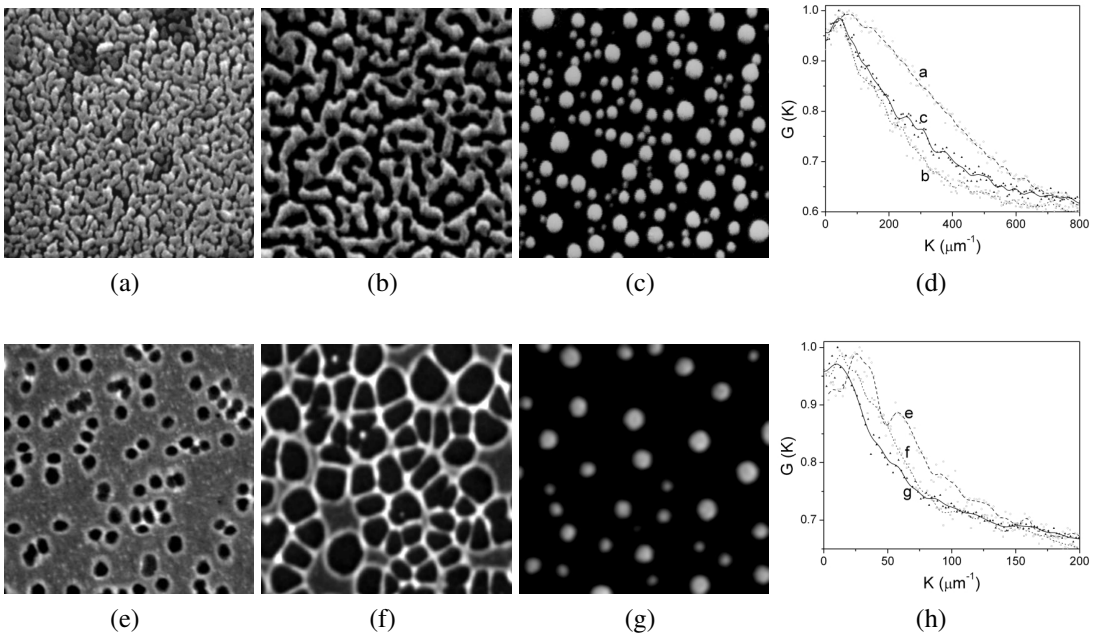

Figure 4.3: (a-c) SEM images (1.5x1.5 μm^2) of progression of dewetting in the 4.5 nm thick film with increasing number of laser pulses (10, 100, 10,500). (d) Plot of the radial distribution function (RDF) for each stage of dewetting. The peak position in RDF was used to estimate the characteristic length scales. (e-g) Progression (3x3 μm^2) of dewetting in the 11.5 nm thick film with increasing number of laser pulses (10, 100, 10,500). (h) Plot of the radial distribution function for each stage. The letters in plots (d) and (h) indicate the RDF's for the corresponding SEM images.

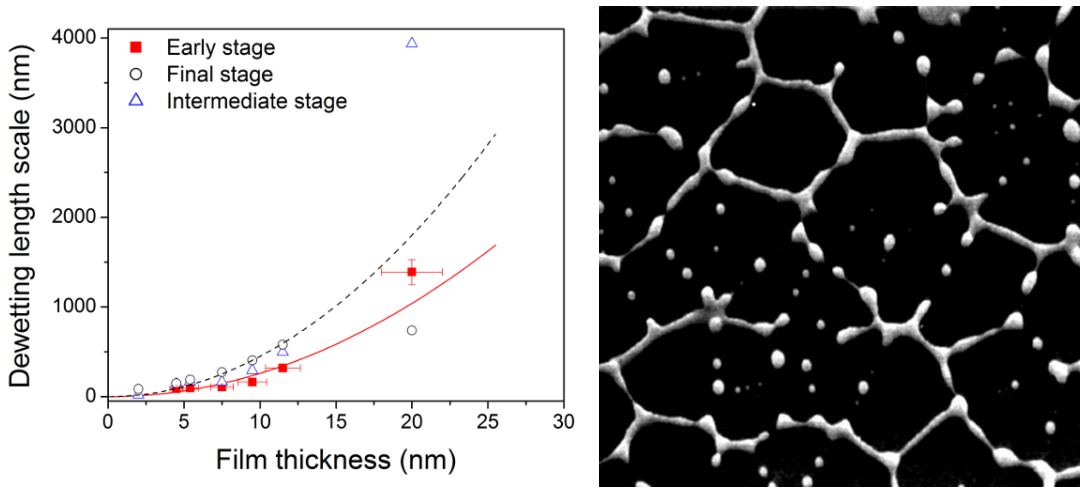

(a) (b)

Figure 4.4: (a) Plot of the characteristic length scale for various stages of progression as a function of film thickness (h). The early stage behavior is shown by the closed squares, the intermediate stage is shown by open triangles, and the final nanoparticle state is shown by open circles. Trend lines with h^2 variation for the early stage (solid line) and nanoparticle stage (dotted line) data are also shown. For clarity, the error bars for the intermediate and final state are not shown. (b) SEM image (15x15 μm^2) of the intermediate stage to nanoparticle stage transition for a 20 nm film showing that the break-up of the arms of the polygons is via a Rayleigh-type process leading to multiple nanoparticles in each arm.

The above results provide a strong case for Ag dewetting via the spinodal process, with additional support coming from that fact that similar morphological characteristics are observed when polymer films dewet by the spinodal instability. As mentioned in the introduction, polymer films have been observed to have a bicontinuous to hole transition at thicknesses h_T of a few nm and the theoretical position of this thickness has been correlated to the nature of the free energy [33, 133]. Specifically, the location of minima in the free energy curvature has been correlated to this transition thickness. To determine if a similar behavior is seen for the Ag metal, a sum of different types of attractive and repulsive intermolecular interactions have been used to estimate the free energy and its curvature as a

function of thickness h for Ag on SiO_2. Since the films are very thin, the gravitational term in our calculations was neglected.

Table 4.1: List of metal parameters required for free energy analysis

Metal	$\gamma_{M/Vacc}$ (J-m^{-2}) [118]	θ (degree)	S^p (J-m^{-2}) [136]	A (J) [60]	h_c using Eq. 4.3 (nm)	h_T using Eq. 4.4 (nm)
Ag	0.925	82	0.79	-1.33x10^{-19}	0.300	0.3 - 11.45
Au	1.145	88	1.11	-1.76x10^{-19}	0.293	0.29 - 11.92
Co	1.882	101	2.26	-3.1x10^{-19}	0.273	0.27 - 12.10
Cu	1.304	92	1.35	-2.08x10^{-19}	0.288	0.29 - 11.62
Fe	1.870	101	2.24	-2.9x10^{-19}	0.265	0.26 - 11.88
Mn	1.152	88	1.12	-8.12x10^{-22}	0.019	2.64 - 19.23
Ni	1.781	100	2.10	-9.9x10^{-20}	0.160	1.13 - 13.47
Pt	1.746	100	2.04	-2.56x10^{-19}	0.259	0.26 - 11.94
Ti	1.525	96	1.69	-4.32x10^{-19}	0.372	0.37 - 10.72
V	1.770	100	2.08	-1.74x10^{-19}	0.212	0.21 - 12.58

4.3.1 Free energy analysis to determine transition thickness h_T

The intermolecular interaction free energy of a uniform thin film can be realized by first describing the disjoining pressure acting on a film. Consider a liquid film of height h on top of a flat substrate. The thickness dependent disjoining pressure, $\Pi(h)$, can be expressed by adding a long-range attractive (Van der Waals interaction) and a short range repulsive interaction between the various interfaces formed as a result of having the film on a substrate. The repulsive term typically consists of two parts: (i) a Lennard-Jones (L-J) type repulsion [137] which appears due to the electron cloud interaction, and (ii) an electrostatic force, which is a result of electric layers forming at the liquid-substrate interface.

The total disjoining pressure, by considering a long-range attraction, a short range repulsion expressed as a Lennard-Jones type form [137], and the electrostatic force [137, 33], is given by:

$$\Pi(h) = \frac{A}{h_c^3}\left[\left(\frac{h_c}{h}\right)^3 - \frac{1}{3}\left(\frac{h_c}{h}\right)^9\right] + \frac{S^p}{l}exp(-h/l) \tag{4.1}$$

Here, A is the Hamaker coefficient, which has a negative value in units of Joule, and h_c is the critical length at minimum $\Pi(h)$. S^p is the spreading coefficient which is related to the magnitude of electrostatic part of the disjoining pressure, and l is a correlation (or Debye) length. Using Eq. 4.1, the free energy density (energy/area) of a uniform film can be written as:

$$\Delta G = \frac{A}{2h^2} - \frac{Ah_c^6}{24h^8} + S^p exp(-h/l) \tag{4.2}$$

where, h_c is defined as:

$$\frac{A}{h_c^2}\frac{3^{4/3}}{8} = -2\gamma sin^2(\theta/2) \tag{4.3}$$

and h_T (the transition thickness) is calculated from the position of the minimum in the free energy curvature as:

$$\frac{\partial^2 \Delta G}{\partial h^2} = \frac{3A}{h^4} - \frac{3Ah_c^6}{h^{10}} + \frac{S^p}{l^2}exp(-h/l) = 0 \tag{4.4}$$

The above analysis was performed for Ag on SiO_2 substrate, and the correlation length l was taken to be in the range of $0.2 - 1.0$ nm [136]. The values of the constants used in the analysis for Ag are given in Table 4.1. Table 4.1 also consists of material parameters for few other metals of interest, where the value of h_T is estimated by considering that l lies between 0.2 to 1 nm. The typical transition thickness (h_T) calculated using Eq. 4.4 for Ag appears to be between 0.3 and 11.45 nm. The free energy and curvature plots using Eq. 4.2 *and* 4.4 and the correlation length $l = 1$ nm for Ag are shown in Fig. 4.5. With this result the following observations were made. In polymer films, the bicontinuous structures are observed for the thinner films, while holes are observed in the thicker ones. Similarly, for the presented case of Ag films on SiO_2 substrate, the bicontinuous structures are obtained

for films $h_T \leq 9.5$ nm, while above this thickness the morphology evolution starts with the formation of holes. This experimental result matches well with the theoretical prediction of 11.45 nm, provided a correlation length of $l = 1$ nm is used.

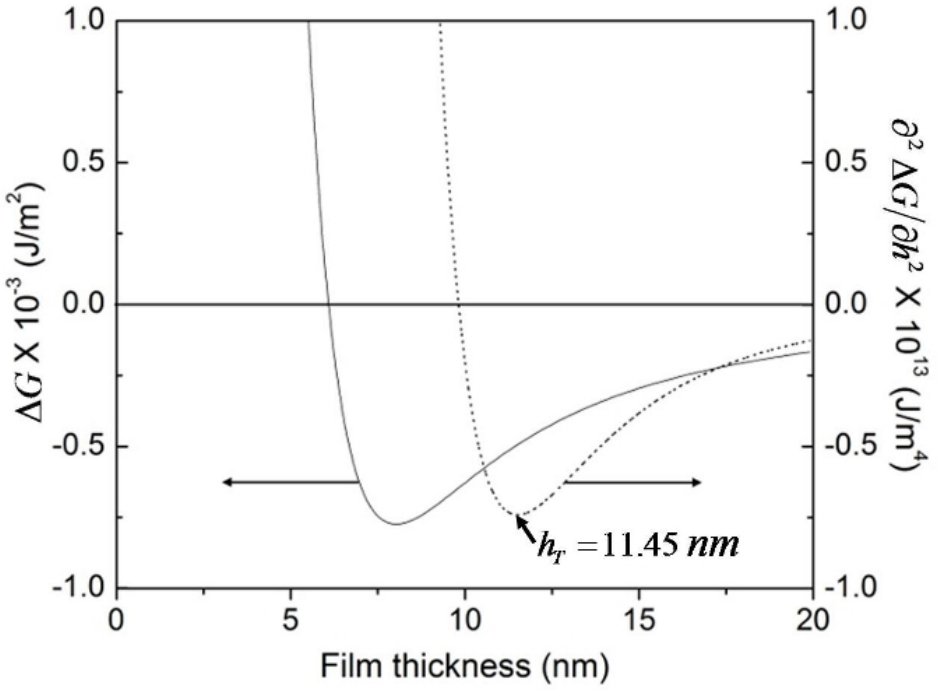

Figure 4.5: Plot of the free energy, ΔG, (solid line) and free energy curvature, $\frac{\partial^2 \Delta G}{\partial h^2}$, (dashed line) vs film thickness for Ag on SiO_2 using Eq. 4.2 and Eq. 4.4, respectively. The transition thickness h_T corresponds to the minimum in the curvature and occurs at ~ 11.45 nm for a correlation length of 1 nm.

4.4 Conclusion

In conclusion, the morphology evolution in nanometer thick Ag films $(2 \leq h \leq 20 nm)$ under melting by nanosecond laser pulses was investigated. The initial dewetting morphology is found to be a bicontinuous morphology for films with thickness $\leq$9.5 nm, while discrete holes appear for films with thickness > 11.5 nm. Evaluation of the characteristic dewetting length scales indicated a good agreement with a h^2 trend, which was evidence

for the spinodal dewetting instability. The observations of the different morphologies and a transition thickness is consistent with the behavior observed previously for polymer films. The experimentally observed transition value for Ag, of between 9.5 - 11.5 nm, agrees well with predictions from intermolecular forces. This work shows that complex and controllable morphologies can be obtained for Ag, but more insight is needed to understand the physical origins of dewetting pattern morphologies in thin metal films.

4.5 Acknowledgments

I would like to acknowledge Dr. Jeremy Strader and Ritesh Sachan for their contributions to get AFM image [Fig. 4.1] and experimental length scale for 2 nm Ag film on SiO_2 [included in Fig. 4.4].

Chapter 5

Size-dependent magnetization in hemispherical Co and Fe nanomagnets on SiO_2

Summary

Nanosecond pulsed-laser melting of ultrathin metal films can lead to self-organized arrays of spherical nanoparticles. This technique was applied to assemble arrays of nanoparticles of the soft elemental ferromagnets, Co and Fe, on SiO_2 substrates. Surface morphology studies using scanning electron microscopy and atomic force microscopy established that the nanoparticles were nearly hemispherical. Magnetic properties of these nanoparticles in the size range of 30 - 250 nm diameter were investigated by magnetic force microscopy (MFM) under zero applied field at room temperature in conjunction with simulations of the magnetic tip-particle interaction. In the case of Co, particles up to 180 nm diameter were found to be single-domain (SD) with the magnetization direction oriented predominantly in-plane ($\leq 45^o$) for the smaller particles (≤ 75 nm) and out-of-plane ($45-90^o$) for the larger particles (≤ 180 nm). Similarly in the case of Fe nanoparticles, within the SD

size of 150 nm, the particles upto 55 nm are predominantly in-plane. Magnetic hysteresis measurements on Co arrays at room temperature confirmed that the arrays consisted of a mixture of in-plane and out-of-plane orientations. Microstructural analysis by transmission electron microscopy revealed that the nanoparticles had a granular microstructure with the average grain size increasing with particle size. This size-dependent magnetic orientation is inconsistent with the expected in-plane orientation due to shape anisotropy. The magnetization direction of the nanomagnets was explained by the size-dependent residual strain *and* the microstructures formed by rapid laser processing. This idea was supported by the significant increase in in-plane orientation of larger particles following thermal annealing in Co arrays. These studies suggest that anisotropic nanomagnets comprised of nearly hemispherical polycrystalline particles can be synthesized with desired magnetic orientations by fast laser thermal processing.

5.1 Introduction

Present research on magnetic devices is concentrated on reducing the component size in order to achieve high density. Nanosized magnetic structures are important for many applications, such as in non-volatile and high speed magnetic random access memories (MRAM) [32, 138], high density magnetic data storage [139, 140, 21], opto-electronics [141] and biological applications [142, 143]. Some of these applications require well-defined zero-field magnetization directions of the nanoparticles. For instance, in the case of recording media, strong magnetic anisotropy is desired with in-plane (longitudinal media) or out-of-plane (perpendicular media) orientations. Traditionally, this magnetic anisotropy has been achieved in nanostructured materials through design of high-aspect ratio structures and/or selecting specific orientations of crystalline phases with large magnetocrystalline anisotropy [144, 145, 54, 146, 147]. It is widely accepted, based on energy minimization arguments, [93, 12] that magnetic nanoparticles with typical dimensions between 10 to 100 nm should be single domain compared to multi-domain behavior for the larger particles. The direction of the zero-field magnetization in such nanostructures is a strong function of size, shape, and processing conditions. As the size of the magnetic structures diminishes, the properties show dramatic changes compared to bulk when the surface and interface magnetic energies [80, 81] become comparable to the volume (magnetostatic) energy [93]. Shape is significant because it introduces large magnetic shape anisotropy. For instance, polycrystalline thin films, which have large shape anisotropy (large in-plane compared to out-of-plane dimensions), tend to show zero-field magnetization along the plane of the film because of lower demagnetization energies. On the other hand, processing conditions can also introduce additional magnetic anisotropy. Several studies on ultrathin epitaxial films show out-of-plane magnetization [148, 149] because of large magnetoelastic energy arising from epitaxial strains and/or surface anisotropy. This chapter shows that the hemispherical polycrystalline nanoparticles of elemental ferromagnets like Co and Fe can be oriented in a specific direction by introducing additional anisotropies dependent on the processing

conditions, which, in this particular case, arises from fast laser processing.

Recently, a self-organizing route was developed to assemble spatially ordered nanoarrays of nearly hemispherical nanoparticles of ferromagnetic (Co, Fe) [85, 99] and paramagnetic materials (Ti, V, Cu, Ag) [113, 150, 151, 152, 1]. In this process, ultrathin metal films on an inert substrate (SiO_2) are irradiated by nanosecond (ns) laser pulses. Self-organization (SO) occurs in the molten phase through a thin film hydrodynamic instability, which causes the spontaneous dewetting of the ultrathin continuous metal film into patterns with well-defined length scales [153, 123]. When the dewetting is initiated by a spatially uniform laser beam, with increasing number of laser pulses, the morphology of the thin film progresses to regularly-sized holes, to cellular networks of polygonal shapes, to stable nanoparticle arrays [153]. The ensuing arrays show spatial short range order (SRO) in the interparticle spacing and monomodal size distribution [153, 123]. It is shown that by varying experimental parameters, such as film thickness and the spatial distribution of the laser intensity, the spacings and ordering of the pattern could be modified in a predictable manner [150, 34]. However, a detailed magnetic characterization of the nanoparticle arrays has not been reported.

This chapter explains the correlations of particle size, shape and microstructure, with the magnetic properties of the nanoparticles in these self-organized arrays. The ensuing array characteristics, including the particle size distribution and particle contact angle, were determined using atomic force microscopy (AFM) and scanning electron microscopy (SEM). Transmission electron microscopy (TEM) measurements were performed to study the microstructures inside the nanoparticles. The orientation of the magnetization of the nanoparticles were determined by magnetic force microscopy (MFM) measurements in zero applied field at room temperature, and comparing them with numerical simulations of the MFM images. The as-prepared Co and Fe nanoparticles were found to be nearly hemispherical, showing single domain magnetic behavior upto 180 nm diameter for Co and 150 nm for Fe; the larger particles were multi-domain. Interestingly, the magnetization direc-

tion changed from a predominantly in-plane orientation for the smaller nanoparticles to an out-of-plane orientation for the larger ones. TEM investigations showed that the smaller particles (<40 nm) were single-grained and the larger particles multi-grained (polycrystalline), with random grain orientations. A clear understanding of this size-dependent magnetization behavior was possible by comparing the relative contributions of different energy terms such as, the dipolar interaction energy, demagnetization energy, magnetocrystalline anisotropy energy and magnetoelastic anisotropy energy (or magnetostrictive energy), and correlating them with the nanostructures of the individual nanoparticles. *This detailed magnetic study of multi-grained near hemispherical nanoparticles suggests that fast thermal processing could be used to control and manipulate nanomagnetic domain and domain switching behavior.*

5.2 Experimental procedure

Thin films of Co (3.2 nm) and Fe (4.5 nm) were deposited on commercially available optical quality SiO_2/Si(100) wafers using the electron-beam evaporation technique under ultrahigh vacuum ($\sim 1 \times 10^{-8}$ Torr). The thermally grown SiO_2 layer on Si was 400 nm thick. Prior to evaporation, the substrates were cleaned by ultrasonic rinsing in acetone, ethanol and DI water. The film deposition rate was monitored by a quartz crystal based deposition rate monitor. The final thickness of each film was further verified by quantitative energy dispersive x-ray spectroscopy (EDS) measurements and by comparing the signals with calibrated metal films of known thicknesses [123]. Following deposition, the samples were irradiated under vacuum with a uniform Nd:YAG laser beam at normal incidence, operating at its 4^{th} harmonic of 266 nm wavelength. A 9 ns laser pulse width with a repetition rate of 50 Hz was used. The laser energy density was chosen to be just above the film melt threshold, which was required to achieve self-organization [153]. Typically, $\sim$3000 pulses with a laser energy density of $\sim 100-120$ mJ/cm^2 were necessary to create the final nanoparticle pattern. To study the effect of thermal annealing on the magnetic

behavior of particles, a Co array sample was annealed *in-situ* at 470°C for 3 hours under high vacuum (2×10^{-6} Torr). The as-prepared and annealed arrays were characterized for particle size, shape and magnetic properties under ambient conditions.

Scanning electron microscopy (SEM, Hitachi S-4500) images were analyzed to obtain the particle size and spatial distribution. To estimate the contact angle, θ, independent measurements of the particle height were made using a tapping mode atomic force microscope (AFM, Digital Instruments Dimension 3000 Multimode IIIA scanning probe microscope) and utilizing the relation $\theta = 90 + sin^{-1}\left[(h - D/2)/D/2\right]$, where h and D are the height and diameter of the particle, respectively. The magnetic domain orientation with respect to the substrate was determined from the bright and dark contrast of the magnetic force microscopy (MFM, Digital Instruments Dimension 3000) images and comparing them with the simulated images, based on tip-sample interactions (see Sec. 5.3.3). The scan height for all the MFM measurements was 50 nm. Scanning in different directions (0^o and 90^o) and scanning heights (20 - 100 nm) was performed to ensure that the resulting MFM information was consistent, and not influenced by tip-sample interactions that could modify the magnetization of the samples. The MFM Si-probes, coated with a few tens of nm thick CoCr alloy, were obtained from Asylum research (ASY) [154]. Magnetic hysteresis measurements were performed in a quantum design physical properties measurement system (PPMS). Transmission electron microscopy was done using two different systems (200 KeV JEOL 2100F and JEOL 2000FX). The plan-view TEM samples were prepared using a well-known Si-chemical etching procedure [see ref. [155] for detailed information].

5.3 Results

5.3.1 Morphology of Co and Fe nanoarrays

The single beam laser irradiation of 3.2 nm thick Co film produces an array of nearly hemispherical nanoparticles with spatial SRO as shown in the SEM micrograph, Fig. 5.1(a).

The inset shows the power spectrum corresponding to the spatial distribution of particles, obtained by fast Fourier transformation (FFT) of the SEM micrograph. Short range order in the interparticle spacing is confirmed by the annular ring visible in the power spectrum. From the average diameter of the annular ring, the average interparticle spacing was estimated to be 290 nm, which is consistent with the prediction of thin film dewetting theory [153, 1]. The particle size distribution is shown in Fig. 5.1(b). The average diameter (from the SEM measurement) and average height (from AFM measurement, Fig. 5.8(a)) was estimated to be $D = 88 \pm 23$ nm and $h = 55 \pm 16$ nm, respectively. The contact angle calculated using the formula mentioned in section 5.2 was 104 ± 22^{o}. The morphology was also studied after vacuum annealing of Co particles similar to as-prepared Co array, mentioned above. The SEM micrograph of annealed Co arrays Fig. 5.2(a), along with the power spectrum (the inset), confirmed the SRO. Fig. 5.2(b) shows the size distribution of the annealed Co nanoparticles, which was similar to the as-prepared distribution (Fig. 5.1(b)). The average spacings, average diameter, and the average height were measured to be 285 nm, 85 ± 25 nm and 53 ± 12 nm, respectively, which once again confirmed that the thermal anneal did not substantially change the size distribution and spacings of the nanoparticles.

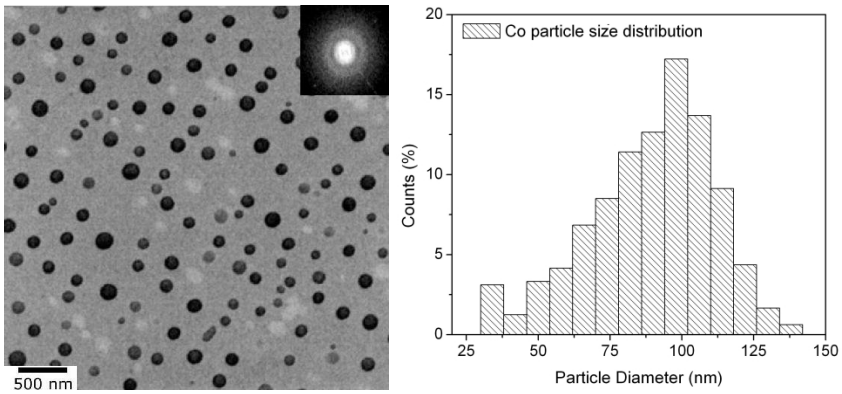

(a) (b)

Figure 5.1: Array morphology and size distribution for the as-prepared Co nanoarrays made from a 3.2 nm thick Co film: (a) SEM micrograph of as-prepared Co nanoarrays; the inset shows the FFT, indicating spatial short range order, (b) Particle size distribution obtained from image (a).

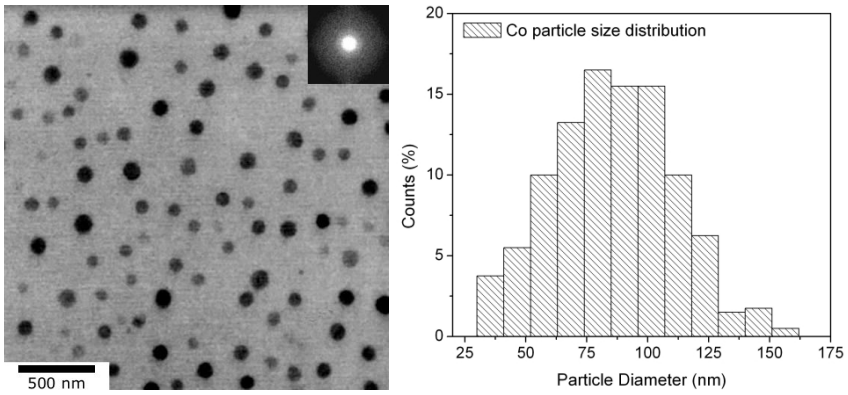

(a) (b)

Figure 5.2: Morphology and size distribution of the annealed Co nanoarrays made from a 3.2 nm thick film after 470^{o}C (for 3 hr)anneal under vacuum. (a) SEM micrograph of annealed Co nanoarrays; the inset shows the FFT, indicating spatial short range order, (b) Particle size distribution obtained from image (a).

Similarly, the irradiation of a 4.5 nm thick Fe film results in an array of hemispherical Fe nanomagnets on SiO_2 substrate with a characteristic SRO, as shown in the SEM micrograph

in Fig. 5.3(a) and the inset. From the particle size distribution (Fig. 5.3(b)), the average diameter, height, and spacing between the particles were measured to be 68 $\pm$ 20 nm, 40 $\pm$ 12 nm and 320 nm, respectively. This corresponds to an equilibrium contact angle of 100 $\pm$ 21^{o}. Similar to Co arrays, the particle size and spacings were in agreement with the characteristic length scales expected from classical dewetting of spinodal-like thin film systems[153, 1].

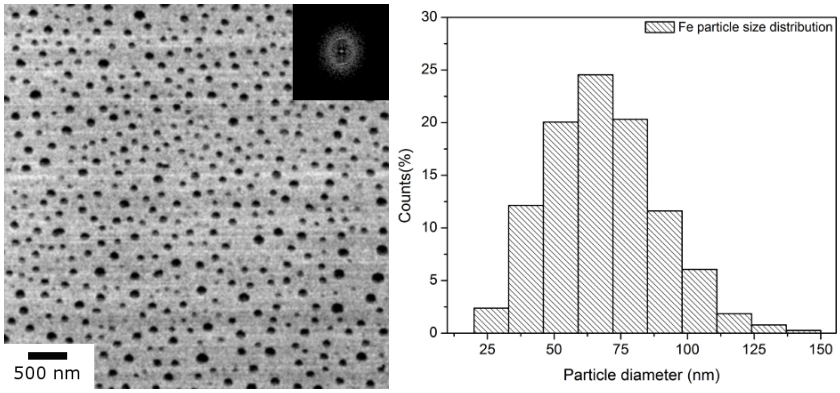

(a) (b)

Figure 5.3: (a) SEM micrograph of arrays of Fe nanoparticles made from 4.5 nm thick Fe film and the corresponding FFT (shown in the inset) confirms the SRO. (b) Particle size distribution obtained from image (a).

5.3.2 Nanostructure of Co particles in arrays

Fig. 5.4(a) and (b) shows the plan-view of bright-field (BF) and dark-field (DF) TEM images for the array from the same location, while Fig. 5.4(c) shows the corresponding selected area diffraction (SAD) pattern. The diffraction spots corresponding to each d-spacing were distributed in several directions, implying the random orientation of the grains. The d-spacings and the corresponding crystallographic planes for the observed diffraction spots (indicated on Fig. 5.4(c) by numbered arrows) are presented in Table 5.1. The experimentally measured d-spacings agreed well with the theoretical d-spacings [156]

for cubic Co, which is the stable phase above 450 ^{o}C. This confirmed that the ns pulsed laser processing was fast enough to quench and retain the high temperature Co phase. Dark-field analysis (Fig. 5.4(b)) confirmed the granular microstructure of the nanoparticles from the dark and bright regions within each nanoparticle. By analyzing the BF and DF contrast, an estimate of the average grain size within each particle was made. The result, shown by the solid circles in Fig. 5.13, indicates an increase in average grain size with particle size. The uncertainty in the grain size measurement ($\sim \pm 10\%$) came primarily from approximating irregular shaped grains to be circular, and from the statistical averaging of the grain size over a number of particles of the same diameter.

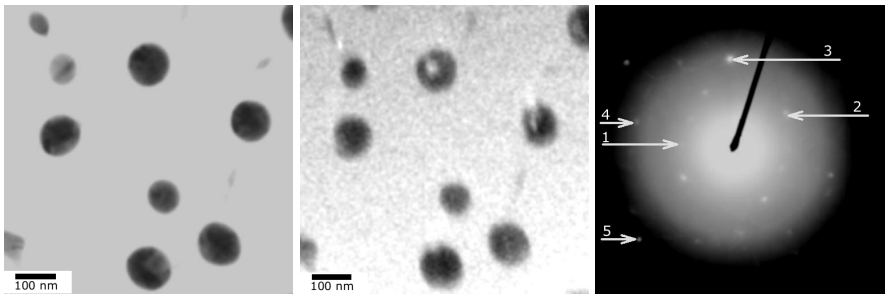

(a) (b) (c)

Figure 5.4: Plan-view TEM micrographs showing microstructure of as-prepared Co nanoparticles: (a) Bright-field, and (b) Dark-field images from the same area, (c) SAD pattern confirming cubic phase for Co. The numbered spots (1 - 5) are indexed in Table 5.1.

Table 5.1: Indexing of diffraction spots and rings in SAD for as-prepared Co arrays. The numbers in the first column correspond to the markings on the SAD pattern shown in Fig. 5.4(c).

Spot #	$d^{Expt.}$(Å)	d^{theory}(Å) *and* (*hkl*) Co - Cubic phase
1	2.0±0.1	2.04 *(111)*
2	1.7±0.1	1.77 *(200)*
3	1.2±0.1	1.23 *(220)*
4	1.1±0.1	1.06 *(311)*
5	0.80±0.05	0.79 *(024)*

Fig. 5.5(a-c) shows the plan-view TEM and SAD for the 450^{o}C (for 3 hr) annealed particles. The most important change after anneal was the formation of faceted grains, compared to smooth circular shape for the as-prepared particles. The SAD (Fig. 5.5(c)) again showed a polycrystalline microstructure; however, in contrast to the cubic phase for the as-prepared nanoparticles, the annealed samples consist of hexagonal [157] as well as cubic phases. The d-spacings and the corresponding indexing of spots, indicated by numbers (6 - 12), on the SAD are presented in Table 5.2. By using the BF and DF analysis, the grain and particle sizes were estimated, as shown by open squares in Fig. 5.13. While the trend is similar to the as-prepared arrays, the grain size is slightly larger, indicating some ripening of the grains inside the particles during anneal.

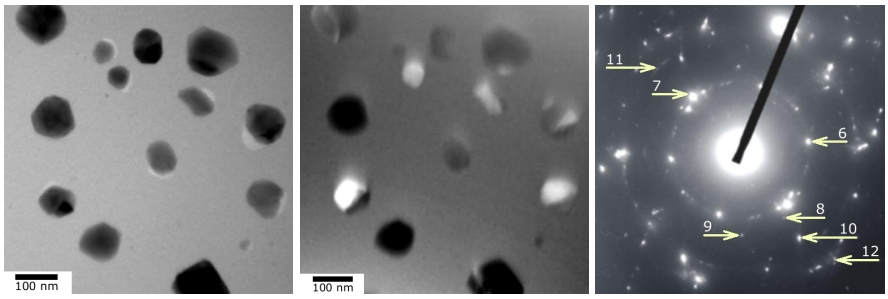

(a) (b) (c)

Figure 5.5: Plan-view TEM micrographs showing microstructure of annealed Co nanoparticles: (a) Bright-field, and (b) Dark-field images from the same area, (c) SAD pattern shows evidence for both hexagonal and cubic phases for Co and the diffraction spots numbered (6-12) are indexed in Table 5.2.

Table 5.2: Indexing of diffraction spots in SAD shown in Fig. 5.5(c). Numbers in the first column correspond to the markings on the SAD pattern shown in Fig. 5.5(c).

Spot #	$d^{Expt.}$(Å)	d^{theory}(Å) *and* (*hkl*) Co - hexagonal phase	d^{theory}(Å) *and* (*hkl*) Co - Cubic phase
6	2.2±0.1	2.16 *(100)*	-
7	2.0±0.1	-	2.04*(111)*
8	1.9±0.1	1.91 *(101)*	-
9	1.7±0.03	-	1.77 *(200)*
10	1.4±0.07	1.48 *(102)*	-
11	1.3±0.1	-	1.23*(220)*
12	1.1±0.1	-	1.06*(311)*

5.3.3 Simulation of MFM response for hemispherical particles

In order to accurately interpret the experimental MFM image contrast presented in Sec. 5.3.4, a theoretical analysis of the interaction between the MFM tip and the uniformly magnetized hemispherical particles was performed and the contrast in the MFM images for different orientations of magnetization were simulated. The system used is a Dimension 3000 AFM/MFM, which uses Tapping Mode and Lift Mode (trademarks of Digital Instruments, Inc.) techniques to map the topography of a sample and gather its magnetic force information [158]. The oscillating probe rasters scans across the surface of the sample, performing two passes for each line in the raster. On the first pass, the instrument taps the probe across the surface and gathers the sample topography along the line. On the second pass, a user-defined offset is added to this topographic information such that the probe tip closely follows the sample topography at a fixed height above the surface, without touching the sample. During the second pass, the probe is driven at a constant frequency close to the probe's nominal resonant frequency, and the instrument records variations in the phase of the probe's motion. The result of the raster scan is a pair of aligned images: a topography image and a magnetic force phase image. Since the phase is observed at a fixed height above the sample, the phase image is largely independent of the topography image.

The phase variations ψ are approximately proportional to the force gradient in the direction of the probe's oscillation [159, 160]. Taking this direction to be the vertical z axis, the phase is written as;

$$\psi \propto \frac{\partial \mathbf{F}_z}{\partial z} \tag{5.1}$$

The force on the probe can be expressed as the gradient of the Zeeman energy for the probe's magnetized tip ($\mathbf{M}_{tip}$), which responds to the stray field created by the sample ($\mathbf{H}_{samp}$) [161];

$$\mathbf{F} = -\bigtriangledown \int_{V_{tip}} \mathbf{M}_{tip} \cdot \mathbf{H}_{samp}\, dV \tag{5.2}$$

This integral here is carried out over the magnetic volume of the tip. Using the substitution $\mathbf{H}_{samp} = -\bigtriangledown \Phi_{samp}$, this can be rewritten as [162];

$$\mathbf{F} = \bigtriangledown \int_{S_{tip}} \Phi_{samp} \mathbf{M}_{tip} \cdot ds - \bigtriangledown \int_{V_{tip}} \Phi_{samp} \Big(\bigtriangledown \cdot \mathbf{M}_{tip} \Big)\, dV \tag{5.3}$$

The first integral is over the surface of the tip, (S_{tip} is the boundary for the volume V_{tip}), where ds is locally normal to the surface. In this work, the tip is modeled as a uniformly magnetized layer coating the surface of a cone. Therefore the second integral in Eq. 5.3 does not contribute to the force on the probe, since $\bigtriangledown \cdot \mathbf{M}_{tip} = 0$. Eq. 5.1 can now be written as;

$$\psi \propto \int_{S_{tip}} \frac{\partial^2 \Phi_{samp}}{\partial z^2} \mathbf{M}_{tip} \cdot ds \tag{5.4}$$

For simulation purposes, the samples, similar to the probe, are considered to be uniformly magnetized. The magnetic potential Φ_{samp} at location $r = (x, y, z)$ for a uniformly magnetized sample is given by (see page 247 in reference [163]);

$$\Phi_{samp}\left(r\right) = \frac{1}{4\pi}\int_{S_{samp}} \frac{\mathbf{M}_{samp}\left(r^{'}\right)\cdot ds^{'}}{\left|r-r^{'}\right|} \tag{5.5}$$

In this integral, $r^{'}$ varies over the boundary S_{samp} of the sample volume, and ds is locally normal to this boundary. Differentiating twice with respect to z gives;

$$\frac{\partial^2\Phi_{samp}\left(r\right)}{\partial z^2} = \int_{S_{samp}} I\left(r-r^{'}\right)\mathbf{M}_{samp}\left(r^{'}\right)\cdot ds^{'} \tag{5.6}$$

where,

$$I(r) = \frac{2z^2-x^2-y^2}{4\pi\left|r\right|^5}$$

Substituting Eq. 5.6 into Eq. 5.4 gives;

$$\psi(r) \propto \int_{S^{''}_{tip}}\left(\int_{S^{'}_{samp}} I\left(r+r^{''}-r^{'}\right)\mathbf{M}_{samp}\left(r^{'}\right)\cdot ds^{'}\right)\mathbf{M}_{tip}\left(r+r^{''}\right)\cdot ds^{''} \tag{5.7}$$

where r is the location of the probe tip in space, $r^{'}$ varies over the surface of the sample, and $r^{''}$ varies over points on the surface of the tip. To create simulated MFM data, Eq. 5.7 is approximated by a summation in Matlab.

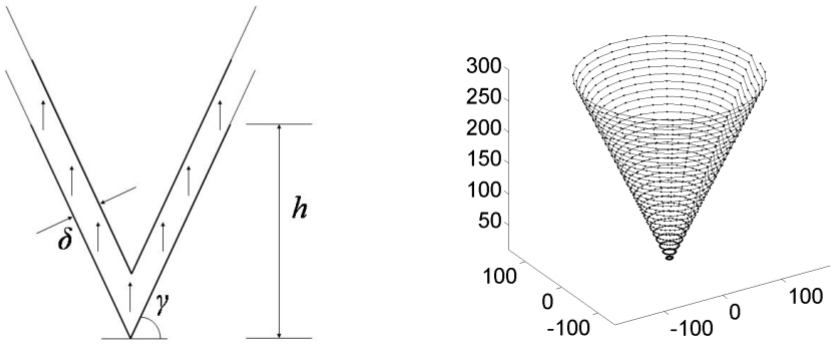

(a) (b)

Figure 5.6: (a) Cross-section of the modeled sample, MFM probe and probe path over the sample with scan height, $z_{scan} = 50$ nm. The probe cone angle is $\gamma = 65°$, the probe height is $h = 300$ nm, and the layer thickness is $\delta = 10$ nm, (b) Points on the tip used to represent the probe surface for the simulations.

The samples are modeled as hemispheres centered at the origin and symmetric about the z axis. The probe is modeled as a uniformly magnetized layer on the surface of a cone. Fig. 5.6(a) illustrates the details of the probe model. Three parameters describe the shape of the probe: angle γ, height h and thickness δ. The values used for these parameters in this simulation are 65^o, 300 nm and 10 nm, respectively. Fig. 5.6(b) illustrates the points chosen to represent the probe. Typically 900 and 1600 points were used in the simulations to represent the probe and sample, respectively. Using this model, a series of simulated MFM images are generated for single domain hemispherical particles with different magnetization directions using MATLAB, as shown in Fig. 5.7. Fig. 5.7(a) represents the path of MFM probe over the hemispherical particle. Fig.5.7(b) - (h) shows MFM response for different magnetization directions of the uniformly magnetized hemispheres from, out-of-plane (Fig. 5.7(b)) to in-plane direction (Fig. 5.7(h)) in steps of 15°.

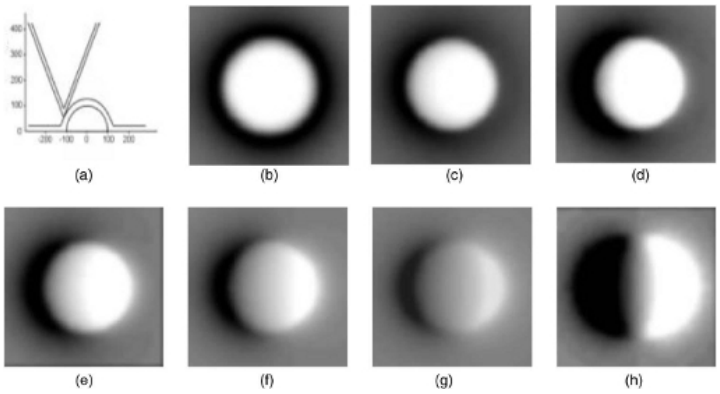

Figure 5.7: MFM simulation results for homogeneously magnetized hemispheres. (a) Cross-section of the MFM tip - sample path for 200 nm diameter particle; (b) - (h) are the simulated MFM images for out-of-plane (Fig. b) to in-plane magnetization (Fig. h) for the hemispheres, shown in steps of 15° change in the magnetization direction.

5.3.4 Magnetic state of Co and Fe nanoarrays

Figures 5.8(a) and (b) show the AFM and the corresponding zero-field MFM images, respectively, of the as-prepared Co nanoparticles. The magnetic information in the MFM images (Fig. 5.8(b)) is represented by the bright and dark contrast. As has been shown previously by a number of researchers, single domains are characterized by a symmetrical dark-white dipolar contrast for in-plane orientation (0° as measured from the surface of the substrate) (see Fig. 5.7(h)), or by a uniform center and oppositely contrasted periphery for out-of-plane orientation of the magnetization (90° as measured from the surface of the substrate) as shown in Fig. 5.7(b). However, if the magnetization direction rotates by 180°, the contrast in the MFM images will be reversed (bright region will become dark and vice-versa). Figs. 5.9(a-c) show the magnified images of the typical MFM contrast observed from different particles, marked by arrows 1 (50 nm particle), 2 (78 nm particle) and 3 (115 nm particle)) in Fig. 5.8(b). While particles marked by 1 and 3 in Fig. 5.9(a) and (c) are consistent with in-plane and out-of-plane orientation of single domain magnets, particle 3 is consistent with a magnetization direction at 45° to the substrate surface. The

assignment of magnetization angle was based on simulations of the tip-sample interactions presented in Sec. 5.3.3. Analysis of all particles within the size range of 30 - 160 nm in Fig. 5.8(b), and up to 180 nm in thicker films indicated MFM contrast similar to that shown in Fig. 5.7(b-h). This suggests that the particles are single domain with the magnetization direction lying between in-plane and out-of-plane directions. Figure 5.11(a) shows the particle size-distribution combined with the size-dependent magnetization directions for all particles, derived from the above analysis. The particles up to 75 nm diameter have their magnetization between $0-45^{\circ}$ and larger particles between $45-90^{\circ}$, as indicated in Fig. 5.11(a). The uncertainty in assigning the magnetization direction came primarily from the comparison of the diffuse contrast in the experimental data, and from the comparison of a true hemisphere in simulations (contact angle 90°) with an approximate hemisphere in the experiment (contact angle $104 \pm 22^{\circ}$). The typical MFM contrast for the larger (>180 nm) multi-domain particles is shown in Fig. 5.9(d). Importantly, no evidence for vortex states, which consist of a dark center and dark edges as shown in Fig. 5.9(e) [5], was found for any particle..

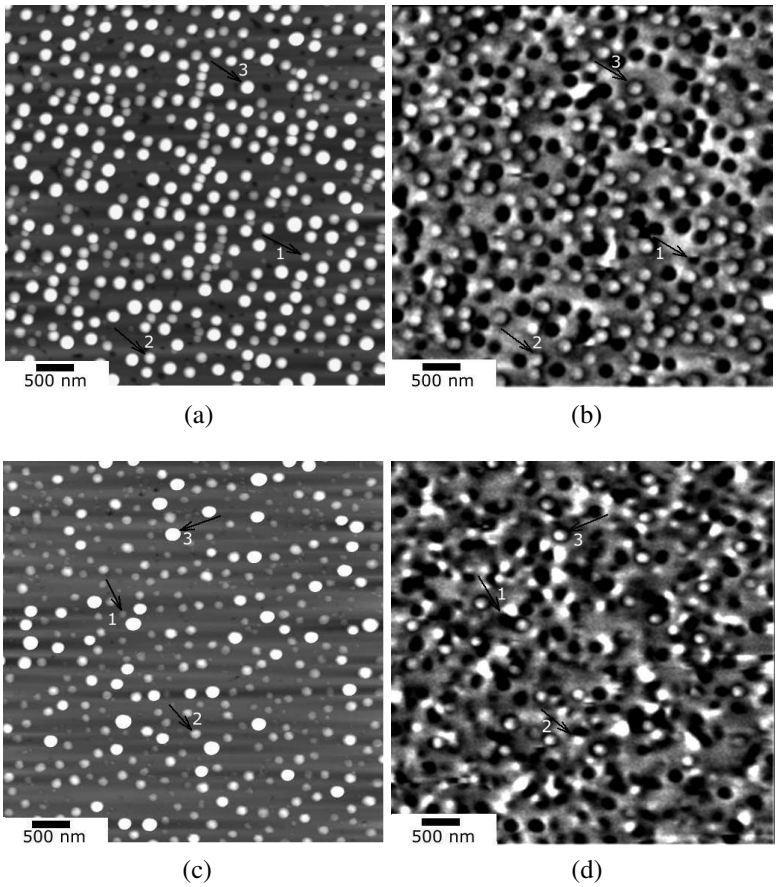

Figure 5.8: AFM and MFM images of as-prepared (a-b) and annealed (c-d) Co particles acquired under zero field condition. Nanoparticles identified by # 1, 2 and 3 in figs. (a) and (b) represent in-plane, near 45^o and out-of-plane magnetization directions, respectively. Nanoparticles identified by #1 and 2 in figs. (c) and (d) represent in-plane, while # 3 represents out-of-plane magnetization direction.

The AFM, and the corresponding zero-field MFM, measurements on the annealed arrays of Co nanoparticles are shown in Fig. 5.8(c) and (d), respectively. In Fig. 5.8(d), the arrows 1 (for 35 nm diameter) and 2 (for 70 nm diameter) indicate particles with in-plane magnetization, whereas arrow 3 (for 125 nm diameter) represents a particle with out-of-plane magnetization. In Fig. 5.11(b) the size ranges for particles with magnetization directions between $0-45^\circ$ (up to 115 nm diameter) and $45-90^\circ$ are shown. Compared to the as-prepared arrays (Fig. 5.11(a)), the annealed arrays show that even much larger particles

(30 - 115 nm compared to 30 - 75 nm for the as-prepared) have preferential in-plane orientation (magnetization direction $\leq 45^{\circ}$). Once again, no evidence for vortex states was found.

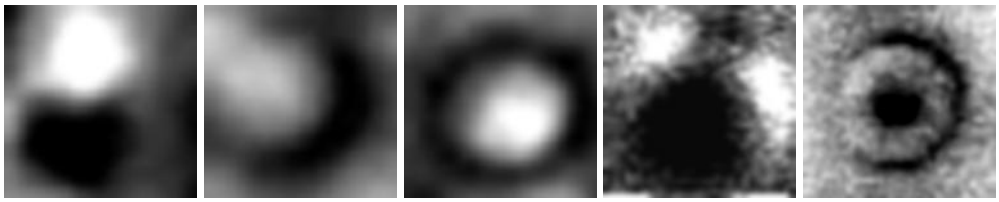

(a) (b) (c) (d) (e)

Figure 5.9: High magnification simulated MFM images for: (a) in-plane, (b) near 45°, and (c) out-of-plane magnetization. Fig. (d) shows MFM contrast for multi-domain particles (larger than 180 nm in diameter), and (e) for vortex state in a circular dot of Co (taken from Fig. 6B of ref.[5]).

Similar to Co, the orientation of magnetization of Fe nanoparticle arrays on SiO_2 substrate was analyzed . Figure 5.10 shows the AFM (Fig. 5.10(a)) and the corresponding MFM (Fig. 5.10(b)) images of a region from the Fe nanoparticle array. The 30 nm, 55 nm and 85 nm diameter particles, indicated by numbers 1, 2 and 3 in the AFM and corresponding MFM images, show magnetization directions at 0°, 45° and 90° with respect to the substrate plane, respectively. After assignment of magnetization directions, the particles were divided into two regions: a) preferentially in-plane ($0-45^{\circ}$ for particles $\leq$ 55 nm) and, b) preferentially out-of-plane ($45-90^{\circ}$ for larger particles), as shown in Fig. 5.11(c). The Fe nanoparticles were SD until approximately 150 nm diameter and multi-domain thereafter; with no evidence for vortex state.

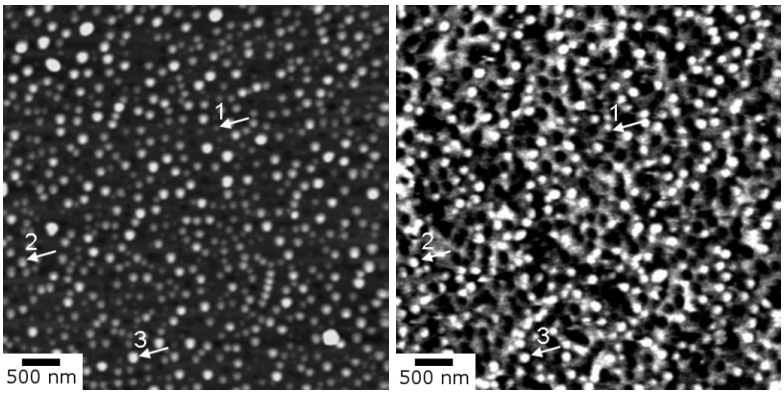

(a) (b)

Figure 5.10: (a) AFM from a region of the arrays showing Fe nanoparticles. (b) Zero applied field MFM images from the AFM region shown in (a). Particles identified by # 1, 2 and 3 (in figs. a and b) correspond to 30 nm, 55 nm and 85 nm size diameters, respectively, and their MFM contrast corresponds to magnetization directions along 0^o, 45^o and 90^o , respectively.

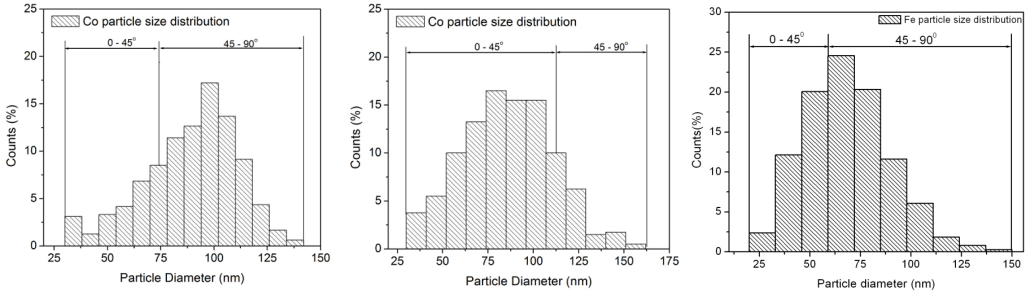

(a) (b) (c)

Figure 5.11: Size distribution of Co and Fe arrays and the corresponding regimes showing experimentally measured magnetization direction with respect to the substrate for as-prepared Co (Fig. a), annealed Co (Fig. b) and as-prepared Fe (Fig. c) with magnetization directions along $0-45^\circ$ and $45-90^\circ$.

5.4 Discussion

The magnetic states of Co and Fe arrays processed by ns laser pulses were either single domain with size dependent magnetization direction or multi-domain. While the experimentally observed single domain size regime (Co$\sim$180 nm and Fe$\sim$150 nm) is large compared to theoretical calculations (Co$\sim$60 nm and Fe$\sim$20 nm) [77, 13], it is not inconsistent with other reported experimental single domain sizes (*e.g.* elliptically shaped Co islands [88, 164, 165]). This discrepancy is primarily due to the fact that the calculations for single domain are fairly approximate and assumes a single crystal [13, 166, 167]. The present experimental condition is different because the particles are polycrystalline and the grains are crystallographically oriented in random directions, coupled by magnetic exchange interactions. This is equivalent to introducing some kind of random anisotropy that lowers the effective magnetocrystalline anisotropy, which increases the domain size compared to single crystal particles. *Importantly, apart from single and multi-domain magnetic states, there is no evidence for vortex magnetic states in the experiments on the near hemispherical nanoparticles*. This is an important difference, given that micromagnetic calculations for unstrained polycrystalline hemispheres predict vortex states in the size regimes of the present experiments [168, 169]. Obviously further work is needed to resolve these issues.

To verify the observation of size-dependent magnetic behavior of these nanomagnets, magnetic hysteresis loop measurement was performed. The hysteresis measurements at room temperature, using the PPMS, for the magnetic field parallel and perpendicular to the substrate plane ($M-H$ curves) are presented in Fig. 5.12(a) for the as-prepared Co nanoarrays with similar microstructures as in Fig. 5.1(b). The solid lines represent the data for magnetic field applied in-plane and the dashed lines for the field perpendicular (out-of-plane) to the plane. The overall characteristics of the $M-H$ curves in both cases were similar, confirming that particles with in-plane as well as out-of-plane magnetization were present. The absence of sharp jumps in the hysteresis curve also implied that there was no substantial contribution from vortex magnetic states in these nanoparticles [168].

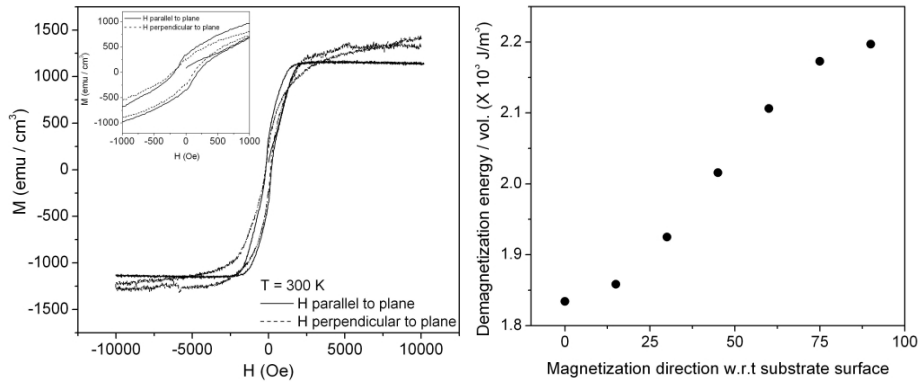

(a) (b)

Figure 5.12: Parallel (solid line) and perpendicular (dashed line) hysteresis curves for as-prepared Co arrays (initial film thickness of 3.2 nm) with particle size distribution similar to Fig. 5.1(b). Inset shows a blow-up of the same hysteresis plot in the range of -1000 to 1000 Oe, (b) Calculated demagnetization energy per unit volume for uniformly magnetized hemispheres oriented along different directions.

To understand the size dependent magnetization, various magnetic energy contributions for these granular nanomagnets were estimated. In this analysis, any anisotropy contribution related to the interface was neglected because the ratio of surface to volume atoms for these particles is small. The total energy per unit volume (E_T) of the arrays includes: the dipolar interparticle interaction energy (E_{Dip}), the shape dependent demagnetization energy (E_{DM}), magnetocrystalline anisotropy energy (E_{MA}), and magnetoelastic anisotropy or magnetostrictive energy (E_{MS});

$$E_T = E_{Dip} + E_{DM} + E_{MA} + E_{MS} \tag{5.8}$$

The dipole-dipole interaction energy per unit volume (E_{Dip}) was calculated between two identical uniformly magnetized hemispheres using the following expression;

$$E_{Dip} = \frac{\mu_0}{4\pi V}\left[\frac{\mu_1 \cdot \mu_2}{r^3} - 3\frac{(\mu_1 \cdot \mathbf{r})(\mu_2 \cdot \mathbf{r})}{r^5}\right] \tag{5.9}$$

where r is the relative distance between the dipoles with magnetic moments μ_i, which is related to the saturation magnetization (M_0) by; $\mu_1 = \mu_2 = M_0 V$, where V is the particle volume [87]. The maximum value of E_{Dip} for two identical single domain Co hemispherical particles of average diameter 88 nm, separated by 290 nm, was estimated to be 8 J/m^3 ($M_0 = 1400\,Gauss$ [93] and $\mu_0 = 4\pi \cdot 10^{-7}\,Wb/A \cdot m$) when both the particles are magnetized out-of-plane; the corresponding energy for the in-plane magnetization of both particles was 17 J/m^3.

The demagnetization energy per unit volume (E_{DM}) as a function of magnetization direction (β, w.r.t substrate plane) was estimated for hemispherical particles (contact angle 90^o), using the approach outlined in ref. [89]. The method assumes that the particles are single domain homogeneously magnetized hemispheres. The calculation was performed by first evaluating the magnetic scalar potential (Φ_M), using general spherical harmonics (Y_{lm}). The final expression for the hemispherical demagnetization energy per unit volume was obtained as;

$$E_{DM} = \mu_0 M_0^2 \left(100 - 9\cos 2\beta\right)/768 \tag{5.10}$$

Fig. 5.12(b) shows the plot of E_{DM} for Co magnets with different magnetization directions, measured with respect to the substrate plane, for the uniformly magnetized hemispheres. It showed that in the case of Co, the out-of-plane magnetized state is higher in energy by $3.62 \times 10^2\,J/m^3$ compared to the in-plane state with an energy of $1.8 \times 10^3\,J/m^3$. This result is consistent with the shape anisotropy favoring magnetization along the longer effective dimension, which is the truncation plane of the hemisphere in the present case (aspect ratio $\sim$1.7). Given the small difference in aspect ratio between a hemisphere (contact angle 90^o) and the experimentally observed nanoparticles (contact angle of 104^o for Co), the general trend of Fig. 5.12(b) is expected to be valid for the nanoparticles under consideration.

The magnitude of magnetocrystalline anisotropy energy E_{MA} depends on the anisotropy constants (K_1 and K_2) of the crystal structure. For polycrystalline cubic Co with n number

of grains, E_{MA} per unit volume can be written in the following form [77];

$$E_{MA} = \frac{1}{n}\sum_{i=1}^{n} K_1 \left[\frac{\sin^4(\alpha_i-\beta)\cdot\sin^2 2\phi}{4} + \cos^2(\alpha_i-\beta)\cdot\sin^2(\alpha_i-\beta)\right]$$

$$+\frac{1}{n}\sum_{i=1}^{n}\frac{K_2\sin^2 2\phi\cdot\sin^2 2(\alpha_i-\beta)}{16} \tag{5.11}$$

where α_i is the angle between the easy axis of the i^{th} grain with the substrate plane, β is the magnetization direction of the particle w.r.t. the substrate plane and ϕ is the azimuthal angle. Constants K_1 and K_2 for cubic Co [170] are $-2.3\times10^4\,J/m^3$ and $-4.31\times10^4\,J/m^3$, respectively . The approximate magnitude of E_{MA} was obtained by assuming $\phi = 0^\circ$. This reduces Eq. 5.11 to;

$$E_{MA} = \frac{K_1}{4n}\sum_{i=1}^{n}\sin^2\left[2(\alpha_i-\beta)\right] \tag{5.12}$$

The order of magnitude for E_{MA} for Co particles, estimated using the experimentally observed number of grains (n) and a range of values for α_i ($-\pi/2$ to $+\pi/2$) in Eq. 5.12, is $\sim 10^3\,J/m^3$, which corresponds to the maximum energy required to orient the magnetization away from the easy axis [88]. However, the true crystalline anisotropy contribution is dependent on the actual microstructure. For example, particles made of single grain will have the highest contribution, whereas randomly oriented multiple grains will have much smaller contribution [88]. In the present case, nanoparticles > 40 nm are typically multi-grained with random crystallographic orientations (Fig. 5.13). Therefore, the magnetocrystalline anisotropy contribution will be significantly lower for these particles.

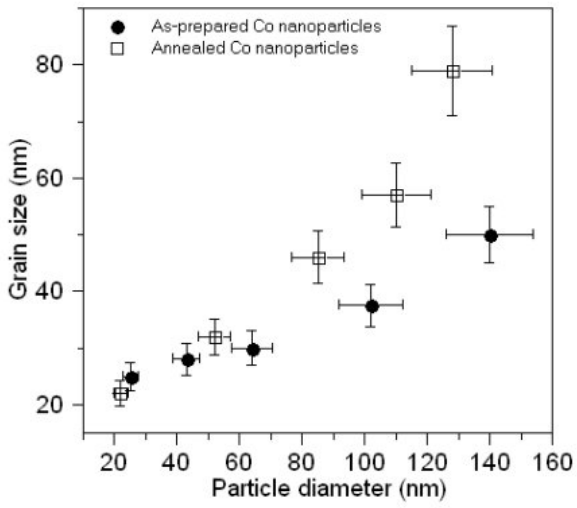

Figure 5.13: Comparison of grain size with particle size for the as-prepared (closed circles) and annealed Co nanoparticles (open squares).

Finally, the magnetostriction energy contribution E_{MS} arises from the coupling of strain to magnetization via the magnetostriction constants [90, 91]. The order of magnitude estimate of E_{MS} for cubic Co crystal was made by using the following relation [92];

$$E_{MS} = (3/2)\lambda\varepsilon(c_{11} - c_{12})[1 + (2c_{12}/c_{11})]cos^2\beta \tag{5.13}$$

where λ is the polycrystalline magnetostriction constant, ε is the thermal strain, c_{11} and c_{12} are the elastic stiffness constants and β is the direction of magnetization. Under the processing conditions, the strain on the nanoparticles arises from the difference in thermal expansion coefficients of the Co ($\sim 13 \times 10^{-6} K^{-1}$) and the SiO_2 substrate ($\sim 0.55 \times 10^{-6} K^{-1}$) during rapid thermal processing. The strain is expected to be tensile since the thermal expansion coefficient of the substrate is smaller than that of the metal. The upper limit of E_{MS} for Co was estimated using the upper limit of the thermally-induced biaxial strain ($\varepsilon_{Co} \sim 0.026$) and the maximum temperature difference achieved during processing (melting point of Co (1495^{o}C) to room temperature). For cubic Co [90], λ is -15×10^{-6},

c_{11} and c_{12} are $2.25 \times 10^{11} J/m^3$ and $1.6 \times 10^{11} J/m^3$, respectively [171]. The maximum estimated value for $E_{MS} \sim 10^5 J/m^3$ for Co, which, appears to be the highest energy contribution in this problem.

The same energy analysis was also performed for Fe nanomagnets. For Fe arrays, the dipolar interaction energy (E_{Dip}) for such large ($\sim$320 nm) interparticle spacings are minimal (using Eq. 5.9 and $M_0 = 1700\,Gauss$ [93]), of the order of $\sim 10 J/m^3$. The magnetocrystalline anisotropy (E_{MA}), will also be significantly low because of the polycrystalline behavior of Fe nanoparticles (TEM image for Fe particles are not shown in this chapter). The shape anisotropy or demagnetization energy (E_{DM}) for the Fe nanoparticles was calculated (using Eq. 5.10) to be of the order of $\sim 10^3 J/m^3$. Finally, the magnetostriction or magnetoelastic anisotropy (E_{MS}) using the magnetostriction coefficient (λ) of -7×10^{-6} for polycrystalline Fe [77], and an estimated upper limit for thermal mismatch strain (ε_{Fe} $\sim$ 0.022) between Fe ($\sim 11 \times 10^{-6} K^{-1}$) and SiO_2, the upper limit for magnetostrictive energy was estimated to be, $E_{MS} \sim 10^5 J/m^3$.

Based on these energy calculations two simple situations can be described:

1. Non-interacting polycrystalline hemispherical particles with no residual strain: In this scenario, the magnetic orientation will be determined primarily by the E_{DM} term in the total energy, aligning the zero-field magnetization along the truncation plane for particles of all sizes.

2. Non-interacting polycrystalline hemispherical particles with large tensile strain along the truncation plane: For large enough strains ($E_{MS} > E_{DM}$), the dominant magnetoelastic energy will determine the magnetization direction of the particles. Because the magnetostriction constant [90, 91] is negative for polycrystalline, soft ferromagnets, like Co, Fe or Ni, the magnetic orientation will be perpendicular to the strain axis.

Based on the above discussion, the experimental results for the multi-grained particles, presented in Figs. 5.11, could be qualitatively understood in the following manner. For

the larger as-prepared particles (Co> 75 nm and Fe> 55 nm) the residual thermal strain from the fast laser processing likely results in $E_{MS} > E_{DM}$, favoring out-of-plane orientation. To qualitatively determine whether this indeed was the case, the Co particle arrays were thermally annealed. As seen from Fig. 5.11(b), the distribution of particles with in-plane versus out-of-plane magnetization changed significantly; particles up to 115 nm now show in-plane orientation, compared to 75 nm for the as-prepared Co arrays (Fig. 5.11(a)). Further, the estimated residual strain (detail analysis is in Chapter 5) that should change the orientation from in-plane to out-of-plane was calculated to be ~ 0.001 [172]. Such a small value, compared to the maximum thermal strain, indicates that even if a substantial fraction of the thermal strain is removed, out-of-plane orientation is possible. The in-plane orientation for the smaller particles suggests that the magnetoelastic energy is comparable or smaller than E_{DM} for these particles. Since there is no size-dependence in E_{DM}, a grain-size dependent strain relaxation mechanism could be responsible for the observed in-plane orientation of the smaller nanoparticles. There is substantial evidence that the rate of stress/strain relaxation in nanostructured materials is a strong function of the grain size. As shown by Shan et. al. [173], Ni nanoparticles undergo size-dependent deformation with smaller particles deforming more easily than larger particles. This behavior was attributed to the energetically favorable surface or grain boundary mediated deformation for very small grains, compared to dislocation-mediated deformation for the larger grains. For grain/surface boundary mediated deformation, the deformation rate is expected to scale with diameter as D^{-4}, implying much faster strain relaxations for the smaller particles. The smaller residual strain in the multi-grained smaller particles in the present case may, therefore, be a result of their smaller grain sizes (Fig. 5.13). Accordingly, the in-plane orientation for the smaller particles appears to be primarily due to shape anisotropy or demagnetization energy.

However, one aspect of the problem remains still unclear. All single grained (single crystal) Co particles ($\sim$40 nm and smaller) show in-plane magnetization (Fig. 5.13). The

TEM analysis on Co particles, based on a few grains, suggest that the crystallographic planes of the grains are randomly oriented with respect to the substrate plane. Now, since the E_{MA} term ($2.3 \times 10^4 J/m^3$) for single crystal particles is larger than all other contributions, when the strain is small, their magnetization should also show random orientation. However, the MFM measurements consistently show an in-plane orientation. A more rigorous study to correlate the microstructure, residual strain, and magnetization direction of these nanomagnets is needed to provide a more quantitative understanding of this unusual size-dependent magnetization.

5.5 Conclusion

A laser-induced self-organization technique was used to create spatially ordered, nearly hemispherical, nanoparticles of Co and Fe on SiO_2 substrates. An extensive study of the magnetization, morphology, and microstructure was performed as a function of particle size for the as-prepared Co and Fe arrays, as well as for the thermally annealed Co arrays, using zero-field MFM, SEM, AFM and TEM studies and magnetic hysteresis measurements. The MFM measurements under zero applied field showed single domain behavior for the smaller particles with size dependent magnetization directions in Co and Fe nanoparticles, and multi-domain behavior for the larger particles. TEM analysis revealed a granular microstructure with the grain size increasing with particle diameter. To interpret the MFM image contrast from the nanoparticles, simulations of the MFM images were performed taking into consideration the MFM tip-hemispherical particle interactions for the uniformly magnetized spheres with different magnetization directions. Histograms of the particle size distribution with the magnetization direction were constructed from these images for the as-prepared and annealed Co arrays, as well as for the as-prepared Fe nanomagnets. In the as-prepared arrays, smaller particles (Co< 75 nm and Fe< 55 nm) showed in-plane magnetization orientation, while larger particles showed out-of-plane orientation. For the

annealed Co sample, in-plane orientation was observed over a larger range of particle sizes, from 30 to 115 nm, compared to 30-75 nm for the as-prepared particles. The origin of this size-dependent magnetization is attributed to a size-dependent relaxation of thermal strain *and* the granular microstructure produced during fast laser thermal processing. These detailed studies of magnetic properties of the laser-induced self-organized nanoparticles with near hemispherical shapes could be important towards understanding the size, shape and process dependent magnetism in the nanoscale. It should be emphasized that while there is substantial evidence for out-of-plane magnetization in epitaxial and/or continuous thin films due to thermal strain [174, 175, 176], such studies for nanoparticles on an amorphous substrate are still lacking.

5.6 Acknowledgments

I would like to thank C. Miller for his significant contribution in the MFM simulation part (sec. 5.3.3) and Dr. A. K. Gangopadhyay for the magnetic hysteresis measurements of Co samples in the PPMS that led to Figure5.12(a).

Chapter 6

Nanoparticles of elements, alloys, and mixtures with in-plane and perpendicular to the plane magnetizations

Summary

Patterned arrays of ferromagnetic hemispherical nanoparticles of elemental Co and Ni, an alloy ($Fe_{50}Co_{50}$), and a phase separated mixture of Cu and Co ($Cu_{50}Co_{50}$) have been synthesized from their ultrathin metal films on SiO_2 substrate by nanosecond laser-induced self-organization. The morphology, nanostructure, and magnetic behavior of the nanoparticle arrays are investigated by a combination of electron, atomic force, and magnetic force microscopy techniques. Transmission electron microscopy investigations reveal a granular polycrystalline nanostructure, with the number of grains inside the nanoparticle increasing with their diameter. Magnetic force measurements suggest that the magnetization direction of Co and Ni nanoparticles are predominantly out-of-plane while those for the $Fe_{50}Co_{50}$ and $Cu_{50}Co_{50}$ are in the plane of the substrate. This difference in behavior is due to the dominating influence of magnetostrictive energy on the magnetization as a result of residual thermal strain following fast laser processing. Since the magnetostriction coefficient is

negative for polycrystalline Co and Ni, and positive for $Fe_{50}Co_{50}$, the tensile residual strain forces the magnetization direction of the negative magnetostriction materials out-of-plane and the positive magnetostriction materials in-plane. In the case of $Cu_{50}Co_{50}$ mixture, the magnetostrictive energy is small because of the low residual strain present in these nanoparticles. As a result, the observed in-plane magnetization is due to shape anisotropy. This demonstrates a cost-effective non-epitaxial technique for the fabrication of patterned arrays of magnetic nanoparticles with tailored magnetization orientations.

6.1 Introduction

As mentioned previously in chapter 5, of prime importance in the field of nanotechnology is the fabrication of patterned nanostructures consisting of discrete nanoparticles whose physical properties (*e.g.* magnetic, semiconducting, or optical) can be reliably controlled by shape, size, and spacing, in conjunction with processing parameters. Arrays of magnetic nanoparticles can be used for many applications, including high density magnetic data storage [21] to non-volatile and high speed magnetic random access memories (MRAM) [32], opto-electronics [141], and biological sensor applications [142]. One of the important challenges in the applications of magnetic nanoparticles is the control of magnetic orientation of each nanoparticle. When the magnetization direction of nanoparticles can be tailored to lie in-plane or perpendicular to the plane, additional advantages are evident. For example, particles with perpendicular to the plane anisotropy enable higher density for the same signal-to-noise ratio [30] and lower the read and write errors [31], compared to particles with in-plane magnetization. In the absence of an external magnetic field, the magnetic moment of a ferromagnetic material aligns spontaneously along a preferred direction. This direction corresponds to the minimum magnetic energy, which in turn is determined by intrinsic material parameters such as magnetocrystalline anisotropy, as well as extrinsic parameters such as shape, size, interfacial strain. Therefore, achieving desired magnetic orientation and switching behavior, requires control of magnetic energy through the choice of intrinsic and extrinsic material properties. For instance, epitaxial thin film growth technique can be used to synthesize single crystal magnetic nanodots, where the magnetocrystalline anisotropy uniquely determines the magnetization direction [177].

This chapter demonstrates magnetic orientation control in polycrystalline nanoparticles through non-epitaxial means. The ordered magnetic nanoparticle arrays were synthesized with the magnetization direction tailored either in-plane or perpendicular to the plane. The magnetic nanoparticle arrays were produced on amorphous SiO_2 surfaces by nanosecond (ns) laser-induced self organization of nanometer thick ferromagnetic metal films, as de-

scribed in the previous chapters. As shown in chapter 5, the single-domain Co [6] and Fe nanoparticles [99] showed particle size-dependent magnetic anisotropy behavior. A significant contribution to this anisotropy came from extrinsic mechanisms. While the polycrystalline nature of the larger nanoparticles (multiple grains) reduced the contribution of magnetocrystalline anisotropy, the residual thermal mismatch strain made a large contribution to the magnetic energy via coupling of the strain to the magnetostriction coefficient. In this chapter, we show how exploiting these process dependent parameters, the magnetization directions of the nanoparticles can be tailored to lie in-plane or perpendicular to the substrate plane. Elemental ferromagnets (Ni, and Co), an alloy ($Fe_{50}Co_{50}$), and a composite nanomaterial ($Cu_{50}Co_{50}$, made of phase separated magnetic Co and non-magnetic Cu) were selected for their different signs of magnetostriction coefficient and magnitude of thermal expansion coefficients. The elemental ferromagnets have negative magnetostriction coefficient (λ_S) (Co, λ_S= -30 ppm and Ni, λ_S = -34 ppm) and the alloy, $Fe_{50}Co_{50}$, has positive magnetostriction coefficient (λ_S = +84 ppm) [77, 178, 179]; the quoted values are for randomly oriented polycrystalline materials. The ensuing investigations of magnetic properties showed that the single-domain Co nanoparticles have preferential perpendicular to the plane (out-of-plane) orientation, while those of $Fe_{50}Co_{50}$ and $Cu_{50}Co_{50}$ in-plane orientations. The reason for this difference was attributed to the coupling of residual thermal strain (tensile), generated on the nanoparticles by the substrate during rapid thermal processing, to the magnetostriction. The residual tensile strain contributed to a high value of the magnetostrictive energy that favored out-of plane orientation of the magnetization for the negative magnetostriction materials (Co and Ni), and in-plane orientation for positive magnetostriction material ($Fe_{50}Co_{50}$). A much lower strain in the nanoparticles of $Cu_{50}Co_{50}$ due to chemical phase separation into very fine grains, allowed the shape anisotropy to dominate, favoring in-plane orientation.

6.2 Experimental details

A thin film of Co ($\sim$ 4 nm) was deposited using electron beam evaporation (e-beam), while Ni ($\sim$ 5 nm), $Fe_{50}Co_{50}$ ($\sim$ 4 nm) and $Cu_{50}Co_{50}$ ($\sim$ 6.5 nm) films were deposited using pulsed laser deposition (PLD) technique on commercially available optically smooth SiO_2/Si(100) substrates, under ultra high vacuum ($\sim 1 \times 10^{-8}$ torr). The ingots for PLD used for FeCo alloy and CuCo mixture were made by repeated arc-melting of stoichiometric mixtures of elements (4N purity) in a water-cooled copper hearth under high purity TiZr-gettered argon atmosphere. The films were irradiated with a Nd:YAG pulsed laser beam as described in the previous chapter. Two types of laser irradiation experiments were performed. For the case of Ni and FeCo, a spatially uniform single beam was incident perpendicular to the substrate surface to produce nanoparticle arrays by spinodal dewetting [1, 150, 153]. For Co and CuCo, two beam laser-interference irradiation was performed to produce 1-dimensional ordered nanoparticle arrays [34].The resulting nanoparticle arrays were characterized by SEM, TEM, AFM, and MFM techniques, as described in chapter 5.

Finite element simulations were performed to model the thermal relaxation of a single hemispherical nanoparticle with diameters ranging from 20 - 100 nm diameter, placed on a 400 nm thick SiO_2 substrate. This was accomplished using the COMSOL software package for a 2-D axi-symmetric geometry, where the particle is perfectly adhered to the substrate. The model was set to be stress-free at the melting point of the nanoparticle, and the stresses and strains present from thermal contraction from the melting temperature to 298 K were determined. The substrate was assumed to be elastic, and the particle was modeled as both a purely elastic and elastic-perfectly plastic solid. The yield strength, σ_y, of annealed pure Co, 400 MPa, and pure Ni, 300 MPa, was determined by converting large depth hardness data by means of the tabor relation, Hardness = $3\sigma_y$ [180, 181, 182]. The average stresses within the particle were converted to elastic strain by Hooke's law resulting in two tensile in-plane principal elastic strains.

6.3 Results

The nanostructural studies of the individual particles of Co, Ni and $Fe_{50}Co_{50}$ are shown in Fig.6.1. Figure6.1(a) is the bright field (BF) TEM micrograph of Co nanoparticles. Detailed nanostructural analysis for Co particles, as explained in chapter 5 [6], revealed a granular nanostructure with random orientation of the grains inside the nanoparticles. The number of grains increased with increasing nanoparticle size from 1 grain (*i.e.* single crystal) for the smaller particles (< 40 nm) to 20-30 grains for the bigger particles (~ 120 nm), with small statistical variation when different similar size particles were compared. Figure6.1(b) is the BF TEM image for the array of Ni nanoparticles. These also indicate a granular nanostructure with random orientation of the grains. Similar to Co, the very small Ni particles (~ 15 nm) are single grained while the bigger particles have multiple grains (*e.g.*, ~ 40 nm particle is made of about 20 grains). The TEM image of $Fe_{50}Co_{50}$ nanoparticles [shown in Fig.6.1(c)] also showed similar granular behavior. The main difference was the large statistical variation in the number of grains from particle to particle, even when the size was similar (*e.g.*, a small fraction of ~ 150 nm size particles had only 2-5 grains, while the majority had more than 15 grains).

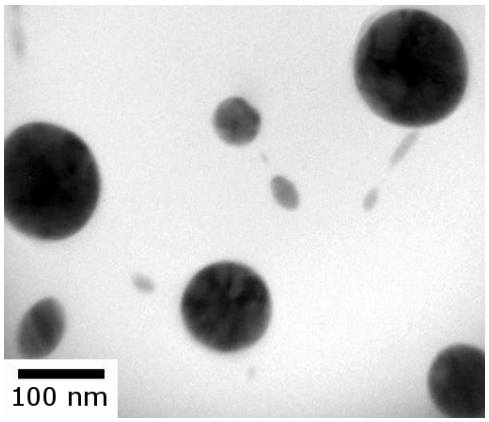

(a)

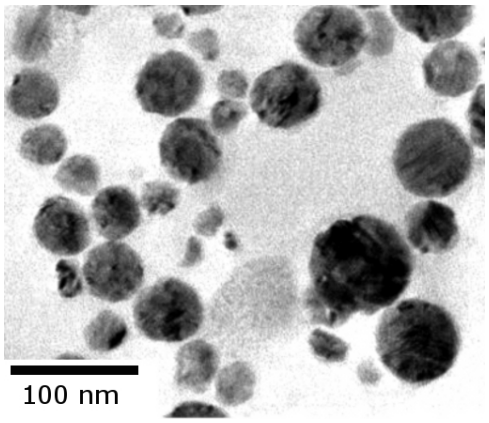

(b)

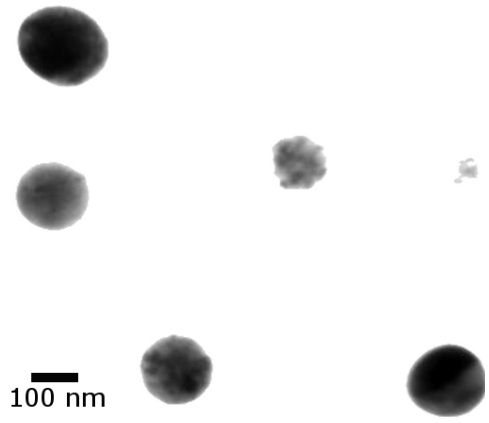

(c)

Figure 6.1: Representative bright field TEM micrographs for nanoparticle arrays synthesized by the laser-induced self-organization; (a) Co nanoparticles, (b) Ni nanoparticles, and (c) $Fe_{50}Co_{50}$ nanoparticles. The contrast within each nanoparticle arises from random crystallographic orientation of multiple grains. Such images were used to generate statistics on the number of grains as a function of nanoparticle size.

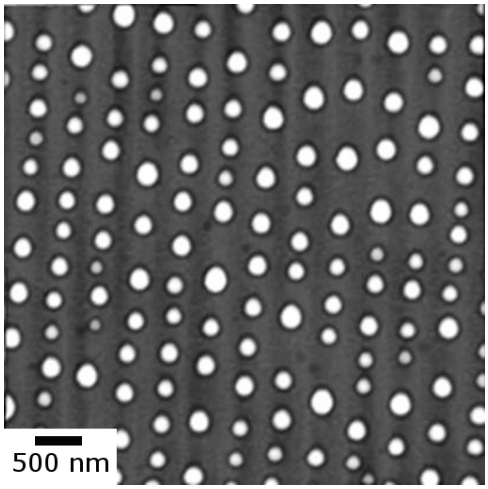

(a)

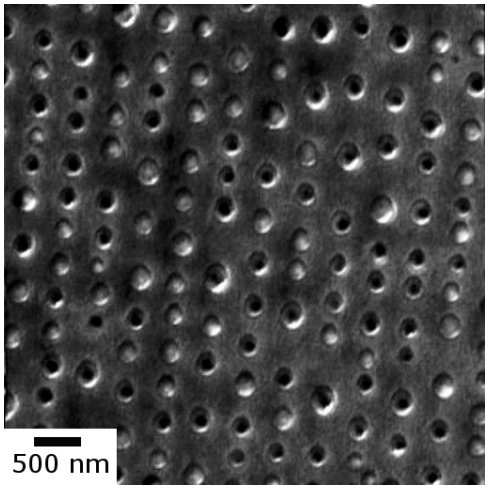

(b)

Figure 6.2: AFM (a) and zero field MFM (b) images of one dimensional patterned Co nanoparticles produced by 2-beam pulsed laser interference irradiation of a 4 nm Co film.

Figure 6.2 shows the AFM (6.2(a)) and zero-field MFM (6.2(b)) images of an array of Co nanoparticles produced by two beam irradiation. The separation between the rows of particles is ~ 400 nm, which is consistent with the separation of the interference fringes from the two beams. The regular 1-D pattern of the nanoparticles along the lines is clearly evident. A 2-D pattern can also be formed using three beam irradiation [104]. The average

particle diameter was measured to be 110 ± 34 nm. The corresponding MFM image in Figure 6.2(b) shows that the image contrast of the particles, is either uniformly dark with a bright periphery or uniformly bright with a dark periphery. When compared with the simulated MFM image contrast of single domain particles oriented along different directions (Fig.6.5), it is clear that all particles in Fig.6.2(b) are single domain and have their magnetization orientation perpendicular to the substrate plane; the exactly opposite image contrast of the two groups is due to their magnetization pointing either up or down (see chapter 4 for detailed analysis).

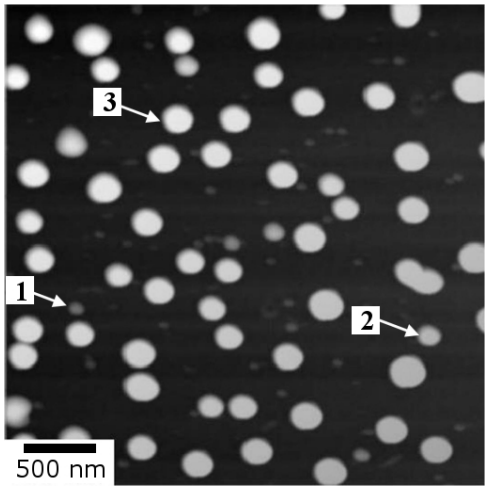

(a)

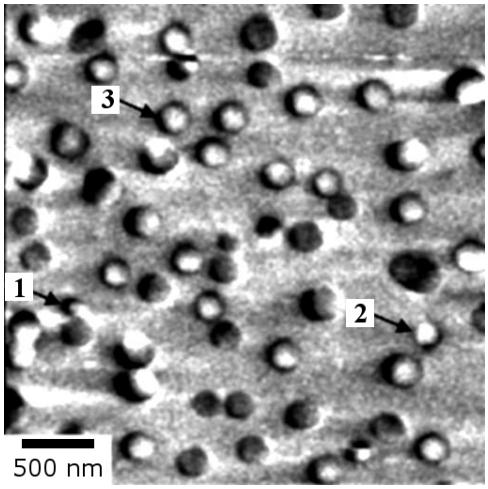

(b)

Figure 6.3: AFM (a) and zero field MFM (b) images of Ni nanoparticles produced by single beam pulsed laser irradiation of a 5 nm Ni film. The nanoparticles marked as #s 1, 2, and 3 in the AFM image (Fig. (a)) are 75 nm, 135 nm and 200 nm diameter, respectively. The corresponding MFM image [Fig. (b)] indicates the magnetization directions with respect to the substrate plane at 0^o, 45^o and 90^o, respectively.

The AFM and MFM images for the Ni array produced by single beam irradiation, is shown in Figure6.3(a) and 6.3(b), respectively. Due to self-organization by spinodal dewetting, the particles have a characteristic interparticle spacing ($\sim$615 nm) and a fairly narrow particle size distribution (176 ± 37 nm). Compared to the two beam irradiation, the spatial distribution of these particles do not follow any pattern, however. Similar to Co, the

contrast in the MFM image [Fig.6.3(b)] indicates that almost all particles (similar in size to that marked as # 3) have their magnetization perpendicular to the substrate plane, either up or down. A few particles (*e.g.* marked as 2 in Figure6.3(a)) have their magnetization at an angle $< 90^o$ to the plane; only the smallest particle (marked as 1) of about 75 nm in diameter is oriented at a small angle to the plane. The nanoparticles have a multi-grained microstructure, but are single domain up to about 220 nm diameter, which is slightly larger than the previously reported value of $\sim$180 nm for spherical single grain Ni nanoparticle [183].

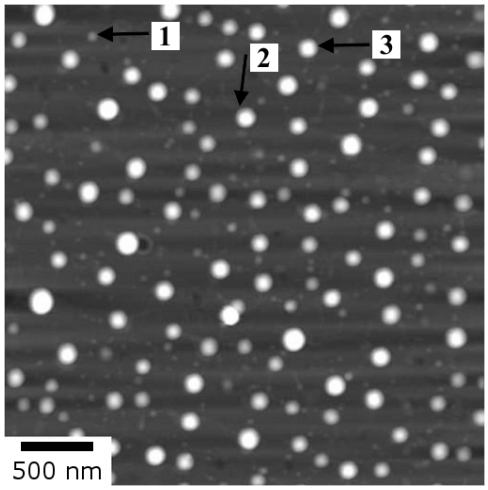

(a)

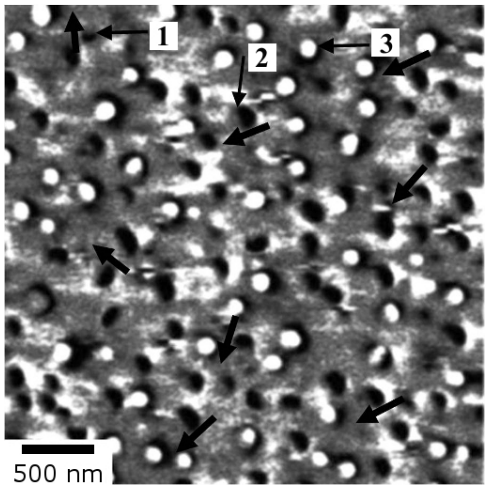

(b)

Figure 6.4: AFM (a) and the zero-field MFM (b) images of $Fe_{50}Co_{50}$ nanomagnets produced from a 4 nm film by pulsed laser irradiation. The nanoparticles indicated as #s 1 and 2 in the AFM image (Fig. (a)) are 50 nm and 150 nm diameters; the corresponding MFM image (Fig. (b)) indicates that both have magnetization direction in the substrate plane (0^o), while another 150 nm diameter particle (# 3) is aligned at $\sim 45^o$ to the substrate. The bold arrows in Fig. (b) indicate the in-plane random orientations of the other nanoparticles.

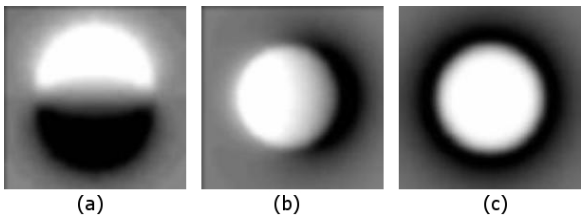

Figure 6.5: The simulated contrast in the MFM images of a single domain ferromagnetic particle with (a) in-plane (0^o), (b) at an angle of 45^o and (c) perpendicular to the plane (90^o) (taken from chapter 4 [6]).

The AFM and the MFM images on an array of $Fe_{50}Co_{50}$ nanoparticles, produced by single beam irradiation, are shown in Figures6.4(a) and (b), respectively. The average particle diameter is 113 ± 32 nm with about $\sim$580 nm separation. The particles with diameters 50 nm and 150 nm, indicated as 1 and 2 in the AFM and MFM images, show in-plane (0^o) magnetization. In stark contrast to Co and Ni nanoparticles, most of the $Fe_{50}Co_{50}$ nanoparticles (around 70 %) show in-plane magnetization while the rest (*e.g.* number 3) are at a small angle ($\leq 45^o$) to the plane. These multigrain particles remain single domain up to about 175 nm in diameter. These results clearly show a difference in the orientation of the magnetization of the nanoparticles with respect to the substrate plane when the magnetostriction coefficient changes sign.

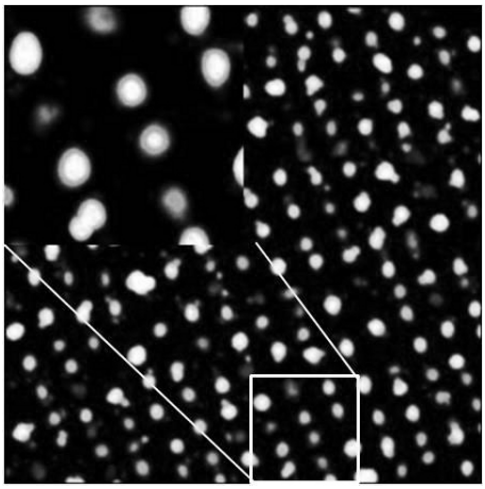

(a)

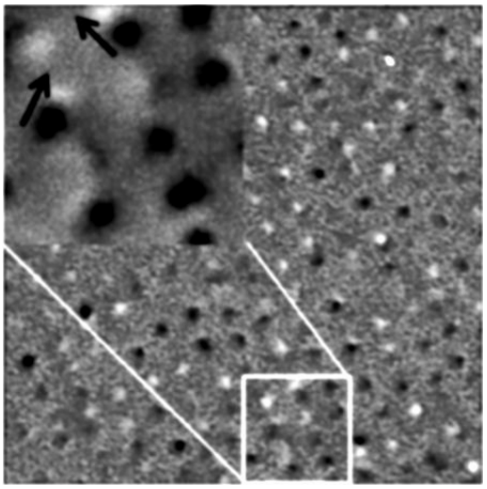

(b)

Figure 6.6: AFM (a) and the corresponding MFM (b) for $Cu_{50}Co_{50}$ nanoparticle showing in-plane magnetization. The size of each micrograph is $5\mu mX\,5\mu m$. The arrows in the inset of image (b) show the direction of in-plane directions. The size of each inset image is $1\mu mX\,1\mu m$

Figure 6.6(a) shows the AFM and corresponding magnetic information for $Cu_{50}Co_{50}$ particles [Fig. 6.6(b)]. The average particle size for $Cu_{50}Co_{50}$ composites was measured to be 121 ± 20 nm in diameter. The separation between the rows of particles is ~ 350 nm, consistent with the separation of the interference fringes from the two beams at 45^o angle. The contact angle was measured to be 97 ± 15^o. The split dark-bright contrast in these particles in Fig. 6.6(a) is consistent with in-plane directions ($\sim 0^o$ with the substrate

plane).

The average in-plane elastic thermal strains determined from the finite element simulations were found to be independent of particle size. This is because the only relevant length scale present in the problem is the ratio of particle diameter to the size of the SiO_2 substrate, which was sufficiently large. The larger of the two average in-plane elastic strains is given in Table6.1, along with the material parameters used in the simulation [184]. Only the average elastic component of strain is reported due to its contribution to the megnetostrictive energy. With no mechanism to relieve internal stresses, the elastic solutions represent an upper bound on the average elastic strains. The average elastic strain is found to be lower for the elastic-perfectly plastic simulations due to the presence of large plastic deformations. The yield strength chosen and the nature of the elastic-perfectly plastic simulations neglects any size, strain hardening and cooling rate affects, which may significantly reduce plastic deformations consequently increasing average stresses and elastic strains within the particle [185, 186]. For this reason, the elastic-plastic simulations are assumed to be a lower bound of the resulting average elastic strain.

Table 6.1: List of material parameters used for finite element simulation and the average in-plane elastic strain values obtained from the simulation . The strain reported is the larger of the in-plane principal strains averaged over the volume of the particle.

Property		SiO_2	Cobalt		Nickel		Co-Fe
Thermal expansion coeff.	$\alpha \times 10^{-6}$	0.55	13		13.4		12.4
Melting temperature	T_m(K)		1768		1728		1748
Young's modulus	E (GPa)	72	209		200		82.7
Poisson's ratio	ν	0.17	0.31		0.31		0.31
Yield strength	σ_y (MPa)	∞	∞	400	∞	250	∞
Avg. in-plane elastic strain	$\varepsilon\left(\times 10^{-4}\right)$		10	3.9	10.5	4.6	24

6.4 Discussion

To understand this difference, various contributions to the magnetic energy of a nanoparticle was estimated. The magnetocrystalline anisotropy, which depends on the crystal structure, is significant only for single crystal or polycrystalline particles with preferred crystallographic orientation of the grains. The anisotropy constants for single crystal Co, Ni, and $Fe_{50}Co_{50}$ are 2.3×10^4, 0.5×10^4 and 4.8×10^4 J/m^3, respectively [77]. For random crystallographic orientation of the grains, such as the case here, the contribution of crystalline anisotropy scales inversely with the number of grains [88], reducing to at least one to two orders of magnitude smaller values when the number of grains exceed about 20 (see Fig.6.7 and [6]). Because of the large interparticle separation (400 to 600 nm), dipolar interaction energy is also small, as will be shown below. The shapes of these nanoparticles are nearly hemispherical as has been determined by the AFM measurements. The estimated contact angles were 104 ± 22^o, 106 ± 26^o, and 103 ± 20^o, for Co, Ni, and $Fe_{50}Co_{50}$, respectively. For the average particle size and separations, using the known saturation magnetizations (1400, 485, and 1922 Gauss for Co, Ni, and $Fe_{50}Co_{50}$, respectively [77]), the demagnetization energy was estimated to be $\sim 1.8 \times 10^3$, $\sim 2.3 \times 10^2$, and $\sim 3.6 \times 10^3$ J/m^3 for Co, Ni, and $Fe_{50}Co_{50}$, respectively [see horizontal lines in Fig.6.7(a-c)]. To estimate the magnetostrictive energy, two approaches were used. A simplistic estimation, as given in chapter 5, considered the difference in the thermal expansion coefficients of the substrate and the metal (13×10^{-6} K^{-1}, 13.4×10^{-6} K^{-1}, and 12.4×10^{-6} K^{-1}, and 0.55×10^{-6} K^{-1}, for Co, Ni, $Fe_{50}Co_{50}$ alloy, and SiO_2, respectively [187]) during cooling from the melting point to room temperature, gave an upper limit of the tensile strain to be ~ 2.5%. The corresponding value for E_{MS} is about 1×10^5 J/m^3, much higher than all other energy contributions in the present case. A more sophisticated calculation, as explained in the previous section, gave the maximum theoretical elastic strain to be 0.1% for both Co and Ni and 0.24% for $Fe_{50}Co$ (see Table6.1). The corresponding values of E_{MS} are 7.7×10^3, 1.1×10^4 and 3.3×10^4 J/m^3 for Co, Ni and $Fe_{50}Co_{50}$ respectively. The estimated magnetostrictive energies (E_{MS}) as a

function of strain (%) for Co, Ni, and $Fe_{50}Co_{50}$, along with the magnetocrystalline energy, E_{MC}, and demagnetization energy, E_{DM}, as a function of number of grains in the nanoparticles are shown in Fig. 6.7.. They clearly show that, E_{MS} dominates over all other energy terms (E_{MC} or E_{DM}), even when a very small amount of strain ($\sim 0.1\%$) is present in these magnetic particles.

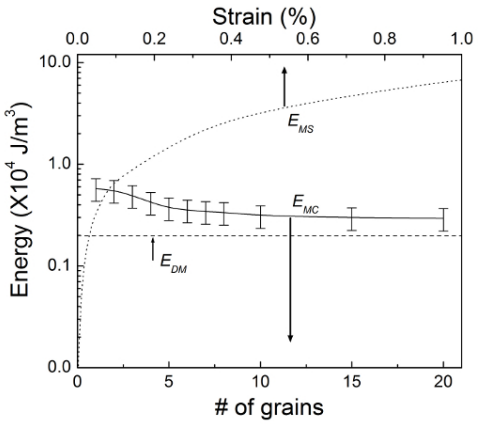

(a)

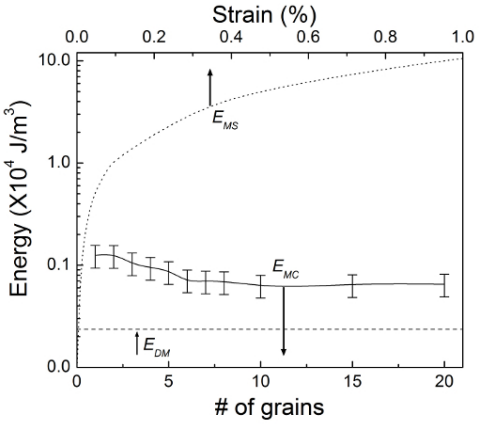

(b)

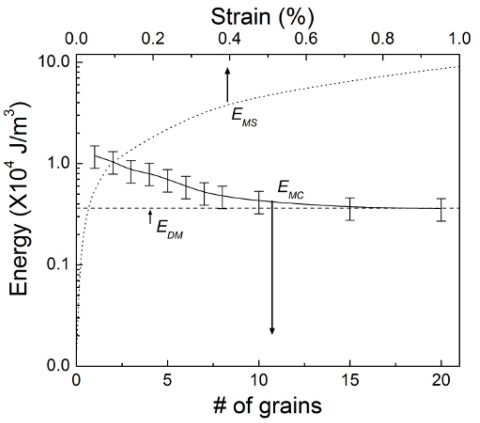

(c)

Figure 6.7: The comparison of different magnetic energies for the three different materials. The magnetocrystalline energy (E_{MC}) is shown as a function of number of grains, and the magnetostrictive energy (E_{MS}) as a function of strain (%). The demagnetization energy (E_{DM}) is also shown. Fig (a) corresponds to Co, Fig. (b) to Ni and, Fig. (c) to $Fe_{50}Co_{50}$. In each of the three cases a small amount of residual strain (~0.1%) is sufficient to make the E_{MS} dominate over E_{MC} and E_{DM}.

With this reasoning, the difference in the behavior of magnetization direction for the nanoparticles of Co and Ni versus $Fe_{50}Co_{50}$ can be explained. For an in-plane tensile strain, the magnetization will be perpendicular to the substrate plane when the λ_S is negative, as is the case for Co and Ni. On the other hand, for positive values of λ_S, the magnetization will be in-plane, as is the case for $Fe_{50}Co_{50}$. One point needs to be clarified, however. A fairly significant number of $Fe_{50}Co_{50}$ nanoparticles (about 30%), also show slightly out of plane $(0-45^o)$ magnetization. Interestingly, as mentioned in the previous section, the TEM analysis of $Fe_{50}Co_{50}$ showed large statistical variations in the number of grains for the same diameter nanoparticles. As can be seen from Fig. 6.7, the magnetocrystalline anisotropy contribution cannot be neglected when the number of grains is small. For example, the magnetocrystalline anisotropy energy for $Fe_{50}Co_{50}$for 2 grains was calculated to be $\sim 1 \times 10^4$ J/m^3, compared to an order of magnitude smaller value of $\leq 1 \times 10^3$ J/m^3 for 15 grains (anisotropy constant $K_1 = 4.8 \times 10^4$ J/m^3 [77]). The magnetocrystalline energy, therefore, may compete with the magnetostrictive energy for particles containing smaller number of grains and orient the magnetization from the in-plane direction. The same argument may be applied to the in-plane magnetization of smaller Ni nanoparticles. Moreover, some statistical variation in the amount of strain in particles of the same size may also be partly responsible for the above observations.

The in-plane magnetic behavior of $Cu_{50}Co_{50}$ nanoparticles can also be explained by similar arguments, but with a slightly different strain relaxation mechanism. Since binary phase diagram of Cu-Co system reveals a very small miscibility in each other, each $Cu_{50}Co_{50}$ nanoparticle is expected to be made of phase separated smaller grains of Cu and Co. Although detailed x-ray mapping of the nanoparticles have not been done in this case, such studies for a similar immiscible system, AgCo, showed phase separated Ag and Co grains inside the nanoparticles (chapter 3). Moreover, previous studies of thin films and devitrified CuCo alloys [188] have clearly shown the presence of phase separated Co and

Cu grains in such nanocomposite materials. Under the present processing conditions, it is quite realistic to expect that because of the much lower melting point of Cu (1356 K) compared to Co (1768 K), Co grains will nucleate and grow first from the liquid during cooling . Since they remain in contact with the remaining Cu-rich liquid, they do not experience any strain until the Cu-rich liquid solidifies. Therefore, the temperature window over which the Co grains experience strain is much narrower; room temperature to the melting point of Cu, instead of m.p. of Co. Thereafter, the strain experienced by the Co grains is small, because of two reasons. First, the thermal expansion mismatch between Cu and Co is small (Cu, $\alpha_{th} \sim 16.5 \times 10^{-6} K^{-1}$ and Co, $\alpha_{th} \sim 13 \times 10^{-6} K^{-1}$). Whatever strain now comes form the SiO_2 interface, most likely causes plastic deformation of Cu because of its low elastic limit. The harder Co grains, being embedded in the softer Cu matrix, experience much smaller strain and may also transfer some their strain to the Cu grains. Therefore the magnetostrictive energy is, expected to be much smaller compared to the elemental metals or miscible alloys. The magnetocrystalline is also expected to be small because of the fine grained nanostructure. The shape anisotropy (demagnetizing) is, therefore, expected to dominate and favor in-plane magnetization direction. Clearly, more theoretical and experimental investigations are required to support this argument.

6.5 Conclusion

In conclusion, magnetic nanoparticle arrays of Co, Ni, $Fe_{50}Co_{50}$ and $Cu_{50}Co_{50}$ were synthesized using *ns* laser-induced self-organization from ultrathin films deposited on SiO_2 surfaces. The resulting nanoparticles were hemispherical in shape with polycrystalline nanostructure. An extensive study of the orientation of the magnetization as a function of nanoparticle size was performed using zero-field MFM. This revealed that the single-domain magnetic nanoparticles of Co and Ni were primarily oriented out-of-plane. On the

other hand, nanoparticles of $Fe_{50}Co_{50}$ and $Cu_{50}Co_{50}$ were primarily in-plane. The reason for this difference was attributed to the difference in the sign of magnetostriction coefficients and the magnitude of magnetostrictive energy. Magnetic energy arguments showed that the magnetostrictive energy dominates among all other contributions, when some residual tensile strain is present in the nanoparticles due to the fast cooling process following the ns pulsed laser irradiation. As a result, metals with negative magnetostriction coefficient (Co, and Ni) show out-of-plane magnetization while, positive magnetostriction coefficient materials ($Fe_{50}Co_{50}$) show in-plane magnetization. The in-plane behavior in $Cu_{50}Co_{50}$ composites was explained by small magnetostrictive energy due to the presence of lower strain and finer grain size in these particles. This demonstrates a cost-effective, and non-epitaxial, laser-based processing technique for the production of one- and two-dimensional arrays of magnetic nanoparticles with controlled magnetization directions.

6.6 Acknowledgments

I would also like to acknowledge Dr. Jeremy Strader for his contribution in the theoretical calculation of maximum elastic strain present in the nanoparticles, as presented in Table6.1.

Chapter 7

Summary and future work

7.1 Summary

This chapter summarizes the key findings of this dissertation and also identifies some potential directions for future research based on preliminary results (sec. 7.2). The scientific and technological motivation of this research was presented in the introductory message in chapter 1. Self-organization via dewetting in ultrathin films has received attention because of its potential application as a nanomanufacturing process and also because of the fundamental interplay between energy and dynamics. Practically, dewetting is a simple, low cost, robust and reliable route to create surface nanostructures. It results in a variety of complex structures with ability to control size, shape and spacing. Scientifically, the correlation between the temporal behavior of the free energy of the thin film system with energy loss mechanisms during fluid flow (viscous dissipation) is a fundamental principle underlying spontaneous self-organization. Finally, the use of nanosecond pulsed laser irradiation to initiate and foster the dewetting process is also an important aspect of this work as it allows a systematic exploration of the dewetting morphology evolution, permits exploration of high-melting point materials, introduces intrinsic nanoscale effects that can modify dewetting, and influences the magnetic properties of nanostructures prepared by this process.

The dewetting in thin metal films on inert substrates was observed to follow the spin-

odal dewetting mechanism, and in certain instances, modified by intrinsic thermocapillary forces. A thermodynamic model was developed to understand the characteristics of dewetting in single layer and bilayer metal films. This model is based on the principle of equating the rate of change of free energy to the viscous dissipation during liquid flow. The characteristic length scales of spontaneous dewetting were accurately described by this model. The experimental observations of thickness (h) dependent dewetting length scales (λ) in single layer Ag metal on SiO_2 substrate was correctly explained by the thermodynamic theory, where the length scale showed a parabolic dependence on the initial film thickness ($\lambda \propto h^2$). The model was also successful at explaining the dewetting behavior of Co, which deviated from the classical spinodal case for larger thicknesses. This occured because of the presence of intrinsic thermocapillary forces generated by the nanosecond laser heating process. For bilayers, the theoretical and experimental dewetting study was performed for the immiscible metals Ag and Co on SiO_2 substrates. The length scale behavior was obtained as a function of film thicknesses for both the bilayer configurations, Ag/Co/SiO_2 and Co/Ag/SiO_2, via the thermodynamic model. A substantial difference in length scale with bilayer thickness was seen for the two configurations. The length scale was a non-monotonic function of bilayer thickness for Ag/Co/SiO_2, while it increased monotonically for Co/Ag/SiO_2. This difference could be explained by the difference in the sign and magnitude of the intermolecular forces for the two cases. The experimental observations for both configurations were consistent with the theory. Nanostructure studies were also performed using TEM and x-ray mapping in the SEM for the nanoparticles created by laser processing of bilayer Ag-Co thin films on SiO_2. These revealed that each nanoparticle is a composite of Ag and Co. The ratio of Ag and Co in each nanocomposite, which was calculated by measuring the x-ray counts of both elements, was identical to the individual film thickness in the bilayer.

The morphological evolution during dewetting was studied as a function of film thickness for the case of Ag on SiO_2. In the thickness range of $2 \leq h \leq 20$ nm, the length scale

trend confirmed the spinodal dewetting process. However, the morphology showed bicontinuous structures as an intermediate stage for films $h \leq 9.5$ nm, and regularly sized holes and polygon networks for $11.5 \leq h \leq 20$ nm. This transition in morphology at a specific thickness was correlated to the position of the minima in the free energy curvature. The thickness-dependent free energy contributions came from a long-range attraction, a short range Lennard-Jones type repulsion, and an electrostatic term. The resulting prediction for morphology change for Ag was consistent with experimental observations.

The magnetic properties of hemispherical shaped nanomagnets were investigated for the elemental (Co, Fe, and Ni), alloy ($Fe_{50}Co_{50}$), and a phase mixture ($Cu_{50}Co_{50}$), on SiO_2 substrates. The MFM and hysteresis loop measurement techniques were used to characterize these nanomagnets arrays comprising of 30 - 250 nm diameter nanoparticles. Depending on the particle size, the nanomagnets showed single or multi domain behavior; no evidence for vortex magnetic states was observed in any of these nanomagnets. For the single domain Co, Fe, and Ni nanoparticles, the magnetization showed size-dependent orientations, with the smaller particles aligned in the substrate plane and the bigger particles perpendicular. The size-dependent magnetic behavior was explained by the size-dependent residual thermal strain (tensile), developed during fast laser processing, and the coupling of strain to the negative magnetostriction coefficients of the ferromagnetic elements. A detailed estimate of the various contributions to the magnetic energy revealed that the dominating influence of the magnetostrictive energy controls the magnetization direction of the nanoparticles. This found additional support when the magnetic properties were studied for an array of nanoparticles of a positive magnetostriction coefficient material, $Fe_{50}Co_{50}$, and a phase separated mixture of Co and Cu nanoparticles with very small residual strain, synthesized from a $Cu_{50}Co_{50}$ alloy. Magnetic force measurements revealed in-plane behavior for both $Fe_{50}Co_{50}$ and $Cu_{50}Co_{50}$ nanoparticles. These results clearly show that controlling the interfacial strain during fast laser processing and judicial choice of magnetostrictive properties of materials, the magnetization directions of nanoparticle arrays can be tailored

to lie in specific directions.

7.2 Future work: Magnetic properties in complex shapes

As mentioned in the earlier chapters, the shape is an important factor in magnetism. After studying the magnetic properties of hemispherical nanoparticles, the investigation of magnetism in other shapes (morphologies) such as nanowires and polygons created by rapid laser processing, appeared to be interesting. Here, a summary of some preliminary results obtained for different morphologies, for elemental Co and composite $Co_{40}Ag_{60}$, on SiO_2 substrates, is provided.

7.2.1 Experimental details

Either a thin film of Co ($\sim$ 4 nm), or a bilayer films of Ag ($\sim$ 5 nm) and Co ($\sim$ 7 nm) was evaporated on commercially available optically smooth SiO_2/Si(100) substrates under ultra high vacuum ($\sim 1 \times 10^{-8}$ torr). The thermally grown oxide (SiO_2) layer was 400 nm thick. The deposition of Co and Ag was done by electron beam evaporation and pulsed laser deposition techniques, respectively. To produce one-dimensional ordered array of Co nanowires, the film was exposed to a two-beam laser (wavelength of 266 nm with a pulse length of 9 ns, at a repetition rate of 50 Hz) interference pattern, with an angle of 40^o between the beams. The nanopolygon structures of Co and $Co_{40}Ag_{60}$ were made by irradiating the Co/SiO_2 and Co/Ag/SiO_2 films, respectively, using a spatially uniform single beam, incident perpendicular to the substrate surface. In all these experiments, the energy density of the laser pulses ($\sim$ 60 mJ/cm^2) was chosen to be slightly above the melt threshold. Approximately, 100 laser pulses were required to achieve the pattern with arrays of nanowires or nanopolygon networks.

The resulting morphologies were characterized for topographic and magnetic images, by a tapping mode atomic force microscopy (AFM) and zero-field magnetic force mi-

croscopy (MFM), respectively, using a Digital Instruments Dimension 3000 instrument. A silicon cantilever, coated with a few tens of nm thick CoCr alloy (Asylum Research, ASY), with a scan height of 50 nm, was used in the MFM measurements. To rule out any influence of the MFM-tip on the measurement, MFM was performed in different directions (0^o and 90^o) and at different heights from the samples.

7.2.2 Results and Discussion

7.2.2.1 Co nanowires

Figure 7.1 shows the AFM [Fig. 7.1(a)] and the corresponding zero-field MFM [Fig. 7.1(b)] micrographs of the one-dimensional ordered Co nanowires on SiO_2 substrate, produced by two-beam laser interference irradiation on a Co ($\sim$ 4 nm) film. The spacing between the nanowires was measured to be $\sim$390 nm, which is consistent with the interference angle of 40^o for the two 266 nm laser beams. The length of nanowires was measured to be in the range of 5-20 μm. The average width and height of nanowires were 150 nm and 45 nm, respectively. The contact angle of the nanowire with the substrate was calculated, assuming a cylindrical shape with width and height estimated from AFM, to be 65^o. The magnified AFM and MFM image of a part of the Co nanowire is also shown in the outset of Figures 7.1(a) and (b). The continuous dark and bright contrast in the magnified MFM images along the nanowire indicate that Co breaks up into 250 - 400 nm long domains (SD), with random in-plane magnetization directions. The break-ups appear to be at places where the cross-sectional area (height and width) changes significantly. Such inhomogeneity in shape and formation of defects at these sites, may help domain wall formation and pinning [189]. The shape anisotropy for such Co nanowires is calculated to be 6×10^5 J/m^3 [190], compared to 6.3×10^4 J/m^3 [84] for the magnetocrystalline anisotropy for single crystal cubic Co, which should be further reduced because of the polycrystallinity 7.3. Clearly, the shape anisotropy is dominating over magnetocrystalline anisotropy, favoring magnetization orientation along the long-axis of the wires in the substrate plane. The random

in-plane orientation may be related to the random kinks and bends in the nanowires.

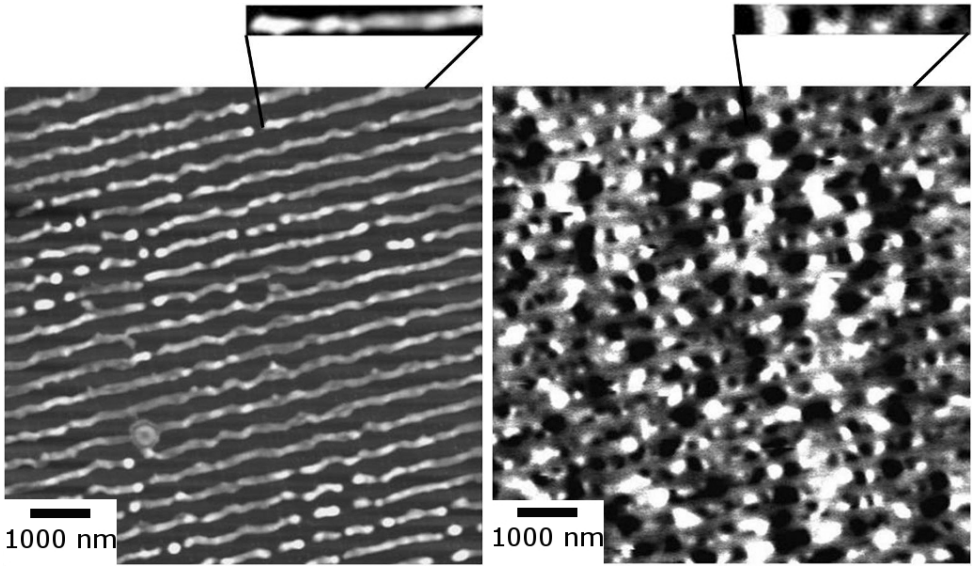

Figure 7.1: AFM (a) and the corresponding zero-field MFM (b) of ordered Co nanowire, the magnified part of the Co nanowire is indicated in both (a) and (b).

7.2.2.2 Co nanopolygon

Figure 7.2 shows the AFM [Fig. 7.2(a)] and the corresponding MFM [Fig. 7.2(b)] images of a polygon made from single beam irradiation of Co film on SiO_2 substrate. The average width and height of the polygonal arms were measured to be 95 nm and 30 nm, respectively, and the calculated contact angle was 68^o. The TEM image of the polygons are shown in Fig. 7.3. The highly inhomogeneous cross sections of the polygonal arms is clearly visible, which is not surprising, considering that the polygons form at fairly early stages of the dewetting process. The MFM image indicates the formation of magnetic flux-closure, where the domains terminate at the nodes of the polygon and change direction along the arms of the polygon, forming a closed loop. Similar to the nanowires, the kinks and bends at the nodal points appear to have helped the formation of domain walls at these points.

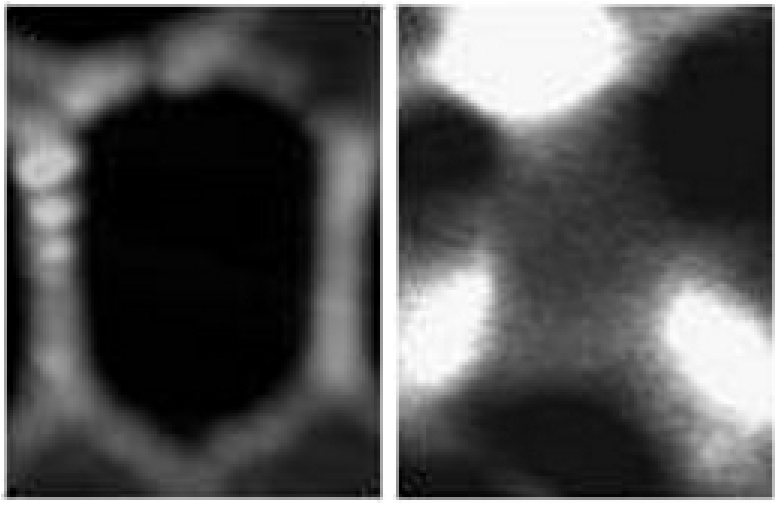

(a) (b)

Figure 7.2: AFM (a) and MFM (b) of a polygon of Co on SiO_2 (both image size is $600\,nm \times 850\,nm$).

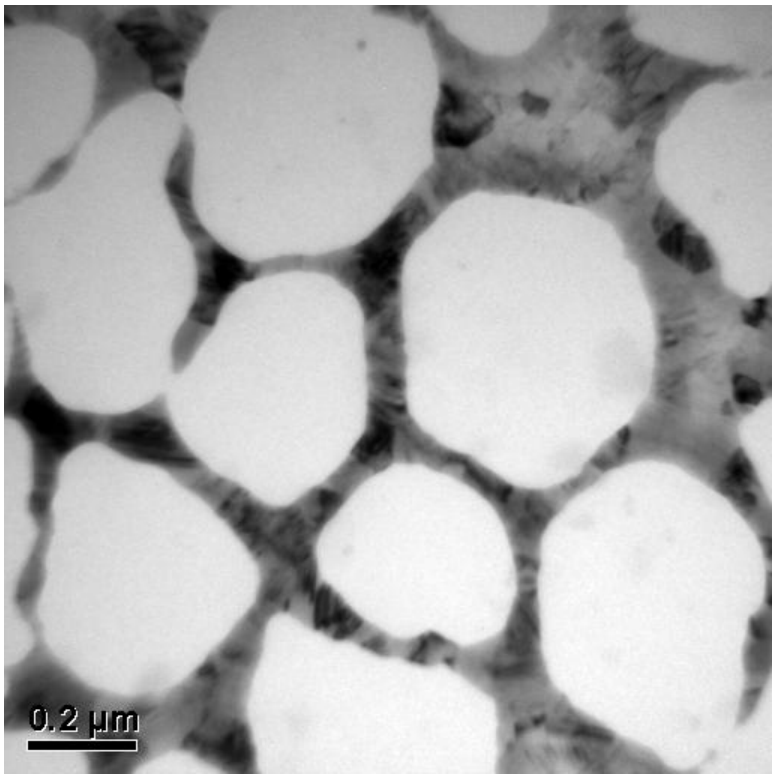

Figure 7.3: TEM micrograph of Co polygon networks, indicating polycrystalline behavior of the microstructure.

7.2.2.3 Ag-Co nanowire

The nanowires made after laser irradiation of a $Co_{40}Ag_{60}$ film, are expected to be made of phase separated small grains of Ag and Co, similar to the nanoparticles shown earlier in chapter 3. The average width and height of the nanowires were measured to be 400 nm and 150 nm, and the calculated contact angle was 75^o. The nanowires are $\sim 3\ \mu m$ long with in-plane magnetization, consisting of much larger domains (1000 - 2000 nm), compared to pure Co (250 - 400 nm). In spite of the presence of a significant fraction of non-magnetic Ag grains, the magnetic nature of these nanowires indicate that the Co grains are easily exchanged coupled. The Co exchange length is $\sim$3.5 nm [191, 190]. The important difference in the magnetic properties of nanowires of $Co_{40}Ag_{60}$ composite compared to pure Co are: (a) much larger domain size, and (b) along the axis of the nanowire magnetization, compared to the random in-plane orientations for pure Co. The former is most likely a result of smaller magnetocrystalline anisotropy, while the reason for the latter is less clear. It is conceivable that because of the finer grains, the small scale irregularities in the morphology average out over the much larger length scale of the domains. This enables the magnetization to follow the direction of the shape anisotropy (along the wire axis), without being hindered by small scale defects and imperfections in the wire morphology.

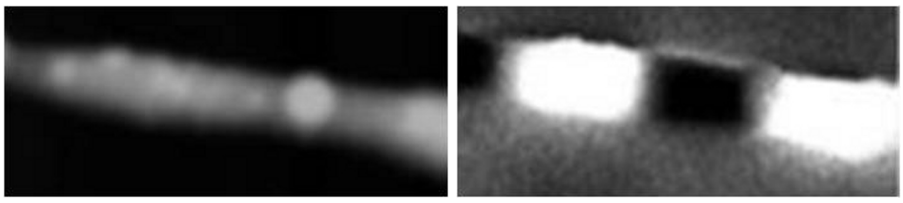

(a) (b)

Figure 7.4: $Co_{40}Ag_{60}$ nanocomposite nanowire; (a) AFM, (b) MFM (both image size is $3\mu m$ X $1\mu m$)

7.3 Acknowledgments

I would like to acknowledge Dr. C. Favazza for the TEM image of Co polygon networks, shown in Fig. 7.3.

Bibliography

[1] H. Krishna, N. Shirato, C. Favazza, and R. Kalyanaraman, "Energy driven self-organization in nanoscale metallic liquid films," *Phys. Chem. Chem. Phys.*, vol. 11, pp. 8136–8143, 2009.

[2] F. Ross, J. Tersoff, and R. Tromp, "Coarsening of Self-assembled Ge Quantum Dots on Si(001)," *Phys. Rev. Lett.*, vol. 80, pp. 984–87, 1998.

[3] S. Camazine, "Patterns in nature," *Natural history*, vol. June, pp. 34–41, 2003.

[4] J. Trice, C. Favazza, D. Thomas, H. Garcia, R. Kalyanaraman, and R. Sureshkumar, "Novel self-organization mechanism in ultrathin liquid films: theory and experiment," *Phys. Rev. lett.*, vol. 101, no. 1, p. 017802, 2008.

[5] C. L. Dennis, R. P. Borges, L. D. Buda, U. Ebels, J. F. Gregg, M. Hehn, E. Jouguelet, K. Ounadjela, I. Petej, I. L. Prejbeanu, and M. J. Thornton *J. Phys: Condens. Matter.*, vol. 14, p. R1175, 2002.

[6] H. Krishna, C. Miller, L. Longstreth-Spoor, Z. Nussinov, A. K. Gangopadhyay, and R. Kalyanaraman *J. Appl. Phys.*, vol. 103, no. 7, p. 073902, 2008.

[7] M. A. Meyers, A. Mishra, and D. J. Benson, "Mechanical properties of nanocrystalline materials," *Prog. Mat. Sci.*, vol. 51, pp. 427–556, 2006.

[8] K. L. Kelly, E. Coronado, L. L. Zhao, and G. C. Schatz, "The optical properties of

metal nanoparticles: The influence of size, shape, and dielectric environment," *J. Phys. Chem.*, vol. 107, pp. 668–677, 2003.

[9] Y. Xia and J. N. Halas, "Synthesis and surface plasmonic properties of metallic nanostructures," *MRS Bull.*, vol. 30, p. 338, 2005.

[10] S. Maier, P. G. Kik, and H. A. Atwater, "Observation of couple plasmon-polariton modes in Au nanoparticle chain waveguide of different length: Estimation of waveguide losses," *Appl. Phys. Lett*, vol. 81, pp. 1714–16, 2002.

[11] D. L. Leslie-Pelecky and R. D. Rieke, "Magnetic properties of nanostructured materials," *Chem. Mater.*, vol. 8, pp. 1770–1783, 1996.

[12] C. Kittel *Rev. Mod. Phys.*, vol. 21, p. 541, 1949.

[13] C. Kittel *Phys. Rev.*, vol. 70, p. 965, 1946.

[14] J. B. Gonzalez-Diaz, A. Garcia-Martin, J. M. Garcia-Martin, A. Cebollada, G. Armelles, B. Sepulveda, Y. Alaverdyan, and M. Kall, "Plasmonic Au/Co/Au Nanosandwiches with Enhanced Magneto-optical Activity," *Small*, vol. 4, pp. 202–205, 2008.

[15] K. Drexler, "Molecular engineering: An approach of the development of general capabilities for molecular manipulation," in *National Academy of Sciences*, vol. 78, pp. 5275–5278, 1981.

[16] K. Drexler and J. S. Foster, "Synthetic tips," *Nature*, vol. 343, pp. 600–604, 1990.

[17] H. Gleiter, "Nanostructured materials: basic concepts and microstructure," *Acta. Mater.*, vol. 48, pp. 1–29, 2000.

[18] K. Inomata and Y. Saito, "Spin-dependent tunneling through layered ferromagnetic nanoparticles," *Appl. Phys. Lett.*, vol. 73, pp. 1143–1145, 1998.

[19] J. Stahl, M. Debe, and P. Coleman, "Enhanced bioadsorption characteristics of a uniquely nanostructured thin film," *J. Vac. Sci. Tech. A*, vol. 14, pp. 1761–1764, 1996.

[20] D. Shtanski, S. Kulinich, E. Levashov, and J. Moore, "Structure and physical-mechanical properties of nanostructured thin films," *Phys. Sol. St.*, vol. 45, pp. 1177–1184, 2003.

[21] M. Todorovic, S. Schuttz, J. Wong, and A. Scherer *Appl. Phys. Lett.*, vol. 74, p. 2516, 1999.

[22] X. Huang, L. Tan, H. Cho, and B. J. H. Stadler, "Magnetoresistance and spin transfer torque in electrodeposited co/cu multilayered nanowire arrays with small diameters," *J. Appl. Phys.*, vol. 105, p. 07D128, 2009.

[23] G. Jo, M. J. Hong, W-K., M. Choe, W. Park, and T. Lee, "Logic inverters composed of controlled depletion-mode and enhancement-mode zno nanowire transistors," *Appl. Phys. Lett.*, vol. 94, p. 173118, 2009.

[24] S. K. Gupta, A. Joshi, and M. Kaur, "Development of gas sensors using zno nanostructures," *J. Chem. Sci.*, vol. 122, pp. 57–62, 2010.

[25] M. Quinten, A. Leitner, J. Krenn, and F. Aussenegg, "Electromagnetic energy transport via linear chains of silver nanoparticles," *Opt. Lett.*, vol. 23, p. 1331, 1998.

[26] S. A. Maier, P. G. Kik, and H. A. Atwater, "Optical pulse propagation in metal nanoparticle chain waveguides," *Phys. Rev. B*, vol. 67, p. 205402, 2003.

[27] S. Fan, M. Chapline, N. Franklin, T. Tombler, A. Cassell, and H. Dai, "Self-Oriented Regular Arrays of Carbon Nanotubes and Their Field Emission Properties," *Science*, vol. 283, pp. 512–514, 1999.

[28] S. Tsunashima, "Magneto-optical recording," *J. Phys. D: App. Phys.*, vol. 34, pp. R87–R102, 2001.

[29] J. Lodder, M. Haast, and L. Abelman in *NATO Advanced Study Institute on Magnetic Systems Beyond 2000* (G. C. Hadjippannayis, ed.), (Dordrecht), p. 117, Kluwer Academic, 2002.

[30] H. N. Bertram and M. Williams *IEEE Trans. Magn.*, vol. 36, p. 4, 2000.

[31] M. Albrecht, S. Ganesan, C. T. Rettner, A. Moser, M. E. Best, R. L. White, and B. D. Terris *IEEE Trans. Magn.*, vol. 39, p. 2323, 2003.

[32] S. Y. Chou, P. R. Krauss, and L. Kong *J. Appl. Phys.*, vol. 79, p. 6101, 1996.

[33] A. Sharma and R. Khanna, "Pattern Formation in Thin Liquid Films," *Phys. Rev. Lett.*, 19 Oct. 1998.

[34] C. Favazza, R. Kalyanaraman, and R. Sureshkumar, "Dynamics of ultrathin metal films on amorphous substrates under fast thermal processing," *J. Appl. Phys*, vol. 102, p. 104308, 2007.

[35] C. Favazza, R. Kalyanaraman, and R. Sureshkumar *Nanotechnology*, vol. 17, p. 4229, 2006.

[36] S. Kondo and R. Asal, "A reaction-diffusion wave on the skin of the marine angelfish Pomacanthus," *Nature*, vol. 376, pp. 765–768, 1993.

[37] J. Trice, D. Thomas, C. Favazza, R. Sureshkumar, and R. Kalyanaraman, "Investigation of laser-induced dewetting in nanoscopic Co films: Experiments and modeling of thermal behavior." 2006.

[38] A. Ashton, A. Brad Murray, and O. Arnault, "Formation of coastline features by large-scale instabilities induced by high-angle waves," *Nature*, vol. 414, pp. 296–300, 2001.

[39] A. Sharma and E. Ruckenstein *J. Colloid. Interface Sci.*, vol. 106, p. 12, 1985.

[40] A. Sharma, "Relationship of thin film stability and morphology to macroscopic parameters of wetting in the apolar and polar systems," *Langmuir*, vol. 9, no. 3, pp. 861–869, 1993.

[41] A. Sharma and A. Jameel, "Nonlinear stability, rupture and morphological phase separation in thin fluids on apolar and polar substrates," vol. 161, pp. 190–208, 1993.

[42] R. Seemann, S. Herminghaus, and K. Jacobs, "Dewetting patterns and molecular forces," *Phys. Rev. Lett.*, vol. 86, pp. 5534–37, 2001.

[43] C. Zhang and R. Kalyanaraman, "In-situ nanostructured film formation during physical vapor deposition," *App. Phys. Lett.*, vol. 83, no. 23, pp. 4827–29, 2003.

[44] M. Vasudevan, A. Shen, B. Khomani, and R. Sureshkumar, "Self-similar shear-thickening behavior in ctab/nasal surfactant solutions," *J. Rheol.*, vol. 52, pp. 527–550, 2008.

[45] J. Bischof, D. Scherer, S. Herminghaus, and P. Leiderer, "Dewetting Modes of Thin Metallic Films: Nucleation of Holes and Spinodal Dewetting," *Phys. Rev. Lett.*, 19 Aug. 1996.

[46] S. Herminghaus, K. Jacobs, K. Mecke, J. Bischof, A. Fery, M. Ibn-Elhaj, and S. Schlagowski, "Spinodal dewetting in liquid crystal and liquid metal films," *Science*, vol. 282, pp. 916–919, 1998.

[47] C. Favazza, J. Trice, H. Krishna, R. Kalyanaraman, and R. Sureshkumar *Appl. Phys. Lett.*, vol. 88, p. 1531181, 2006.

[48] C. Favazza, J. Trice, H. Krishna, R. Kalyanaraman, and R. Sureshkumar, "Laser-induced short- and long-range ordering of Co nanoparticles on SiO2," *Appl. Phys. Lett.*, vol. 88, pp. 1531181–83, 2006.

[49] A. Sharma and E. Ruckenstein, "Finite-Amplitude Instability of Thin Free and Wetting Films: Prediction of Lifetimes," *Langmuir*, vol. 2, pp. 480–494, 1986.

[50] C. Favazza, J. Trice, A. Gangopadhyay, H. Garcia, R. Sureshkumar, and R. Kalyanaraman, "Nanoparticle ordering by dewetting of Co on SiO2," *J. Elec. Mat.*, vol. 35, pp. 1618–20, 2006.

[51] F. Brochard-Wyart, P. G. Gennes, and D. Quere, *Capillarity and Wetting Phenomenon*. New York: Springer, 2003.

[52] J. W. Cahn, "Phase separation by spinodal decomposition in isotropic systems," *J. Chem. Phys.*, vol. 62, pp. 93–99, 1965.

[53] G. Reiter, "Dewetting of thin polymer films," *Phys. Rev. Lett.*, vol. 68, no. 1, pp. 75–78, 1992.

[54] J.-U. Thiele, L. Folks, M. F. Toney, and D. K. Weller, "Perpendicular magnetic anisotropy and magnetic domain structure in sputtered epitaxial fept (001) l1[sub 0] films," *Journal of Applied Physics*, vol. 84, no. 10, pp. 5686–5692, 1998.

[55] T. Stange and D. Evans, "Nucleation and growth of defects leading to dewetting of thin polymer films," *Langmuir*, vol. 13, pp. 4459–4465, 1997.

[56] U. Thiele, M. G. Velarde, and K. Neuffer, "Dewetting: film rupture by nucleation in the spinodal regime," *Phys. Rev. Lett.*, vol. 87, no. 1, p. 016104, 2001.

[57] B. J. Spencer, P. W. Voorhees, and S. H. Davis, "Morphological Instabilities in Epitaxially Strain Dislocation-Free Solild Films," *Phys. Rev. Lett.*, vol. 67, pp. 3696–3699, 23 Dec. 1991.

[58] W. Lu and Z. Suo, "Dynamics of nanoscale pattern formation of an epitaxial monolayer," *J. Mech. Phys. Solids*, vol. 49, pp. 1937–1950, 2001.

[59] F. K. LeGoues, V. P. Kesan, S. S. Iyer, J. Tersoff, and R. Tromp, "Surface-Stress-Induced Order in SiGe Alloy Films," *Phys. Rev. Lett.*, vol. 64, pp. 2038–2042, 23 Apr. 1990.

[60] J. Israelachvili, *Intermolecular and surface forces*, ch. van der Waals forces between surfaces. London, UK: Academic Press, 1992.

[61] V. A. Parsegian, *Van der Waals Forces: A Handbook for Biologists, Chemists, Engineers, and Physicists*. New York, NY: Cambridge University Press, 2006.

[62] A. Vrij, "Possible mechanism for the spontaneous rupture of thin, free liquid films," *Discuss. Faraday Soc.*, vol. 42, pp. 23–27, 1966.

[63] A. Vrij and J. T. G. Overbeek, "Rupture of Thin Liquid Films Due to Spontaneous Fluctuations in Thickness," *J. Am. Chem. Soc.*, vol. 90, pp. 3074–78, 1968.

[64] J. Becker, G. Grun, R. Seeman, H. Mantz, K. Jacobs, K. Mecke, and R. Blossey, "Complex dewetting scenarios captured by thin-film models," *Nature Materials*, vol. 2, p. 59, 2003.

[65] J. Trice, R. Kalyanaraman, and R. Sureshkumar, "Computational modeling of laser-induced self-organization in nanoscopic metal films for predictive nanomanufacturing," in *Instrumentation, Metrology, and Standards for Nanomanufacturing* (M. T. Postek and J. A. Allgair, eds.), vol. 6648 of *Proceedings of SPIE*, p. 66480K, SPIE, SPIE, 2007.

[66] P. de Gennes, F. Brochard-Wyart, and D. Quere, *Capillarity and Wetting Phenomena: Drops, Bubbles, Pearls, Waves*. Springer, 2004.

[67] P.-G. de Gennes, F. Brochard-Wyart, and D. Quere, *Capillarity and wetting phenomenon*. New york: Springer, 2003.

[68] E. Guyon, J.-P. Hulin, L. Petit, and C. D. Mitescu, *Physical Hydrodynamics*, ch. Hydrodynamic instabilities, pp. 439–489. Oxford university press, 2001.

[69] A. Pototsky, M. Bestehorn, D. Merkt, and U. Theile *Phys. Rev. E*, vol. 70, p. 025201, 2004.

[70] A. Pototsky, M. Bestehorn, D. Merkt, and U. Thiele *Euro. Phys. Lett.*, vol. 74, p. 665, 2006.

[71] A. Sharma and R. Khanna, "Pattern Formation in Unstable Thin Liquid Films," *Phys. Rev. Lett.*, vol. 81, no. 16, pp. 3463–3466, 1998.

[72] D. Bandyopadhyay, R. Gulabani, and A. Sharma *Ind. Eng. Chem. Res.*, vol. 44, p. 1259, 2005.

[73] D. Sander, "The magnetic anisotropy and spin reorientation of nanostructures and nanoscale films," *J. Phys.: Condens. Matter*, vol. 16, pp. R603–R636, 2004.

[74] R. Skomski and J. M. D. Coey, *Parmanent magnetism*. Bristol: Institute of Physics Publishing, 1999.

[75] R. M. Bozorth, *Ferromagnetism*. NJ: IEEE, 1993.

[76] C. Kittel, *Introduction to solid state physics, 7th ed.* New York: John Wiley and Sons, Ltd., 2003.

[77] B. D. Cullity, *Introduction To Magnetic Materials*. Addison-Wesley Publishing Company, 1972.

[78] R. Skomski, "Nanomagnetics," *J. Phys.: Condens. Matter*, vol. 15, pp. R841–R896, 2003.

[79] P. B. Johnson, Christy, and R. W., "Optical Constants of Noble Metals," *Phys. Rev. B*, vol. 6, p. 4370, 1972.

[80] J. Shen and J. Kirschner *Surf. Sci.*, vol. 500, pp. 300–322, 2002.

[81] R. Moroni, D. Sekiba, F. Buatier de Mongeot, G. Gonella, C. Boragno, L. Mattera, and U. Valbusa *Phys. Rev. Lett.*, vol. 91, p. 167207, Oct 2003.

[82] J. A. C. Bland and B. Heinrich, *Ultrathin magnetic structures*. Springer, 2005.

[83] J. A. C. Bland and B. Heinrich, *Ultrathin magnetic structures*. Springer, 1994.

[84] D. J. Sellmyer, M. Zheng, and R. Skomski, "Magnetism of fe, co and ni nanowires in self-assembled arrays," *J. Phys.: Cond. Matt.*, vol. 13, pp. R433–R460, 2001.

[85] H. Krishna, C. Miller, L. Longstreth-Spoor, Z. Nussinov, A. K. Gangopadhyay, and R. Kalyanaraman, "Unusual size-dependent magnetization in near hemispherical co nanomagnets on sio[sub 2] from fast pulsed laser processing," *J. Appl. Phys.*, vol. 103, no. 7, p. 073902, 2008.

[86] O. Fruchart and A. Thiaville, "Magnetism in reduced dimensions," Nov. 2005.

[87] M. Beleggia, S. Tandon, Y. Zhu, and M. D. Graef *J. Magn. Magn. Mat.*, vol. 278, p. 270, 2004.

[88] R. M. H. New, R. F. W. Pease, and R. L. White *IEEE Trans. Magn.*, vol. 31, p. 3805, 1995.

[89] J. D. Jackson, *Classical Electrodynamics*. John Wiley & Sons, Inc., 1999.

[90] X. Chen, S. Mandre, and J. J. Feng, "Partial coalescence between a drop and a liquid-liquid interface," *Phys. Fl.*, vol. 18, no. 5, p. 051705, 2006.

[91] F. G. West *J. Appl. Phys.*, vol. 35, p. 1827, 1964.

[92] R. Baron and R. W. Hoffman *J. Appl. Phys.*, vol. 41, p. 1623, 1970.

[93] C. Kittel, *Introduction to Solid State Physics*. John Wiley and Sons, Inc., 1971.

[94] K. Nakamura, T. Ito, and A. J. Freeman *Phys. Rev. B*, vol. 68, pp. 180404–180408, 2003.

[95] C. L. Chien and J. G. Zhu *Phys. Today*, vol. 60, pp. 40–45, 2007.

[96] M. Klaui, C. A. F. Vaz, L. L. Diaz, and J. A. C. Bland *J. Phys.: Condens. Matter.*, vol. 15, p. R985, 2003.

[97] Y. G. Yoo, M. Klaui, C. A. F. Vaz, L. J. Heyderman, and J. A. C. Bland *Appl. Phys. Lett.*, vol. 82, pp. 2470–2472, 2003.

[98] M. Vazquez, *Advanced Magnetic Nanowires*. Wiley, Chichester, 2007.

[99] H. Krishna, N. Shirato, A. K. Gangopadhyay, and R. Kalyanaraman, "Fe nanomagnets with unusual size-dependent magnetization directions produced by fast laser-induced self-organization," *Proc. SPIE*, vol. 7039, p. 703909, 2008.

[100] H. R. Stuart and D. G. Hall, "Island size effects in nanoparticle-enhanced photodetectors," *App. Phys. Lett.*, vol. 73, no. 26, pp. 3815–3817, 1998.

[101] S. Pillai, K. R. Catchpole, T. Trupke, and M. A. Green, "Surface plasmon enhanced silicon solar cells," *Journal of Applied Physics*, vol. 101, no. 9, 2007. Pillai, S. Catchpole, K. R. Trupke, T. Green, M. A.

[102] K. A. Willets and R. P. Van Duyne, "Localized surface plasmon resonance spectroscopy and sensing," *Ann. Rev. Phys. Chem.*, vol. 58, pp. 267–297, 2007.

[103] J. M. McLellan, Z. Y. Li, A. R. Siekkinen, and Y. Xia, "The SERS activity of a supported Ag nanocube strongly depends on its orientation relative to laser polarization," *Nano Lett.*, vol. 7, pp. 1013 –1017, 2007.

[104] A. Gangopadhyay, H. Krishna, C. Favazza, C. Miller, and R. Kalyanaraman, "Heterogeneous nucleation of amorphous alloys on catalytic nanoparticles to produce 2D patterned nanocrystal arrays," *Nanotechnology*, vol. 18, p. 485606, 2007.

[105] J.-M. Nam, C. S. Thaxton, and C. A. Mirkin, "Nanoparticle-Based Bio-Bar Codes for the Ultrasensitive Detection of Proteins," *Science*, vol. 301, p. 1884, 2003.

[106] M.-C. Daniel and D. Astruc, "Gold Nanotparticles: Assembly, Supramolecular Chemistry, Quantum-Size-Related Properties, and Applications toward Biology, Catalysis, and Nanotechnology," *Chem. Rev.*, vol. 104, pp. 293–346, 2004.

[107] W. K. Park, R. J. Ortega-Hertogs, J. S. Moodera, A. Punnoose, and M. Seehra, "Semiconducting and ferromagnetic behavior of sputtered Co-doped TiO2 thin films above room temperature," *J. Appl. Phys.*, vol. 91, no. 10, p. 8093, 2002.

[108] G. Nicolas and I. Prigogine, *Self-Organization in Non-Equilibrium Systems*. New York: Wiley, 1977.

[109] C. Redon, F. Brochard-Wyart, and F. Rondelez, "Dynamics of dewetting," *Physical Review Letters*, vol. 66, no. 6, pp. 715–718, 1991.

[110] S. Herminghaus, K. Jacobs, K. Mecke, J. Bischof, A. Fery, M. Ibn-Elhaj, and S. Schlagowski, "Spinodal dewetting in liquid crystal and liquid metal films," *Science*, vol. 282, pp. 916–919, 1998.

[111] J. Bischof, M. Reimmuth, J. Boneberg, H. Herminghaus, T. Palberg, and P. Leiderer in *SPIE*, vol. 2777, p. 119, 1996.

[112] S. J. Henley, J. D. Carey, and S. R. P. Silva, "Pulsed-laser-induced nanoscale island formation in thin metal-on-oxide films," *Phys. Rev. B*, vol. 72, pp. 195408–I–195408–10, 2005.

[113] C. Favazza, J. Trice, R. Kalyanaraman, and R. Sureshkumar *Appl. Phys. Lett.*, vol. 91, p. 043105, 2007.

[114] P.-G. de Gennes, "The dynamics of a spreading droplet," *C. R. Acad. Paris*, vol. 298, pp. 111–115, 1984.

[115] O. S. Heavens, *Optical properties of thin solid*, pp. 76–77. London: Butterworth Publications, LTD., 1955.

[116] L. Kondic, "Instabiliites in gravity driven flow of thin fluid films," *SIAM Review*, vol. 45, pp. 95–115, 2003.

[117] C. L. Yaws, ed., *Chemical Properties Handbook*. McGraw-Hill, 1999.

[118] H. M. Lu and Q. Jiang, "Surface tension and its temperature coefficient for liquid metals," *J. Phys. Chem. B*, vol. 109, no. 32, pp. 15463–15468, 2005.

[119] T. B. Massalski, *Binary Alloy Phase Diagrams*, vol. 1. American Society for Metals, 1986.

[120] M. P. Brochard Wyart, F. and C. Redon, "Liquid/liquid dewetting," *Langmuir*, vol. 9, pp. 3682–3690, 1993.

[121] L. Kondic, "Instabilities in Gravity Driven Flow of Thin Films," *SIAM Rev.*, vol. 45, pp. 95–115, 3 Feb. 2003.

[122] J. N. Islaelachvili, *Intermolecular and Surface Forces*. London: Academic Press, 1985.

[123] J. Trice, D. Thomas, C. Favazza, R. Sureshkumar, and R. Kalyanaraman *Phys. Rev. B*, vol. 75, p. 235439, 2007.

[124] PCPDFWIN database, CAS No. 7440-48-4, PDF No. 02-1098, 03-0931, 1997.

[125] PCPDFWIN database, CAS No. 7440-48-4, PDF No. 15-0806, 1997.

[126] K. Willets and R. P. Van Duyne, "Localized Surface Plasmon Resonance Spectroscopy and sensing," *Annu. Rev. Phys. Chem.*, vol. 58, p. 267, 2007.

[127] M. Fleischmann, P. J. Hendra, and A. MacQuillan, "Raman spectra of pyridine adsorbed at a silver electrode," *Chem. Phys. Lett.*, vol. 26, pp. 163–168, 1974.

[128] A. Atena and M. Khenner, "Thermocapillary effects in driven dewetting and self assembly of pulsed-laser-irradiated metallic films," *Physical Review B (Condensed Matter and Materials Physics)*, vol. 80, no. 7, p. 075402, 2009.

[129] Y. F. Guan, R. C. Pearce, A. V. Melechko, D. K. Hensley, M. L. Simpson, and P. D. Rack, "Pulsed laser dewetting of nickel catalyst for carbon nanofiber growth," *Nanotechnology*, vol. 19, p. 235604, 2008.

[130] J. Boneberg, A. Habenicht, D. Benner, M. Leiderer, Trautvetter, C. Pfahler, A. Plettl, and P. Ziemann, "Jumping nanodroplets: a new route towards metallic nanoparticles," *Appl. Phys. A: Mater. Sci. and Proc.*, vol. 93, pp. 415–419, 2008.

[131] F. Brochard Wyart and J. Daillant, "Drying of solids wetted by thin liquid films," *Can. J. Phys.*, vol. 68, pp. 1084–88, 1990.

[132] R. Xie, A. Karim, J. Douglas, C. Han, and R. Weiss, "Spinodal dewetting of thin polymer films," *Phys. Rev. Lett.*, vol. 81, pp. 1251–1254, AUG 10 1998.

[133] R. Seemann, S. Herminghaus, and K. Jacobs, "Gaining control of pattern formation of dewetting liquid films," *J. Phys. Cond. Matt.*, vol. 13, p. 4925, 2001.

[134] C. Favazza, J. Trice, A. Gangopadhyay, H. Garcia, R. Sureshkumar, and R. Kalyanaraman, "Nanoparticle ordering by dewetting of Co on SiO2," *J. Elec. Mat*, Aug. 2006.

[135] C. Favazza, R. Kalyanaraman, and R. Sureshkumar, "Dynamics of ultrathin metal films on amorphous substrates under fast thermal processing," *J. Appl. Phys.*, vol. 102, p. 104308, 2007.

[136] A. Sharma, "Relationship of thin film stability and morphology to macroscopic parameters of wetting in the apolar and polar systems," *Langmuir*, vol. 9, no. 3, pp. 861–869, 1993.

[137] V. Mitlin, "On dewetting conditions," *Colloids Surf. A*, vol. 89, pp. 97–101, 1994.

[138] R. M. H. New, R. F. W. Pease, and R. L. White *J. Vac Sci. Technol. B*, vol. 12, p. 3196, 1994.

[139] P. R. Krauss, P. B. Fischer, and S. Y. Chou *J. Vac. Sci. Technol. B*, vol. 12, p. 3639, 1994.

[140] S. Y. Chou, P. R. Krauss, and P. J. Renstrom *J. Vac. Sci. Technol. B*, vol. 14, p. 4129, 1996.

[141] M. Salerno, J. R. Krenn, B. Lamprecht, G. Schider, H. Ditlbacher, N. Felidj, A. Leitner, and F. R. Aussenegg *Opto-Electron. Rev.*, vol. 10, p. 217, 2002.

[142] R. S. Molday and D. Mackenzie *J. Immunol. Methods*, vol. 52, p. 353, 1982.

[143] A. Jordan, R. Scholz, P. Wust, H. Schirra, T. Schiestel, H. Schmidt, and R. Felix *J. Magn. Magn. Mater.*, vol. 194, p. 185, 1999.

[144] K. Coffey, M. Parker, and J. Howard *IEEE Trans. Mag.*, vol. 31, pp. 2737 – 2739, 1995.

[145] S. Charap, P.-L. Lu, and Y. He, "Thermal stability of recorded information at high densities," *IEEE Trans. Mag.*, vol. 33, pp. 978 – 983, 1997.

[146] C. A. Ross, H. I. Smith, T. Savas, M. Schattenburg, M. Farhoud, M. Hwang, M. Walsh, M. C. Abraham, and R. J. Ram *J. Vac. Sci. Tech. B*, vol. 17, pp. 3168–3176, 1999.

[147] S. Kang, S. Shi, Z. Jia, G. B. Thompson, D. E. Nikles, J. W. Harrell, D. Li, N. Poudyal, V. Nandwana, and J. P. Liu, "Microstructures and magnetic alignment of l1[sub 0] fept nanoparticles," vol. 101, p. 09J113, AIP, 2007.

[148] X. W. Wu, M. S. Rzchowski, H. S. Wang, and Q. Li *Phys. Rev. B*, vol. 61, p. 501, 2000.

[149] O. Moran, D. Fuchs, P. Adelmann, and R. Schneider *Ann. Phys. (Leipzig)*, vol. 13, p. 74, 2004.

[150] C. Favazza, J. Trice, H. Krishna, R. Kalyanaraman, and R. Sureshkumar *Appl. Phys. Lett.*, vol. 88, p. 1531181, 2006.

[151] C. Favazza, J. Trice, A. K. Gangopadhyay, H. Garcia, R. Sureshkumar, and R. Kalyanaraman *J. Electron. Mater.*, vol. 35, p. 1618, 2006.

[152] C. Favazza, H. Krishna, R. Sureshkumar, and R. Kalyanaraman *Proceedings, SPIE*, p. 664809, 2007.

[153] C. Favazza, R. Kalyanaraman, and R. Sureshkumar *Nanotechnology*, vol. 17, p. 4229, 2006.

[154] "www.asylumresearch.com."

[155] L. Longstreth-Spoor, J. Trice, H. Garcia, C. Zhang, and R. Kalyanaraman *J. Phys. D: Appl. Phys.*, vol. 39, p. 5149, 2006.

[156] *Natl. Bur. Stand. (US) Monogr.*, vol. 24, no. 4, p. 10, 1966.

[157] Hofer and Peebles *J. Am. Chem. Soc.*, vol. 69, p. 897, 1947.

[158] Digital Instruments, Veeco Metrology Group, *Scanning Probe Microscopy Training Notebook*, 3.0 ed., 1998.

[159] D. Rugar, H. J. Mamin, P. Guethner, S. E. Lambert, J. E. Stern, I. McFadyen, and T. Yogi *J. Appl. Phys.*, vol. 68, p. 1169, 1990.

[160] U. Hartmann *Annu. Rev. Mater. Sci.*, vol. 29, p. 53, 1999.

[161] C. D. Wright and E. W. Hill *Appl. Phys. Lett.*, vol. 67, p. 433, 1995.

[162] A. Hubert, W. Rave, and S. L. Tomlinson *Phys. Stat. Sol. (b)*, vol. 204, p. 817, 1997.

[163] D. K. Cheng, *Field and Wave Electromagnetics*. Prentice Hall, 2nd ed., 1989.

[164] A. Fernandez, P. J. Bedrossian, S. L. Baker, S. P. Vernon, and D. R. Kania *IEEE Trans. Magn.*, vol. 32, p. 4472, 1996.

[165] R. M. H. New, R. F. W. Pease, and R. L. White *J. Vac. Sci. Technol. B*, vol. 13, p. 1089, 1995.

[166] W. F. Brown *J. Appl. Phys.*, vol. 39, p. 993, 1968.

[167] A. Aharoni *J. Appl. Phys.*, vol. 63, p. 5879, 1988.

[168] R. P. Boardman, J. Zimmermann, H. Fangohr, A. A. Zhukov, and P. A. J. d. Groot *J. Appl. Phys.*, vol. 97, p. 10E305, 2005.

[169] R. P. Boardman, H. Fangohr, S. J. Cox, A. V. Goncharov, A. A. Zhukov, and P. A. J. d. Groot *J. Appl. Phys.*, vol. 95, p. 7037, 2004.

[170] W. Sucksmith and J. E. Thompson in *Mathematical and Physical Sciences*, vol. 225 of *Series A*, p. 362, Royal Society of London, 1954.

[171] J. Gump, H. Xia, M. Chirita, R. Sooryakumar, M. A. Tomaz, and G. R. Harp *J. Appl. Phys.*, vol. 86, p. 6005, 1999.

[172] H. Krishna, A. K. Gangopadhyay, J. Strader, and R. Kalyanaraman, "Self-organized synthesis of patterned magnetic nanostructures with in-plane and perpendicular to the plane magnetization." Nanotechnology, Jan 2010.

[173] Z. Shan, E. A. Stach, J. M. K. Wiezorek, J. A. Knapp, D. M. Follstaedt, and S. X. Mao *Science*, vol. 305, p. 654, 2004.

[174] A. M. V. Diepen and F. J. A. Broeder *J. Appl. Phys.*, vol. 48, p. 3165, 1977.

[175] M. Huth and C. P. Flynn *J. Mag. Mag. Mat.*, vol. 204, p. 204, 1999.

[176] A. Mougin, C. Dufour, K. Dumesnit, and P. Mangin *Phys. Rev. B*, vol. 62, p. 9517, 2000.

[177] H. M. Hwang, S. W. Shin, J. H. Kang, J. Lee, J. H. Lee, J. H. Song, J. Y. Choi, H. H. Lee, and H. S. Lee *J. Korean Phys. Soc.*, vol. 49, pp. 1016–1019, 2006.

[178] B. E. Lorenz and C. D. Graham *IEEE Trans. Magn.*, vol. 40, p. 2751, 2004.

[179] R. C. Hall *J. Appl. Phys.*, vol. 30, p. 816, 1959.

[180] A. A. Karimpoor, U. Erb, K. T. Aust, and G. Palumbo *Scripta Mat.*, vol. 49, pp. 651–656, 2003.

[181] Z. Zong, J. Lou, O. O. Adewoye, A. A. Elmustafa, F. Hammad, and W. O. Soboyejo *Mat. Sci. and Eng. A*, vol. 434, pp. 178–187, 2006.

[182] D. Tabor, *The Hardness of Metals*. Clarendon Press, Oxford, 1951.

[183] Liu Y.L., Yang H.F., and Yang Y., "Gas sensing properties of tin dioxide coated onto multi-walled carbon nanotubes," *Thin Sol. Film.*, vol. 497, pp. 355–360, 2006.

[184] G. A. Alers, J. R. Neighbours, and H. Sato *J. Phys. Chem. Solids*, vol. 13, p. 40, 1960.

[185] G. F. Dieter, *Mechanical metallurgy (3rd ed.)*. McGraw Hill, New York, 1986.

[186] Q. Ma and D. Clarke, "Size dependent hardness in silver single crystals," *J. Mater. Res.*, vol. 10, p. 853, 1995.

[187] B. K. Lee *J. Mat. Sci.*, vol. 38, p. 1135, 2003.

[188] J. Q. Xiao, J. S. Jiang, and C. L. Chien, "Giant magnetoresistance in nonmultilayer magnetic systems," *Phys. Rev. Lett.*, vol. 68, pp. 3749–3752, 1992.

[189] C. C. Wang, A. O. Adeyeye, and Y. H. Wu, "Magnetic properties of asymmetric antirectangular ni80fe20 arrays," *J. Appl. Phys.*, vol. 94, pp. 6644–6648, 2003.

[190] R. Skomski, H. Zeng, and D. J. Sellmyer, "Incoherent magnetization reversal in nanowires," *J. Mag. Mag. Mat.*, vol. 249, pp. 175–180, 2002.

[191] J. Lu and X. R. Wang, "Magnetization reversal of single domain permalloy nanowires," *J. Mag. Mag. Mat.*, vol. 321, pp. 2916–2919, 2009.